THE CATHOLIC UNIVERSITY OF AMERICA

Growth and Characterization of Ferromagnetic
Nanostructures for Device Applications

A DISSERTATION

Submitted to the Faculty of the

Department of Physics

School of Arts and Sciences

Of The Catholic University of America

In Partial Fulfillment of the Requirements

For the Degree

Doctor of Philosophy

©

By

Battogtokh Jugdersuren

Washington, D. C.

2009

Growth and Characterization of Ferromagnetic
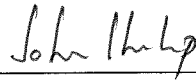Nanostructures for Device Applications
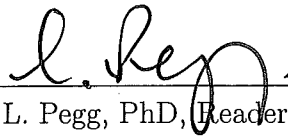
Battogtokh Jugdersuren, PhD

Director: Dr. John Philip

Nanotechnology offers tremendous potential for future technology. A better understanding of ferromagnetism, half-metallicity and magnetostriction on the smallest scales are expected to improve technological performance. Processing and characterization of nanostructured materials, therefore, are central in modern solid state physics. One of the techniques to grow nanostructures is electrospinning which offers simplicity, low cost and flexibility. This dissertation focuses on functionally different colossal magnetoresistance strontium and calcium doped lanthanum manganites and magnetostrictive iron-gallium nanowires. We have tailored the conventional electrospinning method to grow high quality manganites and iron-gallium nanowires below 100 nm in diameter for the first time. We have shown that these ferromagnetic nanostructures can be grown parallel to one another for understanding the basic physics as well as for fabricating advanced device structures. Single nanowire devices were fabricated by electron-beam lithography. Details of the growth, morphology, structure and magnetic characterization, device fabrication and performance of the devices will be discussed in this thesis. Manganite nanowires have been grown by anodized alumina oxide template and by the pulsed laser deposition methods by other groups, nanowires grown from these techniques are difficult

to use for device fabrication. Devices based on electrospun manganite and iron-gallium nanowires have shown improved electrical and magneto-transport properties. Half-metallic lanthanum-strontium manganite nanowires with 80-300 nm in diameters display enhanced magnetoresistance behavior at room temperature and the large magnetoresistance is exhibited at low magnetic field which will play an important role for creation of novel-next generation devices. Although inter-metallic, bulk iron-gallium is one of the highly attractive magnetostrictive materials, at nano level, it is very rarely studied due to difficulty of growing high-quality materials. Alumina templates or by melt-spinning are only methods applied so far to grow iron-gallium wires. Melt-spinning yields microscale ribbons and the growth using templates results in nanowires with varying stoichiometry over the entire length of the nanowire. This work has produced high quality, stoichiometric, parallel bundles of iron-gallium nanowires with diameters varying from 80-500 nm. These iron gallium nanowires exhibit enhanced magnetic properties. Devices with bundles of iron-gallium nanowires are explored for various applications such as submarine sonar, as highly sensitive magnetic sensors and nanoscale valves.
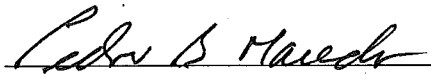
This dissertation by Battogtokh Jugdersuren fulfills the dissertation requirement for the doctoral degree in physics approved by John Philip, PhD, as Director, Ian L. Pegg, PhD, Pedro Macedo, PhD, and Andrew. Buechele, PhD, as Readers.
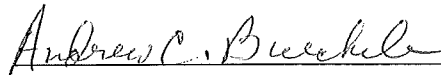
John Philip

John Philip, PhD, Director

l. Peg.

Ian. L. Pegg, PhD, Reader

Pedro B Macedo

Pedro B. Macedo, PhD, Reader

Andrew C. Buechele

Andrew. Buechele, PhD, Reader

To my dad, mom and family for their love and support

Contents

List of Figures

Acknowledgments

First of all, I would like to sincerely thank my advisor, Dr. John Philip for giving me the opportunity to join his group. As a good mentor, Dr. John Philip has not only inspired and helped me realize the exciting nature of spintronics and nanoengineering, but encouraged me get through difficult times.

Many thanks to Prof. Ian L. Pegg and Prof. Pedro B. Macedo and they have been very kind contributing their time and advices.

I am indebted to Dr. Andrew. Buechele, Dr. David A. McKeown, and Dr. Sungmu Kang for the training for SEM, XRD, Raman and Electron Beam Lithography systems. I have learnt a lot from them.

I also would like to thank Prof. Donald Heiman, North Eastern University, Boston, MA and Prof. Michael Wagner, George Washington University, DC. for their collaboration for the SQUID measurements.

I would like to thank my parents N. Jugdersuren and Ts. Adeya and my brother and sisters for providing an exceptionally strong foundation of love and support for me. I am forever grateful to them.

I would especially like to thank my wife, A. Itgel, my son, Bileg and daughter, Bujee for sharing every tearful and happy moment with me.

The financial support from the Vitreous State Laboratory is gratefully acknowledged.

Chapter 1

Introduction

1.1 Nanotechnology

During recent years, increasing interest has been developed in the class of materials known as one-dimensional (1D) nanowires, nanotubes, nanobelts and zero-dimensional (0D) nanodots. The nanowires, for example, - about 800 times smaller in diameter than human hair (Fig. 1.1) have very large surface area-to-volume ratio and exhibit strongly size-dependent, unsusal optical, thermal, magnetic and electrical properties. These novel materials are potentially offering performance advantages in micro and magneto-electronics, optical devices and in magnetic diagnostic, detection, control of cancer, molecular imaging and many other applications. In general, artificial nanostructuring is a fundamental building block of creating completely new technology at atomic, molecular or macromolecular levels referred as *Nanotechnology* [1, 2]. It deals understanding of phenomena and manipulation under control of nano-scale structures, in the length or size scale of approximately 1-100 nm range, and their integration into large logic architectures. There are extremely broad applications and many opportunities that might be realized by making new types of nano-structures, or

by downsizing existing structures. The idea of the nanotechnology philosophy is often
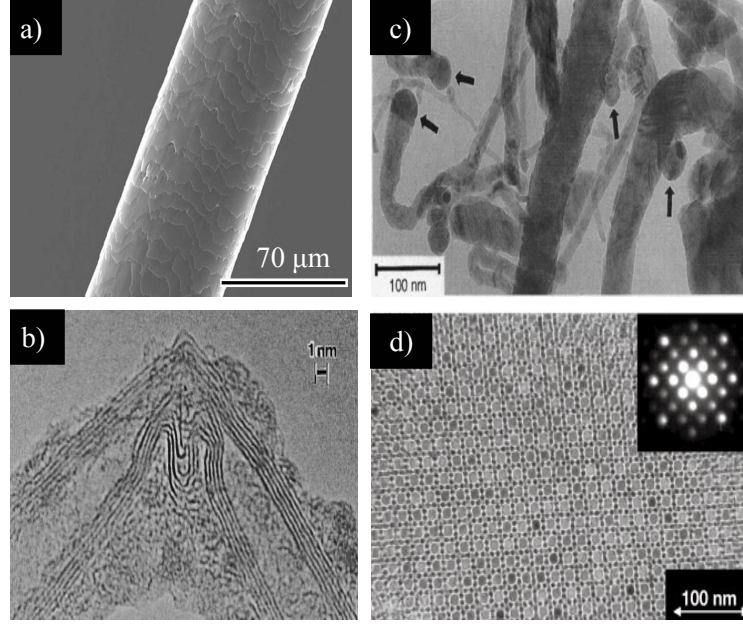
Figure 1.1 a) A human hair, b) TEM images of kink structures formed in nanotubes under mechanical duress [Ref. 5], c) TEM image of polyclystalline InP nanowires [Ref. 7], d) TEM image of PbSe nanodots [Ref. 9]

credit to the Nobel Prize winner, Dr. Richard Feynman, for his speech titled *There's Plenty of Room at the Bottom* at American Physical Society Meeting in 1959 [2]. In his lecture, Dr. R. Feynman lucidly considers rearranging the atoms, self assembly, nano scale motors and miniaturizing computers. Today the philosophy of the nanostructure is realized in many areas, particularly in microelectronics where smaller devices have meant better-less expensive, and more components per chip, faster logic operations, higher technical performance, and lower power consumption. It is interesting that based on technological improvements, in 1965, Gordon Moore made a prediction that number of transistors that can be inexpensively placed on an integrated circuit is increasing exponentially, doubling approximately every two years [3]. A standard electronic devices in late 1950's was a single device with dimension of 8

mm-1cm. Beginning of early 1980's, age of microelectronics began and smallest size of the electronic devices were reduced to (1-5) μm [4]. The first 1D nano-materials, carbon nanotubes, was independently discovered by S. Ijima and D. S. Bethune and co-workers [5,6] in 1993 and first nanowires were grown by T. J. Trentler [7] and *et al*; C. M. Lieber [8] and *et al*., respectively in 1995. The quantum dots, noble metallic clasters or semiconducting, magnetic nanocrystalline materials were grown and intensively investigated by J. S. Foresi and *et al*., 1994; A. P. Alivisato, 1996; T. Trindade, N. Pickett, and P. O'Brien, 2001 [9]. For device applications, the use of individual molecules as functional structure was first proposed in the 1974 (A. Aviram and M. A. Ratner). Currently, at laboratory level, semiconducting and magnetic nanowires are assembled into nanometer scale field-effect transistors, p-n diodes, light emitting diodes, bipolar junction transistors, and complex logic gates circuits [10–15].

1.1.1   Growth of Nanostructures

The ability to produce high quality nano dimensional structures is central to modern science and technology today. The fabrication and reproducibility of nano materials are not a trivial task and there are currently no fully satisfactory strategies that can allow the reproducibility assembly of large numbers of nanostructures into large numbers of logic functional assemblies. Due to increasing studies of nano materials in the last several years, a variety of materials synthesizing methods have been re-examined and modified for the existing strategies. Methods for fabricating nanomaterials and devices below 100 nm include both top down and bottom up approaches.

The top down approach

In a top-down approach, nanostructures are directly fabricated in bulk materials by lithographic techniques such as electron beam lithography, photolithography, atomic

force microscopy (AFM), dip-pen nanolithography (DPN) and scanning tunneling microscopy (STM) and so on. They are used to manipulate, machining, patterning, cut, and shape materials into the desired nano shapes. The top-down approach has been exceedingly successful in many venues, with microelectronics being perhaps the best example today.

The bottom up approach

In the bottom up approach, the nanostructures are synthesized by molecular beam epitaxy (MBE) or direct chemistry methods or self-assembly. MBE, developed by Bell lab's J. R. Arthur, A. Y. Cho, and A. C. Gossard in late 1960's, builds large structures by precise layers of atoms and molecules. MBE is also widely used to make samples and devices for the newly emerging field of spintronics which will be one of the main subjects of this thesis. Other growing popular methods in this category are (i) Chemical vapor deposition (C. M. Lieber and *et al.*,1995; J. Westwater and *et al.*, 1997; C. M. Lieber and *et al.*, 1998; Y. Wu and P. Yang, 2000), (ii) Pressure and anodization process for nano templates (C. R. Martin, 1994; H. Dai and *et al.*, 1995),(iii) Solution-liquid-solid growth (T. J. Trentler *et al.*, 1995; C. M. Lieber and *et al.*, 1995; J. Westwater and *et al.*, 1997; M. S. Gudiksen, C. M. Lieber, 2000; Y. Wu, P. Yang, 2000), and (iv) Electrospinning (D. Reneker and *et al.*, 1995; Hohman and *et al.*, 2001; Matthews *et al.*, 2002; Li *et al.*, 2003; Xia *et al.*, 2004; Subramanian *et al.*, 2005). The process of self-assembly lends itself naturally to controlling the local placement of molecules and it can be observed in many biological, chemical, and physical processes (Ulman, 1991; Ulman, 1996). This method has been recently explored as a way to produce molecular assemblies in a straightforward manner and has been strategically manipulated to form nanostrcuture patterns. (Allara, 1995; Brain and *et al.*, 1989; Bain and Whitesides, 1990; Ulman, 1996). The most commonly

studied and well-characterized systems are alkanethiolate self-assembled monolayers (SAMs) on Au (111) (Dubois and Nuzzo, 1992; Poirier, 1997).

1.1.2 Density of States

What makes nanomaterials unique is their electron density of states (DOS) are different than that of bulk materials, for example, when 1D nanowires having thickness (d) value is the order of or smaller than mean free path of conduction electrons L_m, the resistivity of the materials is changed from case of bulk materials. Due to of large
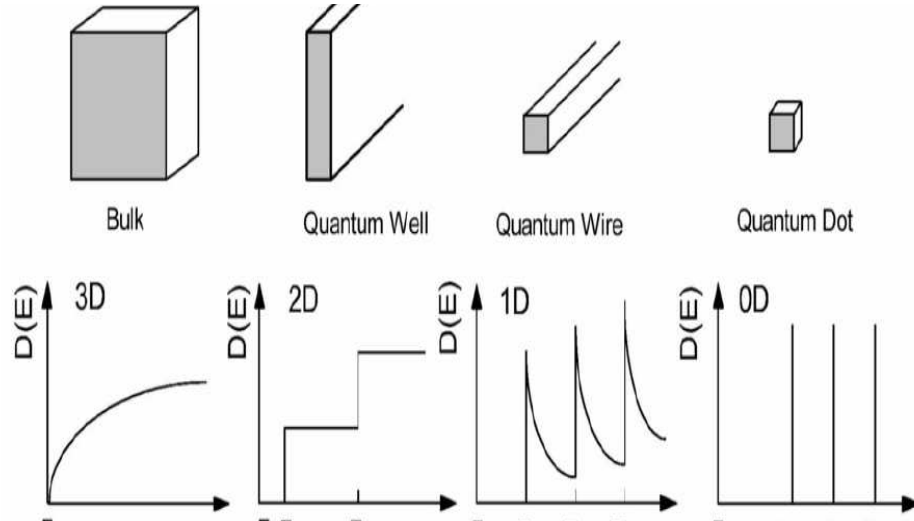
Figure 1.2 Electronic density of states for 1) a bulk 3D crystalline , 2) a 2D quantum well, 3) a 1D nanowire or nanotube, and 4) a 0D quantum dot [Ref. 16]

surface-to-volume ratio of the 1D materials, the energy spectrum in reduced dimensions becomes quantized, causing a remarkable difference in the electron DOS. Unlike the parabolic shape of the DOS for bulk materials, the spike-like shape of the DOS for a 1D nanowire exhibits an increased DOS[1] [16] near the Fermi level (Fig. 1.2)

---

[1]This phenomenon is known as the *quantum confinement effect*

1.1.3   Electrical Conduction Mechanism in Nanostructures

Let's recall the Fuchs-Sondheimer's model which well explains classical size effects and electric transport properties of micron, submicron, mesoscopic systems [17]:

$$\rho = \rho_0 \left\{ \frac{1}{3[\frac{1}{3} - \frac{\alpha}{2} + \alpha^2 - \alpha^3 ln(1 + \frac{1}{\alpha})]} + \frac{3}{8}C(1-p)\frac{1 + AR}{AR}\frac{L_m}{d} \right\} \qquad (1.1)$$

Here, $\alpha = \frac{L_m}{a}\frac{R_C}{1-R_C}$

Where ρ_0 - the bulk resistivity, d - the wire width, a - average grain sizes, AR - the aspect ratio (wire height divided by wire width), R_C- grain boundary reflective coefficient, p - a specularity parameter related to the reflection from wire surface, C - constant. The first term in the equation is related to grain-boundray scattering, and second term to wire-surface scattering. In this model, the system or sample length, L, is considered much higher than electron mean free length L_e, namely $L \gg L_e$. At nano level, $L \ll L_e$, this semiclassical model fails due to the quantum size effect in which the electron's wavefunction can be obtained from Schrödinger's equation. It has been proposed that at very small, nanochannel length in 1D system or sample, the most of the electrons do not "hit" anything as they travels through the channel from one end to another [18]. In another word, transport through the whole quantum confined region is considered to be coherent, thus only elastic scatterings are allowed. Based on the ballistic transport idea, Rolf Landauer [19] formalized the ideal quantum conductivity in a system consist of a single quantum wire, connecting two electron reservoirs as following:

$$G = \frac{2e^2}{h} \cdot N \qquad (1.2)$$

Where, $G_0 = \frac{2e^2}{h}$ is called the conductance quantum, $N = \frac{2\omega}{\lambda_F}$ - the number of conduction channel, ω - the cross section of the quantum wire, λ_F - The Fermi wavelength. It may look strange that an ideal wire without any scattering has finite resistance, but it can be shown that resistance arises from the interfaces between the reservoirs and

the wire.

1.1.4   Ferromagnetic Nanostructures

In recent years ferromagnetic nanowires have attracted considerable interest due to their potential use in many areas of advanced nanotechnology, specifically, *spintronics* and *magnetostriction* device applications which can operate at room temperature. Despite the potential impact of the fields, ferromagnetic nanowire devices remain relatively undeveloped, necessitating a more intimate understanding of more detailed fundamental properties in those nano materials. Very few works are reported on spin-polarized (magneto) transport and magnetorestriction across nanowires, which are hindered by difficulties with fabrication processes, small sample volumes and connecting to individual nanostructures. Until recently spin of electrons, the intrinsic angular momentum of the electron, was ignored in conventional microelectronics. The spin of electrons is quantized such that, whenever it was measured it would yield either spin-up $(+h/2)$ or spin-down $(-h/2)$ projections [20]. Magnetoresistance or spin-dependent transport involves the study of control resistivity of materials by manipulation of spin degrees of freedom under various magnetic field that could be revolutionize today's digital electronics. The magnitude of magnetoresistance (MR) is usually defined as:

$$MR = \frac{(\rho_H - \rho_0)}{\rho_0} = \frac{\Delta\rho}{\rho_0} \tag{1.3}$$

Where, $\Delta\rho$ is the change of material resistivity, ρ_0 is resistivity of the material without magnetic field. The MR can be positive and negative due to suppression/alignment of electron spins in a magnetic field. There are four different of magnetoresistance effects have been recorded: 1) anisotropic magnetoresistance (AMR), 2) giant magnetoresistance (GMR), 3) spin-dependent tunneling effect (SDTE), 4) the colossal magnteoresitance (CMR). Physical explanations behind these effects are very differ-

ent. About 150 years ago, W. Thomson (Lord Kelvin) observed that there is a small effect of the magnetization direction on the resistivity in ferromagnetic metals [21]. This behavior is called as the *anisotropic magnetoresistance* (AMR). The AMR effect depends on the angle between the electric current magnetization directions. When the current is parallel to the magnetization direction, the resistivity of a ferromagnetic material, $\rho_\parallel$ is increase and a case for current is perpendicular to the field, $\rho_\perp$ is decrease. The material with one of the largest AMRs at room temperature is a perm alloy ($Ni_{80}Fe_{20}$) which has an MR of a 5%. The physical origin of this phenomenon is based on the applied field being able to tilt the orbital angular momenta of the $3d$ orbitals, which changes the scattering of the conduction electrons according to their direction of travel proposed by Mott (1936). He further extended the theory (Mott 1964) and realized that at sufficiently low temperatures, where magnon, collective excitation of the electron's spin structure in crystal lattice, scattering becomes vanishingly small, electrons of majority and minority spin, with magnetic moment parallel and antiparallel to the magnetization of a ferromagnet, respectively, do not mix in the scattering processes. The conductivity can then be expressed as the sum of two independent and unequal parts for two different spin projections - the current in ferromagnets is spin polarized. This is also known as the two-current model and has been further developed by Campbell *et al.*, (1967); Fert and Campbell, (1968); Farrell and Greig, (1968). It continues, in its modifications, to provide an explanation for various magnetoresistive phenomena by Schwerer and Conroy (1971); Valet and Fert (1993).

Julliere reported in 1975 an increase in MR nearly 14% at 4.2 K when the magnetic junctions in Co/Ge/Fe switched from the parallel (P) to the antiparallel (AP) configuration, however MR at room temperature was below 1%. This phenomenon is called *tunneling magnetoresistance (TMR)* and it shows much stronger magne-

toresistance than the typical AMR effect [22]. In 1982, Maekawa and Gafvert [23] repeated Julliere's experiment in Ni/NiO/Co junctions and observed TMR=2% at room temperature. In 1991, T. Miyazaki and *et al.*, observed TMR=2.7% at room temperature in $82Ni - Fe/Al_2O_3/Co$ junctions [24]. Tunneling measurements played a key role in early experimental work on spin-polarized transports studying mostly in Ferromagnetic/Nonmagnetic/Ferromagnetic junctions, (Y. Suezawa and *et al.*, 1992; R. Kabani, J. S. Moodera and *et al.*, 1990; J. Nowak and *et al.*, 1992; P. LeClair, J. S. Moodera and *et al.*, 1994). The revolutionary results were found in 1995 by J. S. Moodera's group [25] and they demonstrated that greater than 10% TMR at room temperatures that quickly garnered great deal of attentions and catalyzed many groups to investigate tunneling magneto resistance effect.

The giant magnetoresistance is present for ferromagnetic layers which are separated by a non-magnetic or an anti-ferromagentic metallic thin film and the pioneering work was carried out by Peter Grünberg's group in 1988 on Fe/Cr/Fe tri-layers and Albert Fert's group in 1989 on Fe/Cr multilayers [26]. The magnitude of the electric current and thus the resistance depend on the relative orientation of the magnetization in the thin film systems. The resistance is low (large) for a parallel (anti-parallel) alignment of the magnetization of neighbored magnetic layers. Thus, in layered systems with an anti-ferromagentic coupling the parallel orientation forced by an external magnetic field significantly reduces the resistance. GMR can be extremely large about the 80%. The magnitude of the Giant Magnetoresistance (GMR)is determined as:

$$\lambda = \frac{\rho_{antiparallel} - \rho_{parallel}}{\rho_{parallel}} \tag{1.4}$$

Sensitive read-out heads were needed to be able to read data from the compact hard disks or data storages. In 1997, the first read-out head based on the GMR effect was launched and this soon became the standard technology. Based on their GMR

discovery, A. Fert and P. Grünberg were awarded the 1997 Nobel prize in Physics. Spins are scattered by grain boundaries, carriers, and impurities and spin diffusion length is strongly dependent on the crystallinity of the material. A better understanding of spintronics, specially in nano structures is current milestone of microelectronics in which we are expecting increased data processing speed and decreased electric power consumptions.

Another important part of this thesis is characterization of magnetorestrictive material $Fe_{1-x}Ga_x$. The magnetorestriction effect, one of the special properties of ferromagnetic materials, is the change in a material's dimension caused by a magnetic field. The magnitude of magnetorestriction constant, λ , is usually defined as:

$$\lambda = \frac{\Delta l}{l_0} \tag{1.5}$$

Where, Δl is the change of material dimension, l_0 is the original length of the material. The λ depends on the crystal direction and maybe positive (extension) or negative (contraction) [27]. Further it also depends on applied field and can even change its sign when the field is increased. Examples of magnetostrictive materials include the common ferromagnetic materials Fe, Ni and Co. By alloying metals, one can control λ. The prospect of developing a mechanically robust magnetostrictive material with high λ has motivated scientific community. Recently, it has been shown that a partial substitution of Fe atoms with Ga atoms, in the Fe bcc crystal structure, creates an active material known as galfenol with approximately ten times the magnetostrictive than that of pure Fe (Clark 2000). The miniaturization of magnetostrictive devices at the micro- and nanoscales may also have the potential for an impact in many areas of science and technology. Processing and characterization iron-gallium nanowires are one of aims of the this disseration work, therefore, we will also more talk about crystal structure and properties of Fe-Ga system in next Chapter.

1.2 Purpose

Current interest in research on one-dimensional (1D) ferromagnetic nanostructures is stimulated by the potential application to future *spintronics* and *magnetostriction* devices. Vitreous State Laboratory of The Catholic University of America has established several projects in its efforts to develop nanotechnology for the creation of future nanoscale spintronics and magnetostrictive devices. The author of this dissertation has worked on nano-scale device project processing of variety ferromagnetic nanowire materials. This project is responsible for developing the processing and characterization and integrating technologically important Sr and Ca doped pervoskite lanthanium manganities and iron gallium (galfenol) electrospun nanowire materials. The electrospinning method is a promising route to synthesize a large-area, high-quality, ordered nanostructure with high aspect ratio, which is difficult to form by the conventional lithographic process and other nanostructure fabrication methods. The objectives of this work are: (i) Tailor the electrospinning method to grow oxide and intermetallic magnetic nanostructures, (ii) focus on growth of the colossal magnetoresistance (CMR) pervoskite lanthanium manganitie nanowires as well as gallium iron nanowires, (iii) study morphology and structural characterization of the nanowires, (iv) investigate magnetic and optical properties of the nanowires, (v) fabricate nanoscale devices on the nanowires to understand the properties at nanoscale for device applications, (vi) characterize the devices at a wide range of temperature under various magnetic field. The doped pervoskite manganites exhibit interesting electrical and magneto-transport properties such as high degree spin polarization and large colossial magnetoresistance (CMR) [28]. Among the most studied of these materials are $La_{0.67}Sr_{0.33}MnO_3$ (LSMO) and $La_{0.67}Ca_{0.33}MnO_3$ (LCMO). Interestingly, LSMO show nearly all of their conduction electrons spin-polarized at the Fermi-level

are known as transport half-metallic ferromagnets [29]. On the other hand, for high-power actuator applications, high strain at low fields is important. Galfenol is an emerging new magnetostrictive material that possesses fundamental advantages [30]. Recent new studies of spin-dependent transport and magnetic properties of nanowire materials have been employed for several different materials fabricated by mostly electrodeposition method. For example, manganite nanowires have been grown by anodized alumina oxide template and by the pulsed laser deposition methods by other groups, nanowires grown from these techniques are difficult to use for device fabrication. For nanostructured galfenol, it is very rarely studied due to difficulty of growing high-quality materials. In addition to its magnetostrictive properties, we are interested in additional properties of galfenol such as magnetoresistance properties and considered it part of this work. Undertaking a systematic study involving growth, structure, magnetic properties and device characterization of the electrospun doped lanthanium manganite and galfenol nanowires is the content of this thesis and these had not been performed until now.

1.3   Scope

The work described in this thesis focuses on the synthesis, structural analysis, magnetic and optical properties, spin-dependent transport in one dimensional metallic transport channels. The spin transport properties are investigated in ($La_{0.67}Sr_{0.33}MnO_3$ and $La_{0.67}Ca_{0.33}MnO_3$ and $Fe_{100-x}Ga_x$ ($15 \leq X \leq 27$)) nanowires with different sizes. The outline of the thesis is the following:

- In Chapter 1, introduction, purpose and scope of the thesis are presented.

- In Chapter 2, an introduction of colossal magentoresistance and magnetostrictive galfenol phenomenas, and the materials crystal structures and properties

are discussed.

- In Chapter 3, detailed description of the state-of-the-art electrospinning process is given.

- In Chapter 4, measurement techniques that were used in this dissertation work are presented

- In Chapter 5, growing detail processes of $La_{0.67}Sr_{0.33}MnO_3$ and $La_{0.67}Ca_{0.33}MnO_3$ nanowires are presented. The wires are grown by tailoring electrospinning method on Si and Quartz substrates. Detailed experimental procedures, aqueous solutions preparation, optimal annealing temperatures and nanowire growing environments are also illustrated. The structural studies were done by X-ray diffraction (XRD), morphologies were examined by scanning electron microscopy (SEM). The magnetic measurements of the as-grown nanowire-ensemble were investigated in different temperature ranges using a superconducting quantum interference device magnetometer (SQUID). Raman spectroscopy was performed under low and moderate laser power exposures and spectra were continuously collected at 1 s intervals. The patterns of nanoscale devices were fabricated on Si/SiO_2 substrates by e-beam lithography. Spin dependent transport properties were measured.

- In Chapter 6, we will introduce growing and processing of high magetostrictive galfenol, $Fe_{100-x}Ga_x$ ($15 \leq X \leq 27$) nanowire materials. Their structure and morphology and magnetic properties are investigated. Single galfenol nanowire devices are fabricated on Si/SiO_2 substrates and spin-dependent transport properties were investigated in the devices.

- In chapter 7, summary of this thesis work are given.

Bibliography

[1] Norio Taniguchi, *On the Basic Concept of Nano-Technology*, Proc. Intl. Conf. Prod. Eng, Part II, Japan Society of Precision Engineering, Tokyo, (1974)

[2] Richard Feynman, *There's Plenty of Room at the Bottom, American Physical Society Meeting*, Caltech, December, (1957)

[3] Gordon Moore, *Cramming more components onto integrated circuits*, Electronics, 38(8), (1965)

[4] D. Neamen, *Semiconductor physics and devices*, McGraw-Hill Science Engineering Math, 3rd edition, (2006)

[5] S. Ijima, T. Ichihashi, *Single-shell carbon nanotubes of 1-nm diameter*, Nature 363, 603, (1993)

[6] D. S. Bethune, C. H. Kiang, M. S. De Vries, G. Gorman, R. Savoy, *et al.*, *Cobalt catalysed growth of carbon nanotubes with single-atomic-layer walls*, Nature 363, 605 (1993)

[7] T. J. Trentler, K. M. Hickman, S. C. Goel, A. M. Viano, P. C. Gibbons, W. E. Buhro, *Solution-Liquid-Solid Growth of Crystalline III-V Semiconductors: An Analogy to Vapor-Liquid-Solid Growth*, Science, Vol 270, 5243, (1995)

[8] A. M. Morales and C. M. Lieber, *A Laser Ablation Method for the Synthesis of Crystalline Semiconductor Nanowires*, Science, Vol. 279, 9 (1995)

[9] F. X. Redl, K. S. Cho, C. B. Murray and S. OBrien, *Three-dimensional binary superlattices of magnetic nanocrystals and semiconductor quantum dots*, Nature, 423, 938, (2003)

[10] H. Dai, E. W. Wong, Y. Z. Lu, S. Fan, and C. M. Lieber, *Synthesis and Characterization of Carbide Nanorods*, Nature, 375, 769 (1995).

[11] C. Joachim, J. K. Gimzewski, R. R. Schittler and C. Chavy *Electronic transparence of a single $C_{-}60$ molecule*, Phys. Rev. Lett. 74, 2102 (1995)

[12] S. J. Tans and *et al.*, *Individual single-wall carbon nanotubes as quantum wires*, Nature 386, 474, (1997)

[13] P. Kim and C.M. Lieber, *Nanotube Nanotweezers*, Science 286, 2148 (1999)

[14] J. Hu, T. W. Odom, and C. M. Lieber, *Chemistry and Physics in One Dimension: Synthesis and Properties of Nanowires and Nanotubes*, Acc. Chem. Res. 32, 435 (1999)

[15] P. Kim, T. W. Odom, J. L. Huang and C. M. Lieber, *Electronic Density of States of Atomically Resolved Single-Walled Carbon Nanotubes, Van Hove Singularities and End States*, Phys. Rev. Lett. 82, 1225 (1999)

[16] Equation (8.63) in N.W. Ashcroft, N. D. Mermin, *Solid State Physics*, Holt Rinehart and Winston, Philadelphia (1976); M. S. Dresselhaus, G. Chen, M. Y. Tang, R. Yang, H. Lee, D. Wang, Z. Ren, J. P. Fleurial, and P. Gogna, *New Directions for Low-Dimensional Thermoelectric Materials*, Adv. Mater., 19, 1, (2007)

[17] K. Fuchs, *The conductivity of thin metallic films according to the electron theory of metals*, Proc. Cambridge Philos. Soc, 34, 100, (1938); E. H. Sondheimer, *The influence of a transverse magnetic field on the conductivity of thin metallic films*, Technical Report No. 161, MIT, (1950); W. Steinhgl, G. Schindler, G. Steinlesberger, M. Traving, and M. Engelhardt, *Comprehensive study of the resistivity of copper wires with lateral dimensions of 100 nm and smaller*, Journal of Applied Physics, 97, 023706 (2005)

[18] S. Datta, *Electronic Transport in Mesoscopic Systems*, Cambridge University Press, (1995)

[19] R. Landauer, *Spatial variation of currents and fields due to localized scatterers in metallic conduction*, IBM J. Res. Dev, 1, 223 (1957).

[20] J. J. Sakurai, *Modern Quantum Mechanics*, Addison Wesley, (1993)

[21] S. Maekawa and T. Shinjo, *Spin dependent transport in magnetic nanostructures*, CRC Press; 1st edition, (2002)

[22] M. Julliere, *Tunneling between ferromagnetic films*, Phys. Lett. 54A, 225, (1975)

[23] S. Maekawa and U.Gafvert, *Electron Tunneling Between Ferromagnetic Films*, IEEE Transactions on magnetics,18,(2),707, (1982)

[24] T. Miyazaki, T. Yaoi and S. Ishio, *Large magnetoresistance effect in* $82\text{Ni} - \text{Fe}/\text{Al}_2\text{O}_3/\text{Co}$ *magnetic tunneling junction*, J. Magn. Magn. Mater, 98, L7, (1991)

[25] J. S. Moodera, Lisa R. Kinder, Terrilyn M. Wong, and R. Meservey, *Large Magnetoresistance at Room Temperature in Ferromagnetic Thin Film Tunnel Junctions*, Phys. Rev. Lett. 74, 3273, (1995)

[26] P. Grünberg, R. Schreiber, and Y. Pang, *Layered Magnetic Structures: Evidence for Antiferromagnetic Coupling of Fe Layers across Cr Interlayers*, Phys. Rev. Lett. 57, 2442 (1986); M. Johnson and R. H. Silsbee, *Spin-injection experiment*, Phys. Rev. B, 37, 5326, (1988); M. N. Baibich, J. M. Broto, A. Fert, F. Nguyen Van Dau, and F. Petroff, *Giant Magnetoresistance of (001)Fe/(001)Cr Magnetic Superlattices*, Phys. Rev. Lett. 61, 2472 (1988)

[27] D. Jules, *Introduction to Magnetism and Magnetic Materials*, Chapman Hall, (1991); R. Von Helmholt, J. Wecker, B. Holzapfel, L. Schultz, and K. Samwer, Phys. Rev. Lett, 71, 14, (1993)

[28] A. Urushibara, Y. Moritomo, T. Arima, A. Asamitsu, G. Kido, Y. Tokura, *Insulator-metal transition and giant magnetoresistance in $La_{1-x}Sr_xMnO_3$*, Phys. Rev B, 51, 14103, (1995); R. Von Helmolt, J. Wecker, B. Holzapfel, L. Schultz and K. Samw, *Giant negative magnetoresistance in perovskitelike $La_{2/3}Ba_{1/3}MnO_x$ ferromagnetic films* Phys. Rev. Lett., 71, 2331, (1993)

[29] B. Nadgorny, I. I. Mazin, M. Osofsky, R. J. Soulen, Jr. P. Broussard, R. M. Stroud, D. J. Singh, V. G. Harris, A. Arsenov, and Ya. Mukovskii, *Origin of high transport spin polarization in $La_{0.7}Sr_{0.3}MnO_3$: Direct evidence for minority spin states* Phys. Rev B, 63, 184433, (2001)

[30] A. E. Clark, J. B. Restorff, M. Wun-Fogle, T. A. Lograsso, D. L. Schlagel, D.L., *Magnetostrictive properties of body-centered cubic Fe-Ga and Fe-Ga-Al alloys*, Magnetics, IEEE Transactions on magnetics, 36, 5, (2000)

Chapter 2

Colossal Magnetoresistance and Magnetorestriction Effects

2.1 Perovskite Type Manganese Oxides

In 1950, Jonker and Van Santen discovered that in the doping range $0.2 \leq x \leq 0.5$, transition metal pervoskite $La_{1-x}M_xMnO_3$ (M=transition metal Sr, Ca, Ba) is a ferromagnetic metal at low temperature and a poorly conducting paramagnet at high temperature and the ferromagnetic-paramagnetic transition occurs at the metal-insulator transition temperature T_c [1]. One year later, Zener gave an explanation for the experimental result in which why antiferromagnetic and insulating $LaMnO_3$ show ferromagnetism and become a conductive material when it is doped by divalent Sr, Ca and Ba and proposed idea of the double exchange (DE) model [2]. The DE model considers the mechanism of interaction between electrons in the incomplete d shells in the ferromagnetic manganites. Large magnetoresistance (MR) near the Curie temperature in perovskite-type manganese oxides was first reported in 1969 by Searle and Wang for a flux-grown crystal of $La_{1-x}Pb_xMnO_3$ [3]. However interest in

17

the perovskite-type manganese oxides had not renewed until the discovery of high-temperature superconductivity in oxides. At room temperature a large magnetoresistance of 60% has been observed in 1993 by R. von Helmolt *et al.*, in thin magnetic films of perovskite-like La-Ba-Mn-O [4]. The films were grown epitaxially on SrTiO3 substrates by off-axis laser deposition. McCormack, Jin and others in 1994 observed a magnetoresistance with even more than 99.90%[1] at 77 K, under H=6 T in epitaxially grown La-Ca-Mn-O thin films [5]. In Fig. 2.1 is shown a typical example of the MR feature observed for a single crystal of $La_{1-x}Sr_xMnO_3$ and $La_{1-x}Ca_xMnO_3$ where an external magnetic field cause the gigantic decrease of the resistivity around the Curie temperature (T_c) [6, 7]. Below T_c the resistivity also shows a steep decrease with decreasing temperature in zero magnetic field. The such gigantic negative MR effect
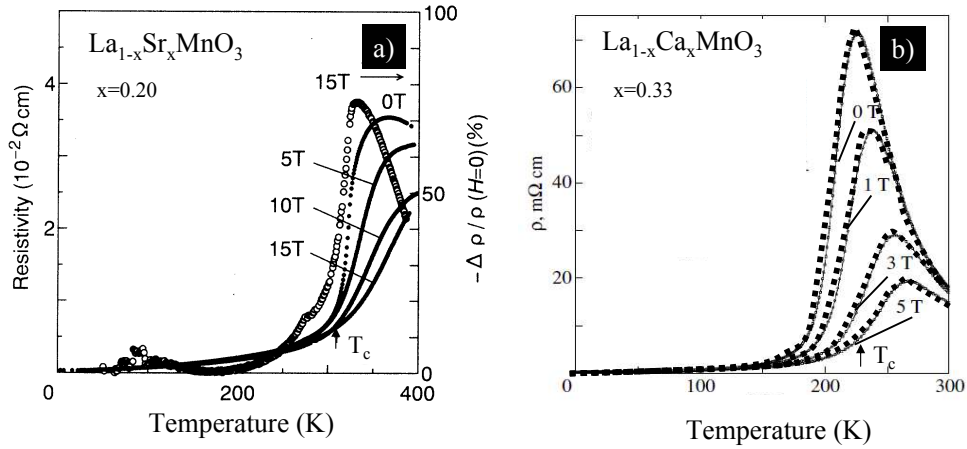
Figure 2.1 Temperature profile of resistivity of a perovskite-like a) $La_{1-x}Sr_xMnO_3$, b) $La_{1-x}Ca_xMnO_3$ single crystal under several magnetic fields applied parallel to the electric current. [6, 7]

was named *the colossal magnetoresistance* (CMR). Its property is not explained fully by any current physical theories. Several models have been explained ferromagetism and carrier transport properties of the various doped perovskite manganites extend-

---

[1]In the paper, $MR = \frac{\Delta \rho}{\rho_H}$ which gives a value of 127000%

ing the Zener's DE model. For example, Anderson and Hasegawa (1955) [8], P.G. de Gennes (1960) [9] and K. Kubo and N. Ohata (1972) [10]. Huge interest in the MR of doped lanthanium manganites has revived more lately since the rediscovery of the CMR.

2.1.1   Crystallographic Structure

The crystallographic structures for the $La_{1-x}Ca_xMnO_3$, a member of the perovskite like manganites, were determined in 1955 by Wollan and Koehler in a remarkably complete neutron and X-ray diffraction study as a function of Mn^{4+} content [11]. The undoped lanthanum manganite has the chemical formula $La^{3+}Mn^{3+}O_3^{2-}$. Each manganese ions are surrounded by six oxygen ions in form of an octahedral configuration that has a highly distorted perovskite crystal structure. The driving force for the lattice distortion is the *Jahn-Teller* effect (H. A. Jahn, 1937 and 1938). This crystal structure can be regarded as a three-dimensional network of corner sharing MnO_6 octahedra (Fig. 2.2 a). Eight octahedra form a cube with the A site in its center (Fig. 2.2 b). The A site is twelve-fold surrounded by oxygen ions. But typically the ionic radius of the A ion is smaller than the volume, enclosed by the oxygen ions. This volume can be reduced by rotating the octahedra with respect to each other. Ideal, undoped perovskites are electrically insulators and show antiferromagnetism, all the atomic sites are filled, and strong ionic bonds keep the atoms and their electrons in place making it difficult for electrons to move through the crystal. More interesting physics arise when it is doped by divalent Sr^{2+} or Ca^{2+} (doping ranges x=0.2 - 0.40) and become metallic and show ferromagnetism. Structurally, $3d$ transition metals Sr or Ca make the distortion reduce in the original perovskite structure (Fig. 2.2 c-d). The larger size La trivalent ions and Sr or Ca divalent ions occupy the A-site with 12-fold oxygen coordination. The smaller Mn ions in the

mixed-valence state Mn^{3+}- Mn^{4+} are located at the center of an oxygen octahedron, with the B-site with 6-fold. For the stoichiometry, the proportions of Mn ions in the valence states 3+ and 4+ are respectively, (1-x) and (x). The structure of the manganites is governed by the tolerance factor $t=(r_{La}+r_{oxygen})/\sqrt{2}(r_{Mn}+r_{oxygen})$. The perovskite structure is stable for 0.89< t <1.02, when $t=1$ that corresponding to the perfect cubic closely packed structure. Generally, t differs appreciably from 1
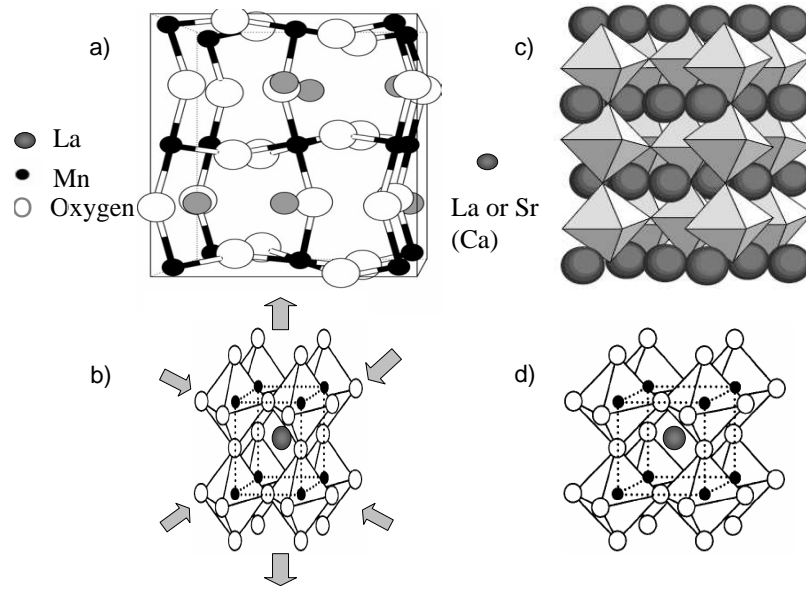
Figure 2.2 a) Undoped $LaMnO_3$ structure, b) Distorted Jahn-Teller type MnO_6 octahedra [8, 12], c) Sr or Ca doped $LaMnO_3$ structure, d) After doping, MnO_6 octahedra shows regular octahedra

and the manganites have, at least at low temperature, a lower rhombohedral symmetry or orthorhomic structure. An important structure derived from the perovskite structure is the Ruddlesden-Popper series or the so-called layered perovskite structure. $(La,M)_{n+1}Mn_nO_{3n+1}$, in which the n-sheets of the Mn-O layer form an isolated building block. For example, the single-layered (n=1) compounds, $(La_{1-x}Sr_{1+x}O_4)$ are insulator with the antiferromagnetic ground states over the whole nominal hole concentration (x) (Here x represents the doped hole concentration in the Mn^{3+} based insulator (x=0).) When n=2, $(La_{2-2x}Sr_{1+2x}Mn_2O_7)$ consist of Mn bilayers separated

from each other by non-magnetic layers exhibit ferromagnetic metallic state; n=∞ corresponds to the usual three-dimensional perovskite.

2.1.2 The Double Exchange Model

The doped lanthanum perovskite manganites can be regarded as solid solutions between $LaMnO_3$ and $SrMnO_3$ or $CaMnO_3$ (replacing a part of the La atoms by Sr or Ca) with formal valence states $La^{3+}Mn^{3+}O_3^{2-}$ and $Sr^{2+}Mn^{4+}O_3^{2-}$ or $Ca^{2+}Mn^{4+}O_3^{2-}$, leading to mixed-valence compounds such as $(La_{1-x}^{3+}Sr_x^{2+})\,(Mn_{1-x}^{3+}\,Mn_x^{4+})\,O_3$ or $(La_{1-x}^{3+}Ca_x^{2+})\,(Mn_{1-x}^{3+}Mn_x^{4+})O_3$. The nominal electronic configurations of Mn^3 and
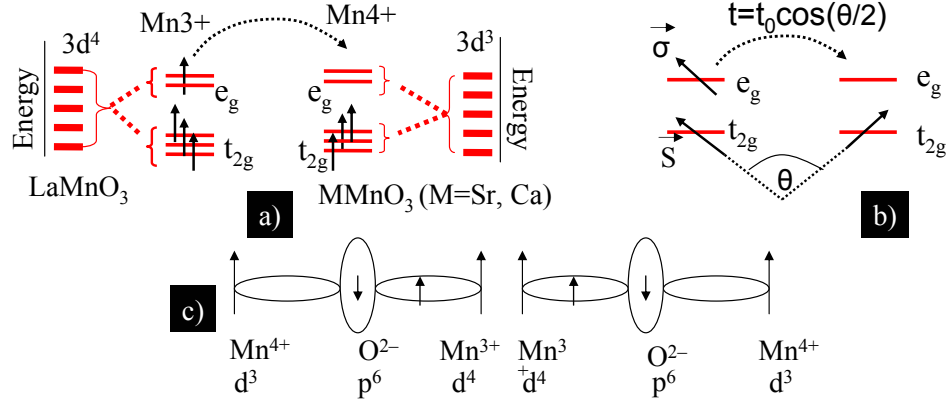
Figure 2.3 a) $LaMnO_3$ and $LaMnO_3$(M=Sr, Ca, Ba) octohedra crystal field splitting of five-fold degenerate atomic $3d$ levels into lower t_{2g} (triply degenerated) and higher e_g (doubly generated) levels, e-f) An illustration of the concept of DE-the hopping matrix element as a function of spin alignment [8, 12].

Mn^4 are $3d^4$ and $3d^3$ respectively. From the crystal field theory, orbital splitting of the MnO_6 octahedral is shown in Fig. 2.3 a. The five d orbitals are split by a cubic crystal field into three t_{2g} and two e_g orbitals. Splitting between the lowest t_{2g} level and the highest e_g level is 1.5 eV [12]. Mn^{3+} is $3d^4$ with $S=2$, whereas Mn^{4+} is $3d^3$ with $S=3/2$. Sr or Ca doping introduce Mn^{4+} ions in the system and create

$Mn^{3+}-O-Mn^{4+}$ bonds. Zener considered that extra electron on the Mn^{3+} can *travel* or *hop* back and forth between $Mn^{3+}Mn^{4+}$ ions via oxygen and change oxidation states of the ions. Also he pointed out that the interatomic Hund rule exchange was strong and that the carriers do not change their spin orientation when *hopping* from one ion to the next, so they can only hop if the spins of the two ions are parallel. Such a transfer was called the *double exchange* responsible for ferromagnetism for doped manganese oxides. On minimizing the total free energy of the system. Zener found that ferromagnetic interactions are favored when the magnetic atoms are fairly well separated and conduction electrons are present. Zener also found following relationship:

$$\sigma \simeq (\frac{xe^2}{ah})(\frac{T_c}{T}) \tag{2.1}$$

Where, σ-conductivity, T_c-Curie Temperature, a-lattice parameter, h-Planck's constant, e-electron charge. This relation agrees excellently with the data of Jonker and Van Santen. Anderson and Hasegawa (1955), (Ref. [8]) estimated the hopping probability of the e_g electron transfer from Mn^{3+} to neighbouring Mn^{4+} is:

$$t = t_0 cos(\theta/2) \tag{2.2}$$

Where, θ is angle between the neighboring (classical) spins. If θ=0, the hopping is the largest, while if $\theta=\pi$, corresponding to an antiferromagnetic background, then the hopping cancels. The quantum version of this process has been described by Kubo and Ohata (1972), Ref. [10]. Recent theoretical works by Millis, Littlewood and Shraiman (1995) show that double-exchange cannot be enough to explain the physics of magnetoresistance of manganites. Regarding ferromagnetism, their calculations for a model having as an interaction only a large Hund coupling between e_g and t_{2g} electrons led to a T_c prediction between 0.1 eV and 0.3 eV, namely of the order of the bare hopping amplitude and considerably higher than the experimental results.

Thus, it was argued that DE produces the wrong T_c by a large factor. Millis, Littlewood and Shraiman (1995) supported the idea and showed that a resistivity that grows with reducing temperature (insulating behavior) even below T_c [13].

2.1.3 Electrical Conductivity

The phase diagrams of the $La_{1-x}Sr_xMnO_3$ and $La_{1-x}Ca_xMnO_3$ as function of temperature T and doping level x are given in Fig. 2.4. In ($La_{1-x}Sr_xMnO_3$), the low
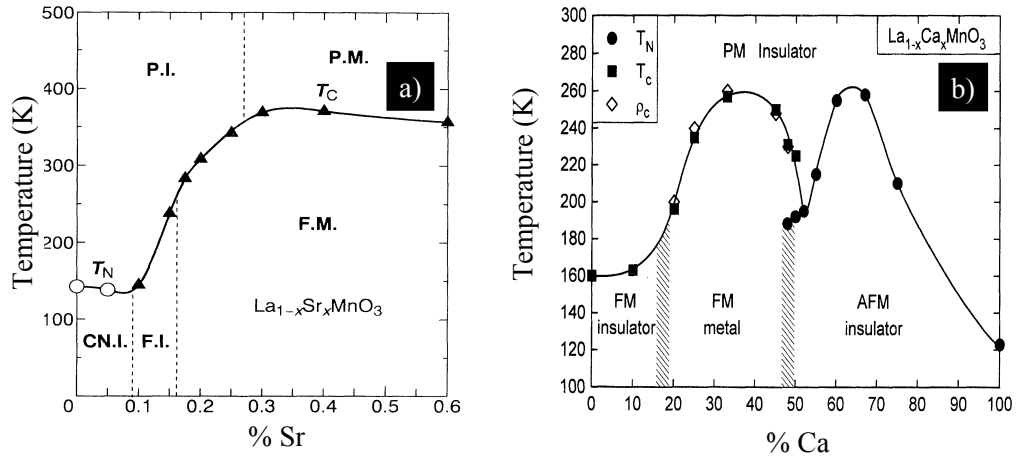
Figure 2.4 a) Electronic phase diagram of ($La_{1-x}Sr_xMnO_3$). Open circles and filled triangles are the Neel T_N and T_c, respectively. The abbreviations mean paramagnetic insulator (PI), paramagnetic metal (PM), spin-canted insulator (SNI), ferromagnetic insulator (FI), and ferromagnetic metal (FM), Reproduced from [6], b) Electronic phase diagram of ($La_{1-x}Ca_xMnO_3$). The transition temperatures are taken as inflection points in M(T) and $\rho(T)$, and T_N for x=0.48 and 0.50 is obtained on warming at H=0.1T [14].

temperature phase is known to be the spin-canted antiferrogametic phase for $0 \leq x \leq$ 0.1 and ferromagnetic phase x>0.1 [15]. The ferromagnetic transition temperature T_c increases with x and reaches the maximum ($\approx$370 K) around x=0.4. Urushibara *et al.*, Ref [6] demonstrated for single crystals of ($La_{1-x}Sr_xMnO_3$) that electronic conduction and magnetic properties vary strongly with doping rate and classified the

(La$_{1-x}$Sr$_x$MnO$_3$) electronic phase into five categories (Fig. 2.4 a). Below the magnetic transition temperature, the three phases are present; a spin canted antiferromagnetic insulator (CNI) is the low doped region (x<0.1), a ferromagnetic insulator (FI) in the region of $0 \leq x \leq 0.15$, and a ferromagnetic metal (FM) in the high-doped region of x>0.15. Above the magnetic transition temperatures (T$_N$ and T$_c$), on the other hand, the non-metal (PI)-to-metal (PM) transition appears to occur around x=0.3. Similar electronic conduction for (La$_{1-x}$Ca$_x$MnO$_3$) is shown in (Fig. 2.4 b) in which x≈0.5, the ground state becomes an insulating antiferromagnet.

2.1.4 Half-metallicity in LSMO

In a typical ferromagnetic materials, for example, nickel has very wide conduction band about 4.5 eV is split into minority and majority carrier bands offset by a small exchange energy about 0.6 eV, leading to partial polarization of the electrons about 23% measured by tunneling (J. C. Phillips *et al.*, 1964). A novel material that predicted to have enhanced spin polarization is called *half-metallic* ferromagnet . It is a metal that has an energy gap at the Fermi level E$_F$ in one of the two spin channels. Only the other channel has states available for transport, and thus the electric current is fully spin-polarized (Fig. 2.5 a-d). Finding half metallic or other highly spin-polarized metals would revolutionize magnetoelectronics, since device performance improves dramatically as the spin polarization of the metal approaches 100% [17]. The spin polzarization is defined as following:

$$P = \frac{n\uparrow - n\downarrow}{n\uparrow + n\downarrow} \tag{2.3}$$

Where, $n\uparrow$ and $n\downarrow$ are density of majority and minority spin electrons at the Fermi level respectively. The polarization is proportional to the magnetization, $P \propto M$, since $M = \mu_B \int (n\uparrow - n\downarrow)dE$.
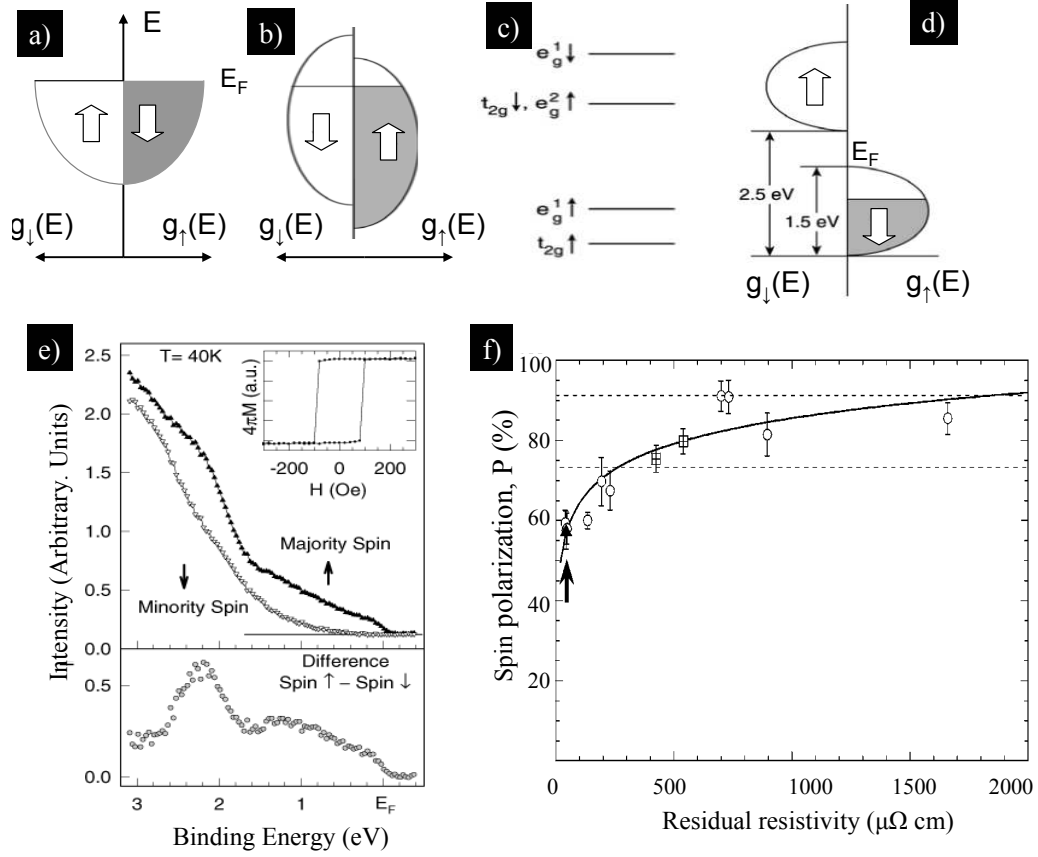
Figure 2.5 A schematic view of the band structure of a) Non-ferromagnetic, b) Ferromagnetic nickel, c) The approximate positions of the 3d bands in undoped $LaMnO_3$, d) ferromagnetic-Sr doped $LaMnO_3$, e) Spin-resolved photoemission spectra of a thin films of $La_{0.7}Sr_{0.3}MnO_3$, f) Spin polarization as a function of the residual resistivity of $La_{0.7}Sr_{0.3}MnO_3$ epitaxial films and a single crystal at T=1.6 K [16, 19, 20].

Some ferromagnetic systems, such as Heusler compounds and chromium dioxide, have been predicted theoretically to be half metallic (de Groot *et al.*, 1983; Schwarz *et al.*, 1986). However, a half-metallic system has not been demonstrated directly and the predictions are still in doubt [18]. Park *et al.*, (1998) concluded from their spin-resolved photoemission spectroscopy measurement that LSMO is completely spin-polarized (Fig. 2.5 e), $P{\approx}100\%$ and $La_{0.7}Sr_{0.3}MnO_3$ show (i) the half-metallic feature well below T_c, for example at 40 K, the spectrum for the majority carriers extends to

E_F and shows a metallic Fermi cutoff, while the spectrum for the minority carriers diminishes around 1 eV binding energy and disappear near E_F, reflecting an insulating gap and (ii) the occurrence of the metal to pseudogap state transition accompanied by loss of the ferromagnetic order on heating through T_c [19]. Spin-resolved tunneling experiments (Yu Lu *et al.*, 1996; J. Z. Sun *et al.*, 1997) indicated incomplete ($P \approx 54\%$ and $P \approx 81\%$, respectively) spin polarization for LSMO. Recent LSMO superconductor tunneling experiments produced a spin polarization of $P \approx 72\%$ (D.C. Worlege *et al.*, 2000). Using the point-contact Andreev reflection technique, B. Nadgorny *et al.*, 2001 cliamed that LSMO is not a half-metal (Fig. **??** f). In this figure, the arrow indicates the lowest resistivity film that was later irradiated with Si ions (shown as squares, the higher resistivity film corresponding to the higher dose). Dashed lines correspond to $P_1 = 74\%$ and $P_2 = 92\%$. Solid line is a guide to the eye. Based on the observation of a clear correlation between the bulk resistivity and the measured spin polarization that is opposite to the one expected for a true half-metal, B. Nadgorny *et al* concluded that high degree of the current spin polarization are $58\% \leq P \leq 92\%$ in bulk $La_{0.7}Sr_{0.3}MnO_3$ [20]. This experiment confirms that LSMO material is a promising candidate for magnetoelectronics applications, since ultimately it is the current spin polarization that controls the performance of these devices. It should be noted that surprisingly, the transport spin polarization was greater for samples with larger residual resistivity. If the material were a true half metal, one might expect the opposite trend: better samples would have less spin-flip scattering and thus show spin polarization closer to 100%. The observed result can be understood, in terms of accounting the dependence of the transport spin polarization on the ratio of the electronic mean free path to the contact size [20]. Therefore $La_{0.7}Sr_{0.3}MnO_3$ can be called a *transport half-metallic ferromagnet*, due to the fact that the spin polarization of the current in this material is approaching 100% in the high resistivity limit.

2.1.5 Applications

After the discovery of giant magnetoresistance (GMR), IBM introduced new classes of magnetically engineered advanced a magnetic random access memory, a type of non-volatile semiconductor memory in 1997 [21]. GMR memories are now found in virtually all hard disk drives produced today and currently, hard disk manufacturing has grown to be 35 billion dollars industry [21, 22]. In a magnetic recording, hard disk drive information is stored by magnetizing regions within a magnetic thin film (Fig. 2.6 a). The transitions between these regions represent *bits* which are detected, via their fringing magnetic fields, by the read sensor. The recording GMR head is attached to a small ceramic slider which is flown on an air bearing above the recording medium at a height of just a few nanometers. The GMR head structure, which is called a spin valve, consists of a stack of four magnetic thin films (Fig. 2.6 c) : (i) a sensing or free magnetic layer, (ii) a nonmagnetic conducting spacer layer, (iii) a magnetic pinned layer, and (iv) an exchange layer. These layers control the resistance of the sensor in response to magnetic fields from the disk. A change in the resistance of the GMR sensor depends on the spin orientation of the conducting electrons and the difference in the magnetization directions of the free and pinned layers [22–24]. The industrial success of the giant magnetoresistance in less than a decade has been fueled an enthusiasm to use collosal magnetoresistance (CMR) effect for more advanced magnetic recording. CMR films having a MR of approximately 95% at room temperature have been compared to GMR films having MR approximately 20% at same condition. Thus a magnetic field CMR sensor would offer a 475% increase in sensitivity providing significantly higher data storage densities. One of the problems of commercialization of CMR sensors is the recording media typically emanates a low field on the order of 20 Oe, which is insufficiently to result in a significant change in resistance in a CMR layer of materials. In laboratory level,
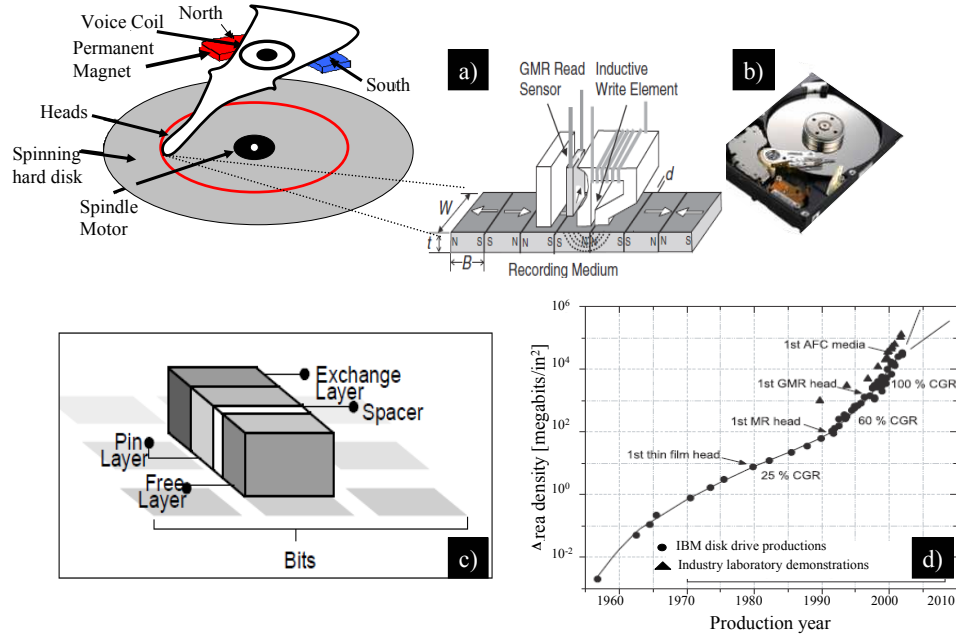
Figure 2.6 a) Magnetoresistive head for hard-disk recording. Schematic structure of the magnetoresistive head introduced by IBM for its hard disk drives in 1991 where B is the bit length, W is the track width and t is the medium thickness, d is the flying height of the head above the medium, b) Hard desk, c) GMR Spin Valve Structure, d) Areal density progress in magnetic recording since its invention [22–24].

several devices have been reported. J. Z. Sun *et al.*, (1996, 1998) reported on the fabrication of a new class of trilayer epitaxial thin film devices based on the doped perovskite manganates LaCaMnO and LaSrMnO. They show that large resistance changes, up to a factor of 2, can be induced by a moderate applied magnetic field below 200 Oe in these trilayers supporting current-perpendicular-to-plane transport. L. E. Hueso *et al.*, (2007) observed large magnetoresistance effects (61% at 5 K), which correspond to large output signals (65 mV), in devices where the non-magnetic channel is a multiwall carbon nanotube that spans a 1.5 mm gap between epitaxial electrodes of the highly spin polarized manganite La-Sr-Mn-O. This spintronic system combines a number of favorable properties that enable this performance; the long spin

lifetime in nanotubes due to the small spinorbit coupling of carbon; the high Fermi velocity in nanotubes that limits the carrier dwell time; the high spin polarization in the manganite electrodes, which remains high right up to the manganitenanotube interface; and the resistance of the interfacial barrier for spin injection.

2.2 Fe-Ga alloys

In 1892, J. P. Joule observed a change of a nickel-rod's physical dimensions when exposed to a magnetic field. Later on, more detailed studies show that when an iron crystal is placed in external magnetic field along an easy direction [100], it gets longer along this direction but contracts in the transverse directions [010] and [001]. This effect is named *magnetostriction* [25]. The magnetorestriction constant is material property defined as:

$$\lambda = \frac{\Delta l}{l} \tag{2.4}$$

It depends on the crystal direction and may be positive (extension) or negative (contraction). Most ferromagnetic materials such as Fe, Co and Ni exhibit some measurable magnetostriction, however, their saturation magnetostriction strain on the order of 10-50 ppm are not sufficient to technological applications. In 1955, E. W. Lee gave a theory [26] for the anisotropic magnetostriction of single crystals using two material constants, *saturation magnetization* and *strain measurement*, as a first approximation in modeling the saturation magnetostriction as in following form:

$$\lambda_s = \frac{3}{2}\lambda_{100}\left(\sum_{i=1}^{3}\alpha_i^2\beta_i^2 - \frac{1}{3}\right) + 3\lambda_{111}\left(\sum_{i,j=1,}^{3}\alpha_i\alpha_j\beta_i\beta_j\right) \tag{2.5}$$

Where, λ_s - saturation magnetostriction, α and β - represent the saturation magnetization and strain measurement directions relative to the crystal axes respectively, λ_{100} and λ_{111} are constans that depend on material properties. For example, the

magnetostriction of body-centered cubic Fe along the easy direction is λ_{100}=20 ppm, and it is anomalous temperature dependence. λ_{100} attains a minimum around 400 K and then again rises to a maximum just before the Curie temperature of Fe [27]. Magnetostrictive materials with high mechanical strength, good ductility, large magnetostriction at low saturation fields and high imposed stress levels, and low associated cost relative materials are of great current interest. Attention has been focused on Fe based alloys because it has a cubic structure that shows enhanced magnetostriction and minimal hysteresis (Clark *et al.*, 1980, 1985). Identifying such an alloy requires a fundamental understanding of magnetostriction in Fe and the influence of alloying elements. Terfenol-D, $Tb_xDy_{1-x}Fe_y$, shows giant magnetostrictive and produces saturation magnetostriction strains in excess of 1,000 ppm [28] at room temperature, but it is very brittle and easily fractured, which makes it difficult to manipulate. In addition, Terfenol-D is expensive to fabricate due to the high costs of Tb and Dy. For high power actuator applications, high strain at low fields is important. Clark *et al.*, (2000) discovered an increase in magnetostriction strain of $\sim$ 400 ppm at a low saturation magnetic field of several hundred oersteds in a $Fe_{100-x}Ga_x$ ($15 \leq x \leq 27$) alloy called as *Galfenol*, which may overcome many problems with Terfenol-D [29]. Recent experimental results indicate that FeGa alloy has a high tensile strength $\sim$ 400 MPa and is machinable [30].

2.2.1   Crystallography

In Fe_xGa_{1-x} system, most interesting phases in the Fe-rich portion for magnetostriction are body centered cubic (BCC) disordered A2, BCC ordered B2-FeGa and α'' ($D0_3$), β ($D0_{19}$) and face centered α-Fe_3Ga ($L1_2$).
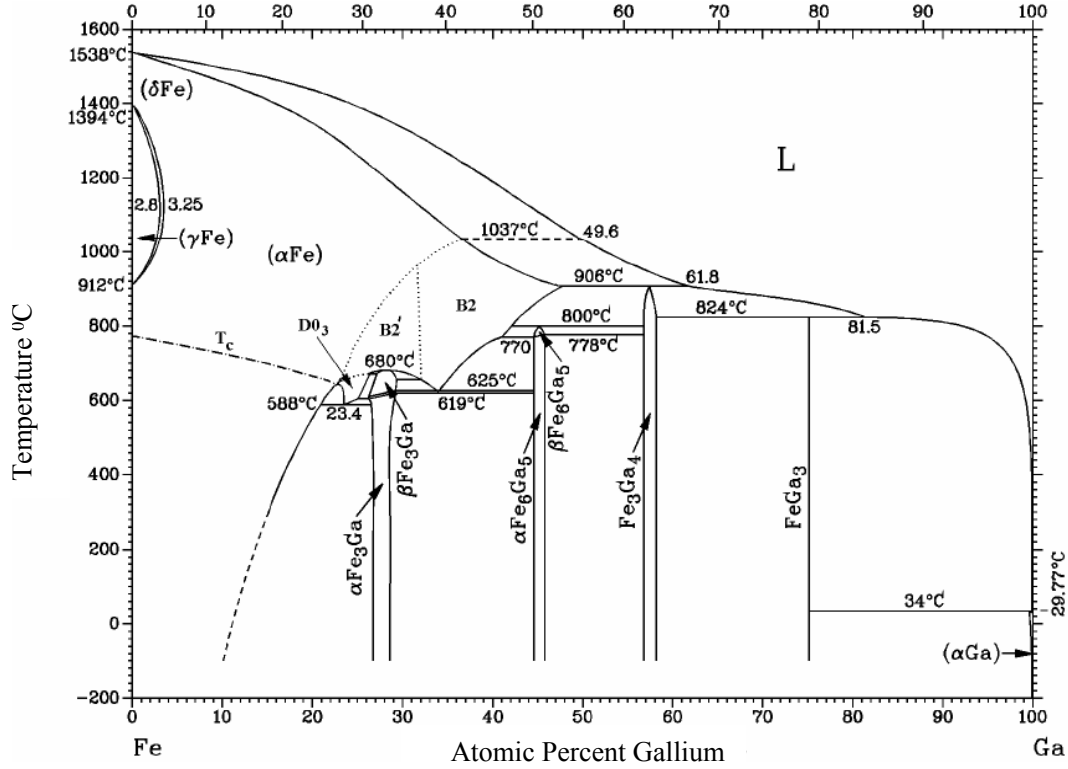
Figure 2.7 The crystal structure of A2, B2 and D0$_3$ in Fe-Ga binary phase diagram [31].

For example, A2 structure extends to x=15, whereas a long-range ordered (LRO) D0$_3$ structure is dominant for x > 23 [31]. For $15 \leq X \leq 23$, a two-phase (B2 and D0$_3$) region can be formed (Fig. 2.7). The space group of D0$_3$ structure is *Fm3m* in which B2 and A2 type structures are stacked alternatively in each direction and its origin is shifted 1/4, 1/4, 1/4 (Fig. 2.8 a-c). Based on transmission and scanning electron-based microscopies with energy dispersion spectroscopy (EDS), Ikeda *et al.*, (2002) observed phase equilibria below 25 at. %Ga almost coincide with the assessed phase diagram, whereas the Fe$_3$Ga (L1$_2$) single-phase region exists up to about 30 at. %Ga and to about 690^0. The phase boundaries between the A2 and D0$_3$ phases including the metastable equilibrium exhibit a complicated behavior (Fig. 2.8 d).
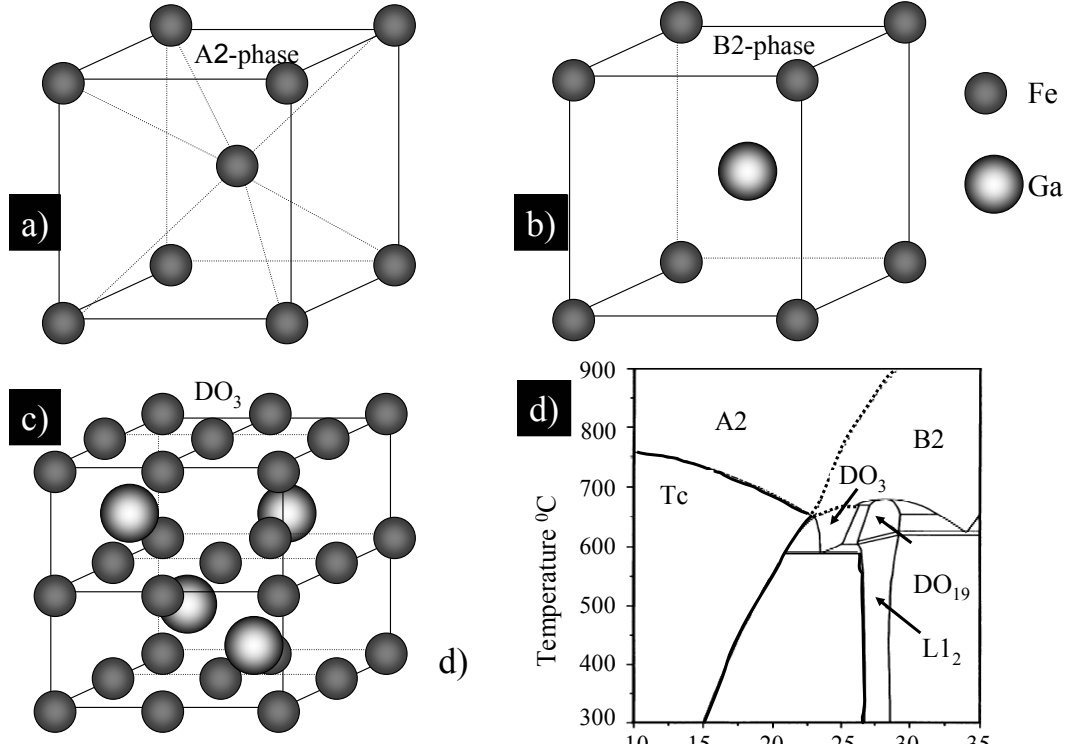
Figure 2.8 a) The unit cell of A2-phase, b) The unit cell of B2-phase, c) The unit cell of D0$_3$-phase, d) Fe-Ga binary phase diagram [33].

Clark *et al.*, [32] proposed that the enhancements of the magnetostriction in Fe-Ga are due to the clustering of the solute atoms in the disordered A2 (α-FeGa) phase to provide both elastic and magnetoelastic defects, which decrease in number as the concentration of solute increase and D0$_3$ and B2 phases emerge. However, in 2002, Wu suggested based on first principles calculations for magnetostrictive coefficients of several ordered Fe$_3$Ga alloys, tetragonal B2-like phase may produces the large positive magnetostriction [34]. More recently a model developed by Cullen *et al.*, [35] explains (001) Ga-Ga pairs may responsible for the high magnetostriction in α-FeGa. However, an understanding of the exact mechanism of magnetostriction in the Galfenol is still remains incomplete.

2.2.2 Magnetostriction

Clark *et al.*, (2000, 2003) measured magnetostriction of $Fe_{100-x}Ga_x$ (4<x<27) prepared by furnace cooling $\sim 10^0 C/min$ and by rapid quenching into water at room temperature [37]. Values of λ_{100} for $Fe_{100-x}Ga_x$ at room temperature are shown in
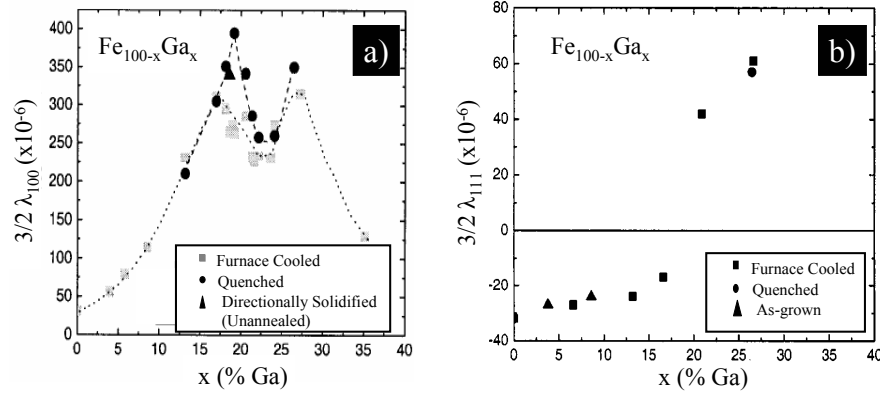
Figure 2.9 Magnetostrictive constants for Fe-Ga single crystal alloys as a function of at.% Ga concentration. a) $\frac{3}{2}\lambda_{100}$ for quenched and furnace cooled heat treatments, b) $\frac{3}{2}\lambda_{111}$ for furnace cooled heat treatment [37].

(Fig. 2.9 a). Interestingly, the results show a double peak in the magnetostriction [100] versus Ga concentration at both cryogenic and room temperatures. Between these peaks λ_{100} has an unusual temperature dependence. Room temperature values for $(3/2)\lambda_{111}$ are displayed in (Fig. 2.9 b) and note that it changes in sign. Entirely different slopes in the magnetostriction versus Ga concentration are found for small x (x<20) than for large x (x>20).

2.2.3 Applications

Magnetostrictive effect can be used for actuation and sensing. Magnetostrictive actuators convert magnetic energy to mechanical energy. Many researchers have used these actuators in smart structures. For example, Bothwell *et al.*, (1995) used a mag-

netostrictive actuator with an extension torsion coupled composite tube to actively control helicopter vibration. Some researchers have developed their own actuators using Terfenol-D rods (R. S. Reed, 1988; M. W. Hiller *et al.*, 1989; A. B. Flatau and J. Pratt, 1993). A compact magnetostrictive actuator, called a magnetostrictive mini-actuator was developed by M. Anjanappa and J. Bi, (1994). The idea is to squeeze a rod of magnetostrictive materials , for example, a schematic of a Terfenol-D actuator manufactured by Etrema Products Inc is shown in Fig. 2.10 [38]. Terfenol-D into
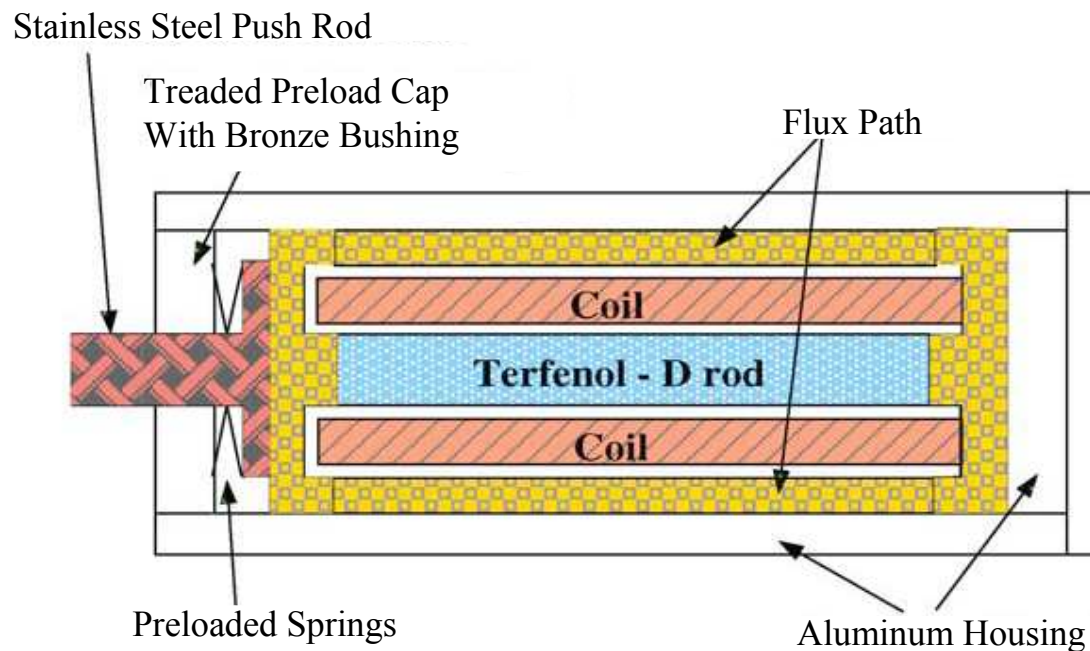
Figure 2.10 A schematic of a Terfenol-D actuator manufactured by Etrema Products Inc   [38].

a metal tube whose bore size is just slightly smaller than the rod's diameter, wrap a series of electromagnetic induction coils around the tube (or stator), and use the coils to generate a moving magnetic field that courses wavelike down the successive windings along the stator tube. As the traveling magnetic field causes each succeeding cross section of Terfenol-D to elongate, then contract when the field is removed, the rod will actually *crawl* down the stator tube like a worm. Repeated propagating

waves of magnetic flux will translate the rod down the tube's length, producing a useful stroke and force output. The amount of motion generated by the material is proportional to the magnetic field provided by the coil system, which is a function of the electrical current. This type of motive device, which features a single moving part, is called an *elastic-wave or peristaltic linear motor* [39]. This type of actuators with galfenol can be embedded inside a laminated composite structure and used for vibration control for adjust or fine-tune the shape of the airfoil cross section of an aircraft wing in flight, reduce aerodynamic drag, boost payload capacity, cut fuel use, and improve maneuverability. Several groups are currently working on to develop and engineer a new class of highly sensitive galfenol sensors for sonar on submarines.

Bibliography

[1] G. H. Jonker and J. H. Van Santen, *Ferromagnetic compounds of manganese with perovskite structure*, Physica, 16(3), 337, (1950); J. H. Van Santen and G. H. Jonker, *Electrical conductivity of ferromagnetic compounds of manganese with perovskite structure*, Physica, 16(7-8), 599, (1950)

[2] C. Zener, *Interaction between the d-shells in the transition metals. II. ferromagnetic compounds of manganese with perovskite structure*, Phys. Rev, 82(3), 403, (1951)

[3] C. W. Searle and S. T. Wang, *Studies of the ionic ferromagnet (LaPb)MnO3 III. Ferromagnetic resonance studies*, Can. J. Phys. 47(23), 2703, (1969)

[4] R. von Helmholt, J. Wecker, B. Holzapfel, L. Schultz, and K. Samwer,*Giant negative magnetoresistance in perovskitelike LaBaMnO ferromagnetic films*, Phys. Rev. Lett, 71(14), 2331, (1993)

[5] M. McCormack, S. Jin, T. H. Tiefel, R. M. Fleming, J. M. Phillips, and R. Ramesh, *Very large magnetoresistance in perovskite-like La-Ca-Mn-O thin flms*, App. Phys. Lett, 64(22), 3045, (1994)

[6] A. Urushibara, Y Moritomo, T. Arima, A. Asamitsu, G. Kidoa, and Y. Tokura, *Insulator-metal transition and giant magnetoresistance in $La_{1-x}Sr_xMnO_3$*, Phys. Rev B, 51(20), 14103, (1995)

[7] T. T. M. Palstra, A. P. Ramirez, S-W. Cheong, B. R. Zegarski and P. Schiffer, *Transport mechanisms in doped $LaMnO_3$: Evidence for polaron formation*, Phys. Rev 56(9), 5104, (1997); C. A. Cardoso, F. M. Araujo-Moreira, M. R. B. Andreeta, A. C. Hernandes, E. R. Leite, A. W. Mombru and R. Faccio, *Physical properties of single-crystalline fibers of the colossal-magnetoresistance manganite $La_{0.67}Sr_{0.33}MnO_3$*, Appl. Phys. Lett, 83(15), 3135, (2003)

[8] P. W. Anderson and H. Hasegawa, emphConsiderations of double exchange, Phys. Rev, 100(2), 675, (1955)

[9] P.-G. De Gennes, *Effects of double exchange in magnetic crystals*, Phys. Rev, 118(1), 141, (1960)

[10] K. Kubo and N. Ohata, *A quantum theory of double exchange*, J. Phys. Soc. Jpn, 33(1), 21, (1972)

[11] E. O. Wollan and W. C. Koehler, *Neutron diraction study of the magnetic properties of the series of perovskite-type compounds La-Ca-Mn-O* Phys. Rev, 100(2), 545,(1955)

[12] Advanced in condensed matter science Vol II, *Colossal magneto-resistive oxides*, edited by Y. Tokura, Gordon and Breach Science Publishers, (2000); A-M Haghiri-Gosnet and J-P Renard, *CMR manganites: physics, thin films and devices*, J. Phys. D: Appl.Phys, 36, R127, (2003)

[13] E. Dagotto, T. Hotta and A. Moreo, *Colossal magnetoresistance materials: the key role of phase separation*, Phys. Rep, 344, 1, (2001)

[14] P. Schiffer, A.P. Ramirez, W. Bao and S. W. Cheong, *Low Temperature Magnetoresistance and the Magnetic Phase Diagramm of* $La_{1-x}Ca_xMnO_3$, Phys. Rev. Lett 75(18), 3336, (1995)

[15] E. O. Wollan and W. C. Koehler, *Neutron Diffraction Study of the Magnetic Properties of the Series of Perovskite-Type Compounds*, Phys. Rev 100, 545, (1955)

[16] A P Ramirez, *Colossal magnetoresistance*, J. Phys.: Condens. Matter 9, 8171, (1997)

[17] G. A. Prinz, *Magnetoelectronics*, Science 282, 1660 (1998)

[18] K. P. Kamper, W. Schmitt, G. Güntherodt, R. J. Gambin, and R. Ruf, CrO_2a *new half-metallic ferromagnet* Phys. Rev. Lett. 59, 2788(1988)

[19] J. -H. Park, E. Vescovo*, H. -J. Kim, C. Kwon, R. Ramesh, T. Venkatesan, *Direct evidence for a half-metallic ferromagnet*, Nature, 392, 23(1998)

[20] B. Nadgorny, I. I. Mazin, M. Osofsky, R. J. Soulen, Jr., P. Broussard, R. M. Stroud, D. J. Singh, V. G. Harris, A. Arsenov, and Ya. Mukovskii, *Origin of high transport spin polarization in* $La_{0.7}Sr_{0.3}MnO_3$: *Direct evidence for minority spin states*, Phys Rev B, 63, 184433, (2001)

[21] J. M. Daughton, *GMR and SDT sensor applications*, IEEE Trans. Magn., 36, 2773, (2000)

[22] S. S. P. Parkin, X. Jiang, C. Kaiser, A. Panchula, K. Roche, and M. Samant, *Magnetically Engineered Spintronic Sensors and Memory*, Proceedings. IEEE, 91(5), 661, (2003);

[23] A. Moser, K. Takano, D. T. Margulies, M. Albrecht, Y. Sonobe1, Y. Ikeda, S. Sun, E. E. Fullerton, *Magnetic recording: advancing into the future*, J. Phys. D: Appl. Phys, 35, R157, (2002)

[24] C. Chappert, A. Fert and F. N. Van Dau,*The emergence of spin electronics in data storage*, Nature materials, 6, 813, (2007)

[25] D. Jules, *Introduction to Magnetism and Magnetic Materials*Chapman Hall, (1991)

[26] E. W. Lee, *Magnetostriction and Magnetomechanical Effects*, Rep. Prog. Phys, 18, 184, (1955)

[27] E. Tatsumoto and T. Okamoto, *Temperature dependence of the magnetostriction constants in iron*, J. Phys. Soc. Jpn, 14, 1588, (1959)

[28] A. E. Clark, and D. N. Crowder,*High temperature magnetostriction of Tb-Fe and Tb-Dy-Fe*, IEEE Trans. Magn, 21(5), 1945, (1985)

[29] A. E. Clark, J. B. Restorff, M. Wun-Fogle, T. A. Lograsso, and D. L. Schlagel, *Magnetostrictive Properties of Body-Centered Cubic Fe-Ga and Fe-Ga-Al Alloys*, IEEE Trans. Magn, 36(5), 3238, (2000)

[30] R.Kellogg, A.Russell, T.Lograsso, A.Flatau, A.Clark, M.Wun-Fogle, *Tensile properties of magnetostrictive irongallium alloys*, Acta Materialia 52, 5043 (2004)

[31] C. Dasarathy; W. Hume-Rothery, *The System Iron-Gallium*, Proceedings of the Royal Society of London. Series A, Mathematical and Physical Sciences, 286(1405), 141, (1965); O. Kubaschewski, *Iron - Binary Phase Diagrams*, Springer-Verlag, New York, (1982)

[32] E. Clark, Marilyn Wun-Fogle, James B. Restorff, Thomas A. Lograsso, and James R. Cullen, *Effect of Quenching on the Magnetostriction of $Fe_{1-x}Ga_x$ (0.13 < x < 0.21)*, IEEE Trans. Magn, 37(4), (2001)

[33] O. Ikeda, R. Kainuma, I. Ohnuma, K. Fukamichi, K. Ishida, *Phase equilibria and stability of ordered b.c.c. phases in the Fe-rich portion of the FeGa system*, Journal of Alloys and Compounds 347, 198, (2002)

[34] R. Wu, *Origin of large magnetostriction in FeGa alloys*, J. Appl. Phys, 91(10), (2002)

[35] J. Cullen, P. Zhao, and M. Wuttig, *Anisotropy of crystalline ferromagnets with defects*, J. Appl. Phys, 101, 123922 (2007)

[36] S. Pascarelli, M. P. Ruffoni, R. Sato Turtelli, F. Kubel, and R. Grssinger, *Local structure in magnetostrictive melt-spun $Fe_{80}Ga_{20}$ alloys*, Phys. Rev B, 77, 184406, (2008)

[37] A. E. Clark, K. B. Hathaway, M. Wun-Fogle and J. B. Restorff, T. A. Lograsso, V. M. Keppens, G. Petculescu, and R. A. Taylor, *Extraordinary magnetoelasticity and lattice softening in bcc Fe-Ga alloys*, J. Appl. Phys, 93(10), 8621, (2003)

[38] X. Tana and J. S. Baras, *Modeling and control of hysteresis in magnetostrictive actuators*, Automatica 40, 1469, (2004)

[39] S. Ashley, *Magnetostrictive actuators*, presented at The American Society of Mechanical Engineers, (1998)

Chapter 3

Electrospinning

Due to increasing studies of nano materials in the last several years, a variety of materials synthesizing methods have been re-examined and modified. One of the oldest techniques is electrospinning process which is originally developed for synthesing high viscous solution or polymer fibers. The electrospinning has aroused great interest in recent years due to its simplicity, low cost and versatility for fabricating ultrathin and continuous nanofibers or nanowires specially for growth of complicated metallic alloys and oxide and ceramics nanostructures.

3.1 Literature Review

Electrospinning process is a simple technology for the production of continuous wires or fibers with diameters ranging from several microns to as thin as 20 nm or less from a variety of materials including polymers, melt composites and ceramics. The electrospinning process can be considered a variation of the better-known *electrospray* process [1]. Conventional electrospinning and electrospraying setups are displayed in Fig. 3.1, in which under a high electric field, polymer or melt solution jet is ejected

and stretched to form fine continuous wires or small droplets or dots from a capillary. There are basically three components to fulfill the processes: (i) a high voltage supply, (ii) a needle or capillary tube connected with a reservoir filled with a solution and (iii) a grounded metal collector. The behavior of discontinuous or continuous droplets under subject of electric field has been an interesting phenomena. We know that a
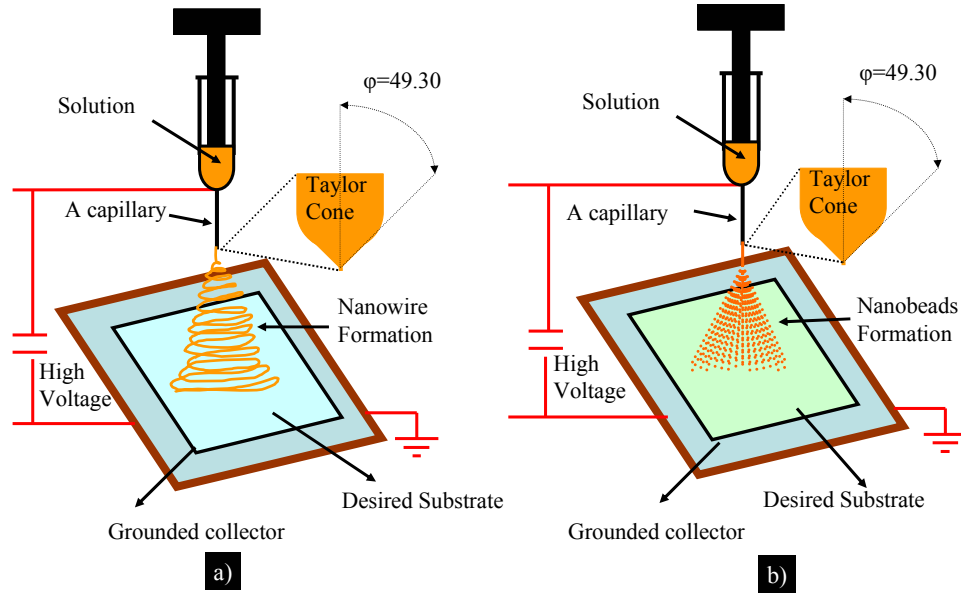
Figure 3.1 A experimental apparatus of a) electrospinning, b) electrospraying processes

droplet tends to have a spherical shape due to its surface tension. In 1882, Lord Rayleigh explained that if a droplet is electrically charged, the spherical droplet would become unstable in shape once the density of surface charges exceeded a threshold known as *Rayleigh limit*, where Coulomb repulsion force equals to the surface tension as following:

$$q^2 = 8\pi^2 \varepsilon \sigma r^3 \tag{3.1}$$

q - electric charge, ε - electrical permittivity of the surrounding, σ -surface tension of the liquid, r -radius of the droplet. Beyond the Rayleigh limit, the surface tension

could be overcome by the electrostatic repulsion. In 1902, J. F. Cooley [2] and W. J. Morton [3] independently filed a US patent claiming in which "...certain new, useful improvements in method of electrically dispersing fluids by subjecting the fluids in a free and attenuated formation to the disruptive and dispersive action of a gaseous field of convective action of electricity at high tension". In his 1914 work, John Zeleny [4] reported behavior of fluid droplets at the end of glass capillaries under a high voltage, a process that what we call it today as *electrospray* process Fig. 3.2. His report
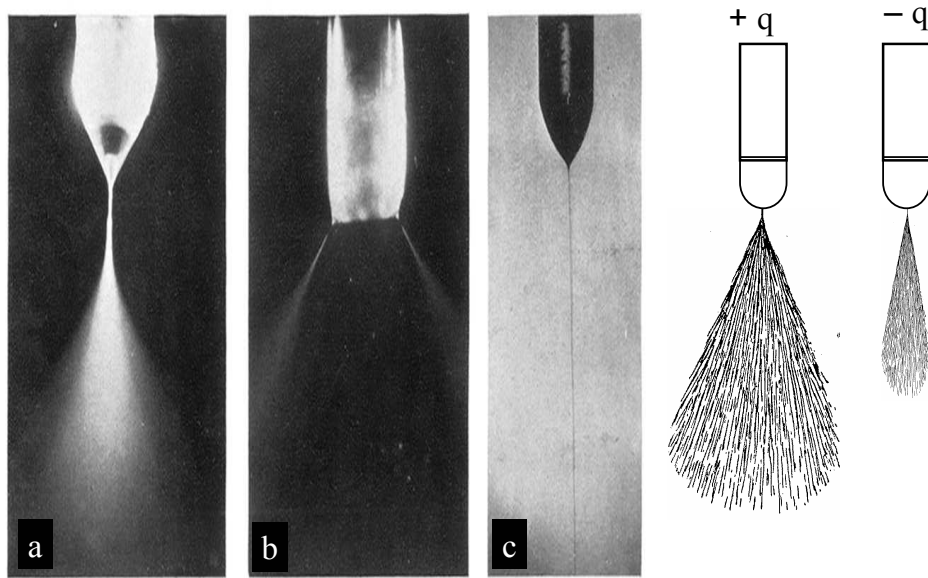
Figure 3.2 A real time photography of instability of electrified liquid surfaces. [Reprinted from ref. 4]

presents experimental evidence for several electrospray operating regimes (dripping, burst, pulsating, and cone-jet). A few years later, he captured the real time-lapse images of the dynamic ethyl alcohol jets at end of glass capillaries created by positive or negative charges [5]. The liquid was charged to several thousand volts from a static machine, and a grounded plate was placed 2-4 cm below the end of the glass tube. He also attempted to mathematically model the behavior of fluids under uniform

electrostatic forces and pointed out the discharging electrospray process was different in applied negative and positive charges. During the years between 1934-1944 [6–9], further developments were made by Anton Formhals who invented several efficient apparatus for production of artificial continuous fibers and textiles using different high voltages and using new solutions and first time used the name of *electrospinning* in his patents. Similar to the standard electrospray process, the application of high voltage to a solution can result in the formation of a cone-jet geometry. If the jet turns into very fine fibers instead of breaking into small droplets, the process is known as electrospinning. He also employed different spinning solutions, for example, rubber and caoutchouc solutions. Electrospinning from a melt rather than a solution was patented by C.L Norton in 1936 using an air-blast to assist fibers formation. In 1943, F. W. Manning [10] patented his idea for manufacturing unwoven fabrics by electrospinning method that may be used for: sanitary napkins, surgical dressing, wearing apparel, filtering, leather substitutes, and blankets. During 1964-1969, G. I. Taylor published several papers about the theoretical groundwork of electrospry and electrospinning [11–13]. Taylor's work contributed to a mathematical model of electrically driven jets which originate above a threshold voltage. He considered the shape of the droplet at the end of a capillary filled by viscous fluid and under the effect of an electric field and estimated critical potential difference at which *Taylor cone* develops with half angle of ϕ=49.3^0 He formulated following relation between a critical voltage and surface tension of a spinning liquid.

$$V_c^2 = \frac{4H^2}{L^2}(ln\frac{2L}{R} - \frac{3}{2})(1.30\,\pi\,r\,T)(0.09) \tag{3.2}$$

V_c - critical voltage, H - distance between the tip of the capillary and the substrate, L - length of capillary with radius r, T -the surface tension of the liquid. The conductivity and viscosity factors are missing in this equation, but the relationship between surface

tension and applied voltage serves as a useful guide for slightly conducting, medium-to-low viscosity solutions. In his 1968 patent, H. L. Simons [14] described that his invention possible for the first time for the electronspun fibers to be gathered in to a thin, lightweight non-woven fabric with a pattern simulating and desired woven fabric. In 1971, Baumgarten [15] conducted systematic experiments to employ the process to acrylic polymer solutions dissolved in dimethyl formamide to fabricate fine fibers with diameters ranges 0.05 to 1.1. In 1981, Manley and Larrondo reported that polyethylene and polypropylene can be electrospun from melt [16]. In 1986, I. Hayati and *et al.*, made direct observation of jet formation of semiconducting liquid and they demonstrated the role of electrical shear effects in electrospinning process [17]. In the early 1990's several research groups, notably Reneker's group who re-popularized the name of electrospinning for the process demonstrated that many organic polymers could be electrospun into continuous *nanofibers or nanowires* [18]. Since then, the number of publications about electrospinning has been increasing exponentially every year. Starting mid 1990's there have been further theoretical developments of the driving mechanisms of the electrospinning process. A mathematical and simulation model developed by A. L Yarin and D. H. Reneker showed the curved path is a consequence of an electrically driven bending instability of the charged wires and the model reproduced the path of the wires, its motion, the large elongation was observed [20, 21]. Reznik *et al.*, described extensive work on the shape of the Taylor cone and the subsequent ejection of a fluid jet [22]. The work by Hohman *et al.*, in 2001 investigates the relative growth rates of the numerous proposed instabilities in an electrically forced jet once in flight and identified them as the classical (axisymmetric), Rayleigh instability, and electric field induced axisymmetric and whipping instabilities [23]. Also an important work has been reported by Brenner and Srinivas Paruchuri in 2003 endeavoring to describe the most important instability to the electrospinning

process, the bending (whipping) instability [24]. In 2002, Dai Li *et al.*, reported successful synthezing of ceramic, hollow and as well as aligned composites nanowires [25]. H. Hou and D. H. Reneker demonstrated that carbon nanotubes could grow on electrospun carbon fibers to form nanotubes-on-nanofiber structures by incorporating iron catalysts in the fibers. In 2002, J. B. Fenn was awarded Nobel prize in Chemistry by his work in development of electrospray ionization, uncle of electrospinning process, for the analysis of biological macromolecules.

In 2003, Sergey V. Fridrikh *et al.*, presented a simple analytical model for the forces that determine jet diameter during electrospinning as a function of surface tension, flow rate, and electric current in the jet.

$$h_t = [\gamma \varepsilon \frac{O^2}{I^2} \frac{2}{\pi(2ln\lambda - 3)}]^{1/3} \tag{3.3}$$

Where, h_t - the final jet diameter, γ - the surface tension of the solution, ε- the dielectric permittivity, Q - the flow rate, I - electric current, λ - the displacement of the centerline of the jet. The model predicts the existence of a terminal jet diameter, beyond which further thinning of the jet due to growth of the whipping instability does not occur. Experimental data for polyethylene oxide (PEO) and polyacrylonitrile (PAN) fibers attest to the accuracy of the model. The ability to fabricate highly aligned sub-micron and nanowires by electrospinning process has many implications in the future technology. Several researchers have shown that it is possible to obtain aligned wires by using a rotating collector (Matthews *et al.*, 2002, Xia and *et al.*, 2004, Subramanian and *et al.*,2005), parallel electrodes (Li *et al.*, 2003), rotating tube collector with knife-edge electrodes below (Teo and *et al.*, 2005), ring collector placed in parallel (Dalton *et al.*, 2005), yarn collection using water bath (Smith and *et al.*, 2005, Khil and *et al.*, 2005), controlled deposition using a ring (Stankus *et al.*, 2004, Buttafoco *et al.*, 2006, Kim 2006, Kim *et al.*, 2006) and magnetic electrospinning

(Dayong Yang *et al.*, 2007).

3.2   Electrospinning Process and Mechanism

The electrospinning process is mostly characterized by three major regions: i) the cone region, ii) the steady jet region, and iii) the instability region.

3.2.1   The cone region

The surface tension or visco elastic forces of the solution cause drops at the tip of the needle or capillary connected to a reservoir containing polymer or melt to retain their hemi-spherical shape. The high electric voltage is introduced between tip of the needle and ground causes the droplet to deform into a conical shape referred to as a Taylor cone at the tip of the needle. When the applied voltage further increased beyond a theshhold value, a liquid jet is ejected and stretched from tip of the needle to form jet or wires. Initially, as formed wires has relatively larger diameter, and it becomes thinner as the electrical forces elongate the wires as Fig. 3.3 a)-c) in which the electrical potential was applied for a little more than 28 milliseconds earlier. The droplet of polyethylene oxide solution in frame 28 milliseconds was already transformed part of the way toward the Taylor conical shape by the applied electric potential. The rounded tip became sharper and a jet emanated from the tip of the cone. Six milliseconds later, the shape of the cone was changed and after about 20 milliseconds the droplet had a rounded shape. A rapidly elongating and thinning jet, carrying electrical charge, flowed from the droplet.
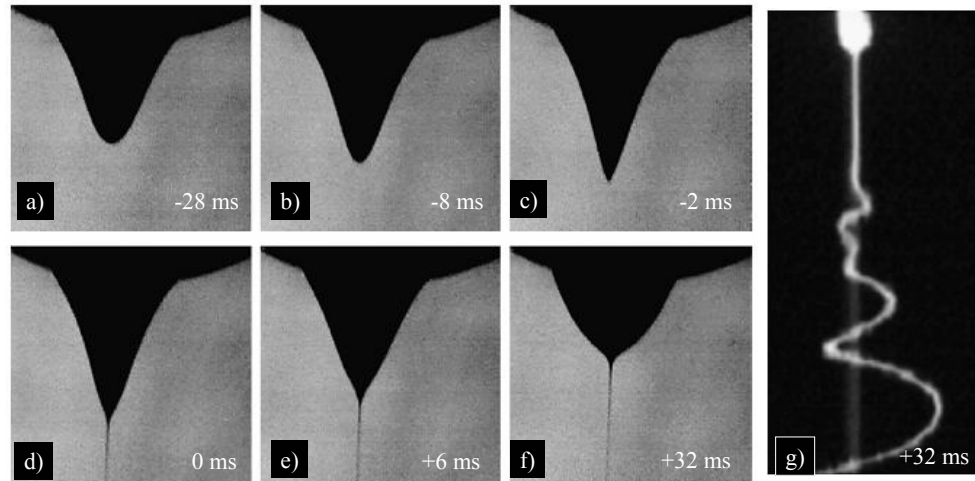
Figure 3.3 The evolution of the shape of a fluid drop in selected images from a video in which a new image was recorded every 2 ms. Figures are taken from H. Fong, D. H. Reneker, *Electrospinning and the formation of nanofibers*, Structure formation in polymeric fibers, Munich, Cincinnati, Ohio, Hanser Publishing, p. 225-46, (2000); A .L. Yarin, W. Kataphinan, D. H. Reneker, *Branching in Electrospinning nanofibers*, J. App. Phys, 98, 064501 (2005)

3.2.2 The steady region

Once the jet has initiated, the fluid can travels along a straight path for a certain distance. This shape is stable, and persisted as long as the solution carried away by the jet was replaced by fluid flowing into the droplet through the hole in the needle to which the droplet was attached by surface tension Fig. 3.3 d)-f). The hydrostatic pressure in the fluid is usually created by the height of the solution in the reservoir. The shape and size of the steady state droplet may change if either the hydrostatic pressure or the applied electrical potential changes.

3.2.3   The instability region

The wires travels in straight line for some time and distance in direction of the applied field, and beyond that distance, the path is curved and become more complicated and instable also referred to as whipping Fig. 3.3 g). Different ideas of regarding the nature of the instability have been given (Baumgarten, 1971, G. Taylor, 1969, D. H. Reneker, 2000, A. L. Yarin *et al.*, 2001). The bending may allow for a large elongation to occur in small region of space. This continuous elongation may be strongly influenced by the repulsion between charges on the fluid. Y. M. Shin *et al.*, (2001) state that the rapid growth of the non-axisymmetric instability causes bending and stretching of the jet. Three modes of the instability were described. (i) Classical Rayleigh mode (axisymmetric), (ii) electric field induced axisymmetric conducting mode, (iii) the whipping non-axisymmetric. Depending upon the electrospinning conditions, the resulting bending instability can be caused by one or a combination of these modes. Due to nature of electrospinning process, optimization of the electrospun wire diameter and morphology can be obtained by (i) adjusting polymer concentration or solvent composition, (ii) applied high voltage, (iii) distance between a capillary tube and grounded collector, and (iv) environmental conditions. For example, one of the problems encountered in electrospinning is defects that form beads. H. Fong *et al.*, (1999) have been shown that higher viscosity concentration resulted in fewer beads (Fig. 3.4).
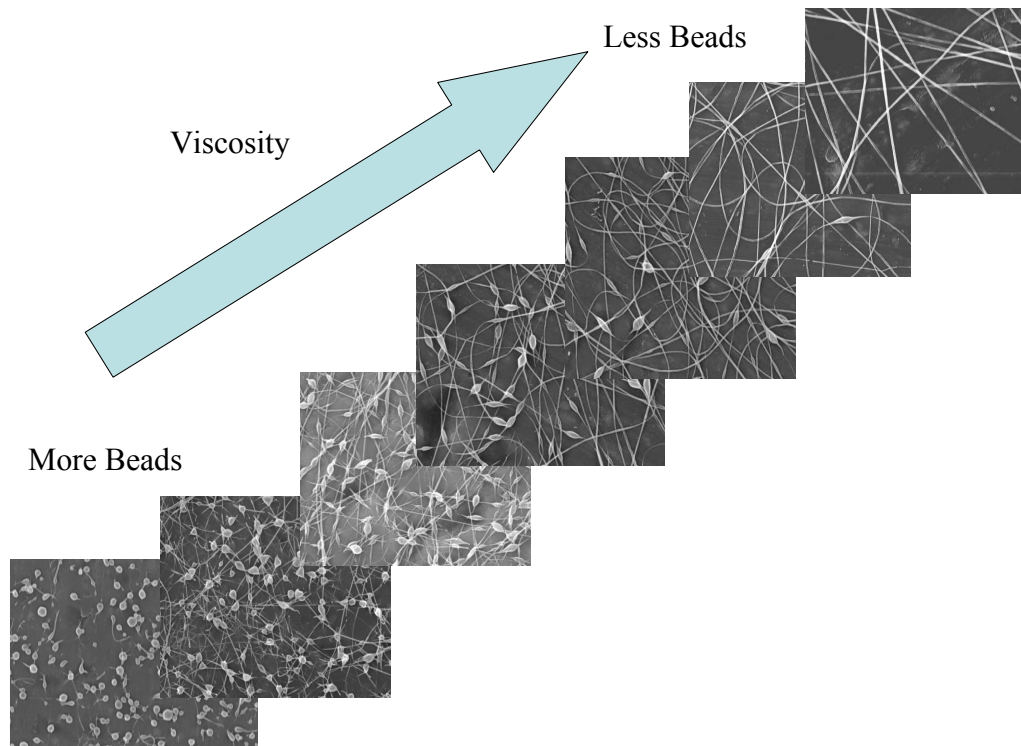
Figure 3.4 SEM photographs of electrospun nanofibers from different polymer concentration solutions, H. Fong, I. Chun, D. H. Reneker, *Beaded nanofibers formed during electrospinning*, Polymer 40, p. 45854592, (1999)

The high viscosity fluid state may achieved by dissolving polymers in a suitable solvent or processing them at a temperature close to the melting point. Deitzel *et al.*, (2001) investigated the influence of electrical charge, which was applied for electrospinning, on the morphology of PEO nanofibers. They reported that with the increase of the electrical potential the resulting nanofibers became rougher and concluded it influence the macroscale morphology of electrospun textiles. The distance d, between a capillary and collector is also important factor because the electric field strength is determined by dividing applied voltage V by the distance, d as a results electric field strength and flight time of the jet are directly affected.

3.3 Applications of Electrospinning

3.3.1 Functional Fibers

Synthesis of high quality hierarchical nanostructures with controllable sizes, shapes, and compositions has received increasing attention in recent years. Such complex architectures, especially those based on one-dimensional nanostructures, are expected to display novel functions important to the development of advanced devices and systems such as active components for ultrahigh-density data storage, as well as in the fabrication of sensors and spintronic devices (T. Thurn-Albrecht, J. Schotterand *et al.*, 2000, D. A. Allwood, G. Xiong *et al.*, 2002, A. Fert and L. Piraux, 1999). Notable works for highly aligned electropsun wires are Li *et al.*, (2003) used parallel electrodes to obtain well aligned electrospun wires; Bibekananda Sundaray *et al.*, (2004) fabricated highly ordered electrospun polymer micro and nanowires by a rotating cylinder using a step-motor [26]; Dalton *et al.*, 2005 used ring collector placed in parallel; D. Yang *et al.*, 2007 used strong magnetic field for aligned magnetic electrospun wires [27] ; Javed Rafique *et al.*,(2007) aligned long polymer nanofibers on large scale by using a tip collector [28].
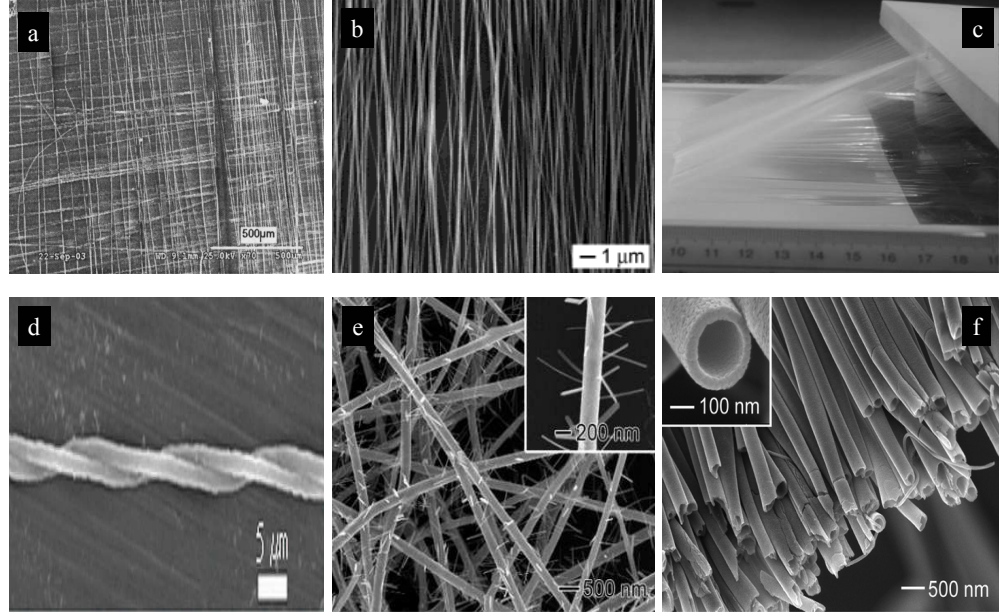
Figure 3.5 a) Net electrospun wires by rotating cylinder using a step-motor, b) Aligned electrospun wires by a magnetic field, c) Well aligned polymer jets using a tip collector, d) Twistted electrospun wires, e) High quality V_2O_5-TiO_2 hierarchical nanostructures, f) Electrospun hollow fibers, Reproduced from [25-30]

In addition, B. K. Gu *et al.*, fabricated artificial twisted nanofibers that resemble naturally twisted fiber structures, such as collagen fibril and double-strand DNA, using a modified conventional electrospinning system to directly develop the twisted nanofibers [29]. R. Ostermann *et al.*, demonstrated that single-crystal V_2O_5 nanorods could be grown on rutile nanofibers by carefully calcining composite nanofibers consisting of amorphous V_2O_5, amorphous TiO_2, and poly(vinylpyrrolidone) [30]. Dan Li *et al.*, fabricated ceramic hollow nanofibers by electrospinning technique [31]. Due to the well-known fact that the rate of electrochemical reactions is proportional to the surface area of the electrode, conductive nanofibrous membranes are also quite suitable for using as porous electrode in developing high performance battery (I. D. Norris, M. M. Shaker *et al.*, 2000). It has been reported that to use electrospun

nanofibers in the development of a liquid crystal device of optical shutter which is switchable under an electric field between a state in which it is substantially transparent to incident light and a state in which it is substantially opaque (C. M. Waters CM, T. J. Noakes *et al.*, 1994). The main part of this liquid crystal device consisted of a layer of nanofibers permeated with a liquidcrystal material, having a thickness of only few tens microns.

3.3.2 Tissue Engineering

Recently, electrospinning provides a mechanism to produce nanofibrous scaffolds from a variety of polymer materials, including synthetic polymers have drawn increased interest for tissue engineering. Tissue scaffolds are utilized to repair the damaged human tissues. Electrospun polymetric nanofiber mat has similar structure with the nano-scaled nonwoven fibrous extra cellular matrix (ECM) proteins. Thus is a good candidate for artificial ECM - mimic tissue engineering scaffold (Flemming *et al.*, (1999), Ma *et al.*, (2005), Huang *et al.*, (2007)). Also electrospun polymetric nanofiber mat has a high surface area and porosity and contains empty space between the fibers that is about the size of cells. In addition, it may provide (1) cellbinding capabilities to allow cells to adhere and proliferate, (2) adequate viscoelasticity and strength to support the developing tissue. To date, electrospinning has been applied for the fabrication of nanofibrous scaffolds from numerous biodegradable polymers, such as poly(-caprolactone) (PCL), poly(lactic acid) (PLA), poly(glycolic acid) (PGA), and the copolymer poly(lactide-co-glycolide) (PLGA) (W. J. Li, C. T. Laurencin *et al.*, 2002, K. Kim, M. Yu *et al.*, 2003, S. R. Bhattarai, N. Bhattarai *et al.*, 2004). These biodegradable polymers have been used to electrospin engineered scaffolds for bone tissue (W. J. Li, Danielson *et al.*, 2003, H. Yoshimoto, Y. M. Shin and et al., 2003) and cardiac grafts (M. Shin, O. Ishii *et al.*, 2004). Polymer nanofibers can also be

used for the treatment of wounds or burns of a human skin, as well as designed for haemostatic devices with some unique characteristics. With the aid of electric field, fine fibers of biodegradable polymers can be directly sprayed/spun onto the injured location of skin to form a fibrous mat dressing. For example, Polyurethane (PU) nanofibrous membranes have been used as wound dressings (M. S. Khil, D. I. Cha *et al.*, 2003).

Bibliography

[1] J. B. Fenn, M. Mann, C. K. Meng, S. F. Wong, C. M. Whitehouse, *Electrospray ionization for mass spectrometry of large biomolecules*, Science 246, 64, (1989).

[2] J. F. Cooley, *Apparatus for electrically dispersing fluids*, US Patent 692631, (1902)

[3] W. J. Morton, *Method of dispersing fluids*, US Patent 705691, (1902)

[4] J. Zeleny, *The electrical discharge from liquid points, anda hydostatic method of measuring the electric intensity at their surfaces*, Phys. Rev, 3, N2, (1914)

[5] J. Zeleny, *Instability of electrified liquid surfaces*, Phys. Rev, 10, N1, (1917)

[6] A. Formhals, *Method and apparatus for the production of fibers*, US Patent 2116942, (1938)

[7] A. Formhals, *Method and apparatus for the production of fibers*, US Patent 2123992, (1938)

[8] A. Formhals, *Method and apparatus for the production of artificial fibers*, US Patent 2158416, (1939)

[9] A. Formhals, *Method and apparatus for spinning*, US Patent 2349950, (1944)

[10] W. F. Manning, *Method and apparatus for making unwoven and composite fabrics*, US Patent 2336745, (1943)

[11] G. Taylor, *Disintegration of Water Drops in an Electric Field*, Proc. Royal Soc. London A: Mathematical, Physical Engineering Sciences, 280, 383, (1964)

[12] G. Taylor, *The force exerted by an electric field on a long cylindrical conductor*, Proc. Royal Soc. London A: Mathematical, Physical Engineering Sciences, 291, 145, (1965)

[13] G. Taylor, *Electrically Driven Jets*, Proc. Royal Soc. London A: Mathematical, Physical Engineering Sciences, 313, 453, (1969)

[14] H. L. Simon, *Process and apparatus for producing patterned non-woven fabrics*, US 3280229, (1966)

[15] P. Baumgarten, *Electrostatic spinning of acrylic microfibers*, J. Colloid and Interface Science, 36, 71, (1971)

[16] L. Larrondo, R. St. John Manley, *Electrostatic fiber spinning from polymer melts, experimental observations on fiber formation and properties*, J. Polymer. Science, 19(6), 909, (1981)

[17] I. Hayati, A. I. Bailey, Th. F. Tadros, *Mechanism of stable jet formation in electrohydrodynamic atomization*, Nature 319, 41 (1986)

[18] D. H. Reneker, I. Chun, *Nanometre diameter fibres of polymer, produced by electrospinning*, Nanotechnology, 7, 216, (1996)

[19] I. Chun, D. H. Reneker, H. Fong, X. Fang, J. Deitzel, N. B. Tan, K. Kearns, *Carbon nanofibers from polyacrylonitrile and mesophase pitch*, J. Adv. Mater, 31(1), 36, (1999)

[20] A. L. Yarin, S. Koombhongse, D. H. Reneker, *Bending instability in electrospinning of nanofibers*, J. Appl. Phys, 89(5):3018, (2001)

[21] A. L. Yarin, S. Koombhongse, D. H. Reneker, *Taylor cone and jetting from liquid droplets in electrospinning of nanofibers.* J. Appl. Phys, 89(9):4836, (2001)

[22] S. N. Reznik, A. L. Yarin, E. Zussman, and L. Bercovici, *Evolution of a compound droplet attached to a core-shell nozzle under the action of a strong electric field*, Phys. Fluids, 18, 062101, (2000)

[23] M. M. Hohman, M. Shin, G. Rutledge and M. Brenner, *Electrospinning and electrically forced jets. I. stability theory*, Phys. Fluids 13, 2201, (2001)

[24] M. P. Brenner and S. Paruchuri, *Thermal bending of liquid sheets and jets*, Phys. Fluids, 15, 3568 (2003)

[25] D. Li, Y. Wang, and Y. Xia, *Electrospinning of Polymeric and Ceramic Nanofibers as Uniaxially Aligned Arrays*, Nano. Lett, 3(8), 1167, (2002); D. Li, Y. Wang, and Y. Xia, *Fabrication of Titania Nanofibers by Electrospinning*, Nano. Lett, 3(4), 555, (2002); D. Li and Y. Xia, *Direct Fabrication of Composite and Ceramic Hollow Nanofibers by Electrospinning*, Nano.Lett, 4 (5), 933, (2004)

[26] B. Sundaray, V. Subramanian, T. S. Natarajan, R. Z. Xiang, C. C. Chang, and W. S. Fann, *Electrospinning of continuous aligned polymer fibers*, Appl. Phys. Lett, 84(7), 1222, (2004)

[27] D. Yang, B. Lu, Y. Zhao, and X. Jiang, *Fabrication of Aligned Fibrous Arrays by Magnetic Electrospinning*, Adv. Mater, 19, 3702, (2007)

[28] J. Rafique, J. Yu, J. Yu, G. Fang, K. W. Wong, Z. Zheng, H. C. Ong, and W. M. Lau, *Electrospinning highly aligned long polymer nanofibers on large scale by using a tip collector*, Appl. Phys. Lett, 91, 063126, (2007)

[29] B. K. Gu, M. K. Shin, K. W. Sohn, S. I. Kim,S. J. Kim, S. K. Kim, H. Lee, and J. S. Park, *Direct fabrication of twisted nanofibers by electrospinning*, Appl. Phys. Lett, 90, 263902, (2007)

[30] R. Ostermann, D. Li, Y. Yin, J. T. McCann, and Y. Xia, *V2O5 Nanorods on TiO2 Nanofibers: A New Class of Hierarchical Nanostructures Enabled by Electrospinning and Calcination*, Nano. Lett, 6 (6), 1297, (2006)

[31] D. Li and Y. Xia, *Direct Fabrication of Composite and Ceramic Hollow Nanofibers by Electrospinning*, Nano. Lett, 4 (5), 933, (2004)

Chapter 4

Experimental Techniques

This chapter contains descriptions of the main techniques used to characterize the electrospun ferromagnetic nanowires in this thesis work. Scanning Electron Microscope, X-ray powder diffraction, Laser Raman spectroscopy were the three main techniques used for structural analysis and morphology. The devices were fabricated from the nanowires using electron-beam lithography and were characterized using Agilent 4156C Precision Semiconductor Parameter Analyzer.

4.1   Scanning Electron Microscopy

The scanning electron microscope (SEM) uses a focused beam of high-energy electrons to generate a variety of signals at the surface of solid specimens. The signals that derive from electron-sample interactions reveal information about the sample including topographic, morphology, chemical composition, and crystalline structure [1, 2]. Areas ranging from approximately 1 cm to 5μm in width can be imaged in the scanning mode. A schematic diagram of a typical SEM is shown in Fig. 4.1 a. Electrons are thermionically emitted from the tungsten-point-cathode electron gun and are acceler-

ated to the anode with an energy typically ranging from a few hundred eV to 40 keV.
Tungsten has the highest melting point and lowest vapor pressure of all metals and
therefore can be heated enough for electron emission. The electron beam is focused
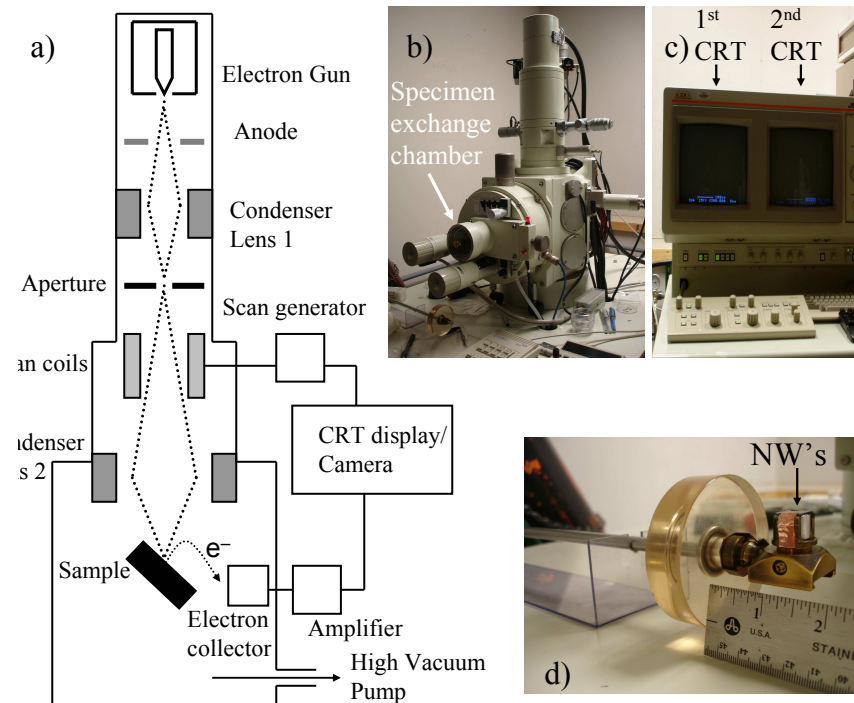
Figure 4.1 Scanning Electron Microscope

by one or two condenser lenses to a spot about 0.4 nm to 5 nm in diameter. The beam
passes through pairs of scanning coils in the electron column, typically in the final
lens, which deflect the beam in the x and y axes so that it scans in a raster fashion
over a rectangular area of the sample surface. The energy exchange between the elec-
tron beam and the sample results in the reflection of high-energy electrons by elastic
scattering, emission of secondary electrons by *inelastic scattering* and *the emission
of electromagnetic radiation*, each of which can be detected by specialized electron
collector detectors. The beam current absorbed by the specimen can also be detected
and used to create images of the distribution of specimen current. Electronic ampli-
fiers of various types are used to amplify the signals. Magnification in a SEM can be

controlled over a range of up to 6 orders of magnitude from about 25x to 250,000x. Unlike optical microscopes, image magnification in the SEM is not a function of the power of the objective lens. SEMs may have condenser and objective lenses, but their function is to focus the beam to a spot, and not to image the specimen. Provided the electron gun can generate a beam with sufficiently small diameter, an SEM could in principle work entirely without condenser or objective lenses, although it might not be very versatile or achieve very high resolution. The raster scanning of the CRT display is synchronized with that of the beam on the specimen in the microscope, and the resulting image is therefore a distribution map of the intensity of the signal being emitted from the scanned area of the specimen. The image is digitally captured and displayed on a computer monitor and saved to a computer's hard disc. At Vitreous State Laboratory, we do use state-of-art high resolution JSM-6300 with a modern digital image processing system (Fig. 4.1 b). It operates at accelerating voltages of between 0.2 and 30 kV in secondary and backscattered modes. Fig. 4.1 c shows control and display system. In order to place samples in the SEM, specimen exchange is made through the specimen exchange chamber. The requisite to observe the samples by SEM is that they have to be electrically conductive. Metallic samples as, e.g., our wires grown on Si/SiO_2 can be placed directly into the SEM (Fig. 4.1 d) for imaging.

4.2   X-ray Diffractometer

X-ray diffractometry (XRD) is used to identify specific crystalline compounds, both mineral and organic, based on their crystal structure. X-rays are electromagnetic radiation of wavelength about 1 angstrom, which is about the same size as an atom. They occur in that portion of the electromagnetic spectrum between gamma-rays and the ultraviolet. X-rays impinging on a crystal scattered by the lattice planes forming

areas of constructive and destructive interference. The condition for constructive interference is given by the Bragg equation:

$$2 \cdot d \cdot sin\left(\vartheta\right) = n \cdot \lambda \tag{4.1}$$

where, n is an integer order of diffraction, λ is the X-ray beam wavelength being diffracted and d is the crystal lattice spacing. The process of taking X-ray diffraction measurements involves scanning through a range of incident angles on the sample. Fig. 4.2 a shows a typical configuration of a diffraction system. X-ray diffractometers
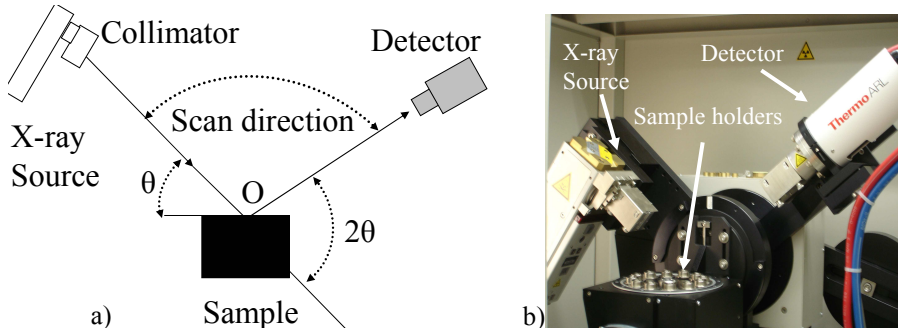

Figure 4.2 The mechanism in an x-ray diffractometer

consist of three basic elements: i) an X-ray source, ii) a sample holder, and iii) an X-ray detector. X-rays are generated in a cathode ray tube by heating a filament to produce electrons pass through a collimator and become more aligned in a specific direction [1,3]. Once x-rays hit on sample crystal, they are either transmitted through the crystal, reflected off the surface, or diffracted by the crystal lattice. A beam stop is located directly opposite the collimator to block transmitted rays and prevent burn-out of the detector. Reflected rays are not picked up by the detector due to the angles involved. Diffracted rays which satisfied the Bragg law at the correct orientation for the configuration are then collected by the detector. Detector generally measures intensity of the diffracted x-rays; it can be rotated about O and set any desired angular position. Modern single-crystal diffractometers use CCD (charge-coupled

device) technology to transform the X-ray photons into an electrical signal which are then sent to a computer for processing. At Vitreous State Laboratory, we do use Thermo ARL X-ray diffractometer with CuKa radiation, where λ=1.541 angstrom Fig. 4.2 b).

4.3 SQUID Magnetometer

Superconducting Quantum Interference Devices (SQUID) magnetometers are used to study magnetic properties of the electrospun nanowires at low and ambient temperatures with collaboration through Prof. Wagner's group at The George Washington University, Washington DC and Prof. Heiman's group at Northeastern University, Boston, MA. SQUID is highly sensitive magnetometer that is able to measure ex-
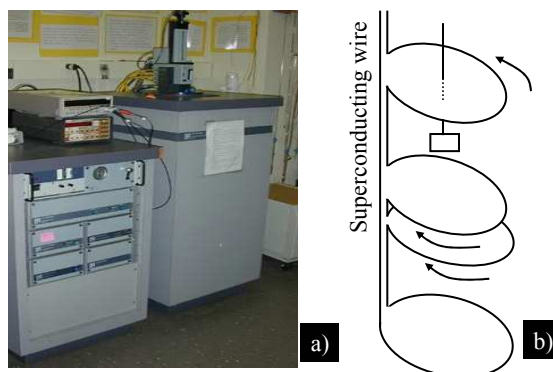
Figure 4.3 a) Quantum Design MPMS SQUID Magnetometer, b) Second-order gradiometer superconducting pick-up coils.

tremely small magnetic fields based on inductive coils or loops Fig. 4.3 a. During measurement process, desired samples moves through several superconductiing detection coils connected to SQUID with superconducting wires, magnetic moment of the samples induces an electric current in the detection coils (Fig. 4.3 b). Any change of magnetic flux in detection coils which is proportional to the magnetic moment of the sample produces a change in persistance current in the detection circuit. The

SQUID is inductively coupled with the detection coils, so the SQUID electronics produces output voltage which is strictly proportional to the flowing current [4].

4.4   Micro-Raman System

The Raman effect is an inelastic scattering phenomenon. A Raman experiment typically uses laser light to excite a sample of interest, where a detector records scattered light intensities from the sample. The scattered light consists of the elastically scattered Rayleigh component and the much weaker Raman component. The Raman component is shifted to lower frequencies (Stokes) and higher frequencies (anti-Stokes) with respect to the incident laser light and Rayleigh scattered light. In a Raman experiment, the Rayleigh scattered light intensity is filtered or suppressed before reaching the detector. The Raman spectral features are produced by vibrational modes of atoms within a sample of interest that add frequency components to, or subtract frequency components from, the incident laser light frequency. A Raman spectrum provides vibrational information about the sample that is directly influenced by the arrangements of atoms and atomic bonding within that sample. Therefore, Raman spectroscopy is useful for determining atomic structural and chemical aspects of a sample. The frequency units for a Raman spectrum are in wavenumbers (cm^{-1}), or waves per cm. Vertically polarized laser light propagates from the laser through a grating filter that eliminates weak laser plasma components that are at different frequencies with respect to the desired laser line. The filtered laser light is sent through a broad band polarizer rotator to polarize the light vertically or horizontally with respect to the propagation direction. The laser light is then guided to the microscope by beam steering optics where it is passes through an aperture, lens, and beam splitter assembly so that it propagates down through the microscope objective to a sample on

the microscope stage (Fig. 4.4). The laser beam is focused on the sample to a spot size of 10 μm or less in diameter (depending on the microscope objective used). Scattered light from the sample propagates back up through the microscope objective, through the beam splitter, and is sent through an analyzing polarizer in the column of the microscope. The polarized scattered light is then guided through the notch filters,
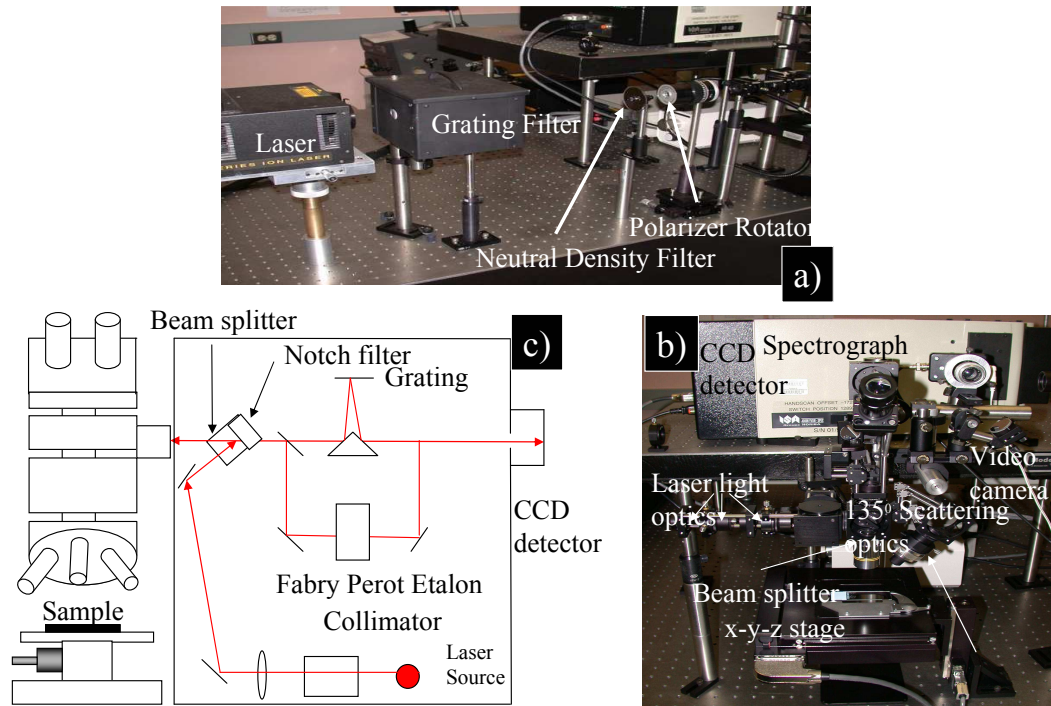

Figure 4.4 a) Front end of Raman system at VSL (handles incident laser light characteristics), b) Laser Microscope in back-scattering mode, c) Schematic diagram of a Raman spectrometer

which reduce the intensity of the Rayleigh scattered light by 10 optical densities [5]. The scattered light is now dominated by the Raman component from the sample and is guided into the spectrograph by mirrors and a collection lens at the entrance slit of the spectrograph. The scattered light polarization is intentionally oriented perpendicular with respect to the rulings of the grating in the spectrograph. The grating is set by the spectrograph so that it spatially disperses the scattered light on to the CCD array detector. The geometry of the spectrograph-detector system is designed so

that there is a nearly linear relationship between the horizontal position of the pixels in the CCD array and the scattered light frequency. At VSL, major Raman system components consist of an Argon (Ar+) laser (Melles-Griot Laser: Model 35-LAP-431-208), a broadband polarizer rotator (Newport: Model PR-550), a microscope with a computer controlled x-y-z stage (Applied Scientific Instruments MS-2000), two notch filters (Kaiser Optical Holographic Super Notch and Super Notch-Plus filters: 4 and 6 optical densities, respectively, at the laser line), a single grating spectrograph (JY-Horiba: Model HR460), and a peltier cooled 2048 x 512 element CCD array detector (Andor Technology: Model DU440BV).

4.5 Nanoscale Device Fabrication

The nanoscale devices require conductive electrical contacts to the nanowires in order to test their electrical and magneto-transport properties. The patterns of nanoscale devices are created on wafers by lithography. The lithography process creates the patterns of integrated circuits in films of specialized materials called *resist*, which are coated on the wafers on which devices are made. Resists typically do not adhere properly to untreated surfaces of silicon and silicon-containing materials such as dioxide and silicon nitrite. To ensure proper adhesion, the wafer surfaces treated prior to resist coating. Resists are typically compromised of organic polymers applied from a solution and are broadly classified as positive or negative. Unexposed positive resists normally have very long solubility in developer and become soluble by exposure to energetic electron-beam. Negative resist behave in the opposite manner; unexposed negative resists soluble in developer, and lose their solubility upon exposure to electron-beam [6]. Negative resists were used predominately prior to the advent of wafer steppers. Fabrication of single nanowire devices require time consuming several

steps of process starting with i) sonication of the as-grown nanowires on a substrate in small amount of isopropanol, ii) drop the sonicated wires in isopropanol onto the p-type Si substrates coated with SiO_2 with copper alignment markers (Fig. 4.5a), iii) bi-layer resist coating (Fig. 4.5b), iv) design of the electrodes, v) e-beam exposure (Fig. 4.5c), vi) developing (Fig. 4.5d), vii) metal deposition (Fig. 4.5e), viii) lift-off (Fig. 4.5f),) ix) examining the device under microscope and x) wire bonding the device to the socket. For sonication of the as grown nanowires, several small pieces
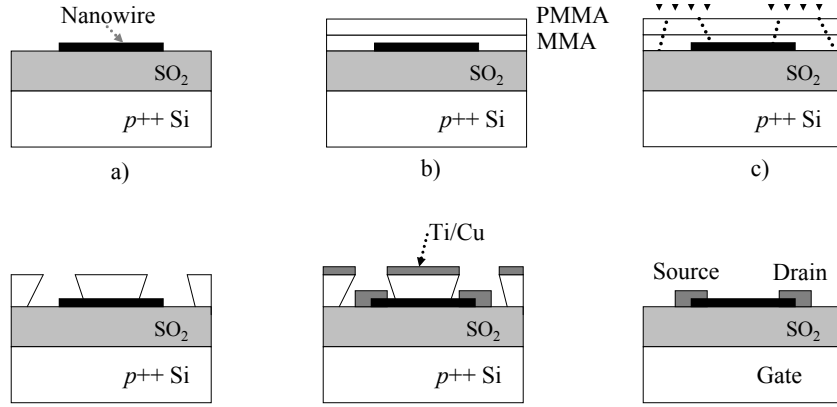

Figure 4.5 The procedure for nanoscale device fabrication

of as grown nanowires on Si substrates were placed inside a small glass container filled with significantly small amount of isopropanol and sonicate it for 5 sec-3 min depend on nanowire materials. For resist coating, polymethyl methacrylate (PMMA) and MMA (methyl methacryllate) are common positive e-beam resists consisting of long polymer chain of carbon atoms. In bilayer resist, high molecule weight PMMA forms top layer and low molecular weight MMA forms the bottom layer. MMA (6% in Ethyl Lactate/ 950K), PMMA resist bilayers with MMA/PMMA thicknesses of 450 nm and 90 nm respectively applied to the wafer by a spin coating. As a bottom layer, the MMA liquid is droped at the center of the wafer. Then wafer is spun about its axis at high speed. The resist is subjected to centrifugal forces, spreading the resist, and leaving a thin, uniform layer adhering to the all over the surface. Depend

on the nanowires size, average thickness can be controlled by adjusting either rate of spin or resist viscosity. Average device thicknesses in our experiment are 150 nm, the spinning rate was 3000 revolution per minute (RPMs). It should be noted that spinning either too fast or too slow produces non uniform coatings. Following spinning, the wafer is removed and placed onto a hot plate for hardening MMA coating. After that coating of top PMMA resist is applied, the procedure is same as MMA resist coating. Following the coating, the resist film on the wafer usually does not have desired dissolution properties in developer. Specially for a positive resist, the develop rate of unexposed resist should be very low, but the resist, as coated, is often porous, retains considerable solvent, and has a high develop rate as a consequence. The most common method densifying the resist is baking. The bake that immediately follows resist coating is referred to as the soft bake, prebake, or post apply bake. Among the baking methods, hot plates have provided the best temperature control. After MMA coating, it should be baked at 150 ^{0}C for 20-40 minutes until the resist layer becomes completely solid before coating the top resist PMMA. Once wafers are removed from hot plates, they begin to cool, and this cooling needs to occur in a controlled way. Wafers simply removed from the hot plates cool in irregular fashion, depending upon the airflow proximity to other still-warm wafers, and handling.

4.5.1 Electron beam exposure and patterning

Derived from the development of Scanning Electron Microscopes, Electron beam (E-beam) lithography is a process engraves and exposes patterns into the material underneath the electron beam to sensitive resists using highly focused electron beams. Electron lithography therefore has potential for very high resolution. Electron-beams image with extremely large depths-of-focus, providing relief from one the most challenging problems of typical optical lithography. The scattering of electrons in the

resist reduced when using high electron electrons, something desirable and perhaps necessary for high-resolution electron beam lithography. However, most high-energy electrons pass through the resist film deposit their energy in the underlying substrate. One limitation for e-beam lithography is the trade-off between resolution and current density in e-beam systems. When an electron beam is focused into a small volume, the individual electrons experience the electric fields of the other electrons. While the resulting average field can be compensated, there is stochastic scattering- the random electron-electron interactions that will tend to broaden the beam. In spite of the issues of productivity, direct-write electron writers have been developed and built for fast-turn applications. In this work, we used the Nanometer Pattern Generation System (NPGS) nanolithography system is capable of imprinting patterns into resist materials with a maximum writing speed of 100 kHz [7]. NPGS uses a true vector writing mode which gives the user the maximum control over the beam. For example, the beam will move along sloped lines and tangent to arcs and circles. Also, when filling arbitrary polygons, the beam will sweep parallel to one side of the polygon as specified by the user. This approach enhances the exposure quality over systems using a simple xy raster method or one that breaks each arbitrary polygon into trapezoids with different scan directions.

4.5.2 Photolithography

Photolithography is a process used in microfabrication, transferring geometric pattern on a *photomask* to a layer of photoresist (either positive or negative) on surface of a substrate. A mask or photomask is a square glass plate with a patterned emulsion of metal film on one side [8]. An important steps in the photolithography process is mask alignment. The mask is aligned with the substrate, so that any pattern can be transferred onto the desired substrates for multi-step device fabrication. With help

of photolithography, we do fabricate alignment markers on the silicon dioxide/silicon substrates for nanowire device fabrication.
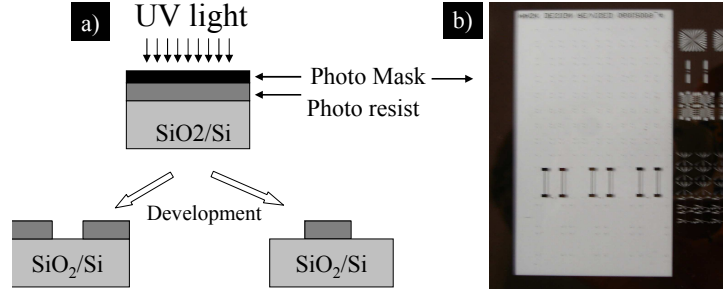

Figure 4.6 a) Photolithography process, b) A photomask

4.6 Ultra High Vacuum System

The cryopump (also called mechanical cryopump) was used metallization for the nanoscale devices. It pumps by getting gases so cold that they freeze out and are stored, or captured, in the pump. It is extremely clean-it uses no oils, and has no moving parts in vacuum. It has also very high throughput. The cryopump is intensively used in the high vacuum or ultra high vacuum (UHV) range in industrial applications where hydrocarbons cannot be tolerated. The cryopump used in thesis work is capable to pump down 1E-09 Torr (Fig. 4.7). A mechanical cryopump is made of two main components: a gaseous helium compressor and a pump consisting of a cold head, baffle, pump body and sometimes an integral high vacuum valve. Cryopumps are commonly cooled by compressed helium though they may also use dry ice, liquid nitrogen, or stand-alone versions may include a built-in cryocooler. Baffles are often attached to the cold head to expand the surface area available for condensation, but they also increase the radiative heat uptake of the cryopump. Over time, the surface eventually saturates with condensate and the pumping speed gradually drops to zero. It will hold the trapped gases as long as it remains cold, but it will not condense fresh

gases from leaks or backstreaming until it is regenerated. Regeneration of a cryopump is the process of evaporating the trapped gases. This can be done at room temperature and pressure, or the process can be made more complete by exposure to vacuum and faster by elevated temperatures. Best practice is to heat the whole chamber under vacuum to the highest temperature allowed by the materials, allow time for outgassing products to be exhausted by the mechanical pumps, and then cool and use the cryopump without breaking the vacuum [9]. Cryopumps are often combined

Figure 4.7 Ultra High Vacuum Cryopump

with sorption pumps by coating the cold head with highly adsorbing materials such as activated charcoal or a zeolite. As the sorbent saturates, the effectiveness of a sorption pump decreases, but can be recharged by heating the zeolite material (preferably under conditions of low pressure) to outgas it. The breakdown temperature of the zeolite material's porous structure may limit the maximum temperature that it may be heated to for regeneration.

4.7 Semiconductor Parameter Analyzer

A semiconductor parameter analyzer (SPA) contains voltage sources, current sources, voltage monitors, and current monitors that can be programmed via a menu-driven user-interface. An SPA is very useful for characterizing semiconductor devices. Pos-
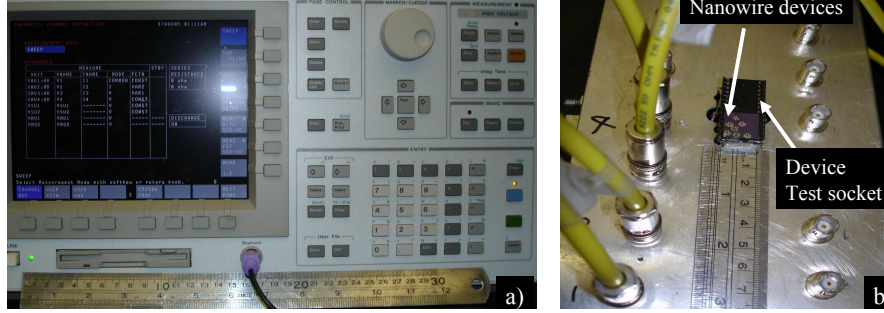

Figure 4.8 a. Agilent 4156C Precision Semiconductor Parameter Analyzer, b) Device test socket

sible measurements include, I-V curve of a simple two terminal device, I_d-V_{ds}-V_g graphs for the metal oxide semiconductor field-effect transistor (MOSFETS), switching characteristics of logical gates, etc. In this project, we have used Agilent 4156C Precision Semiconductor Parameter Analyzer which offers four source monitor units (SMUs), two voltage source units (VSUs), and two voltage monitor units (VMUs). It can limit output voltage or current to prevent damaging the devices under test in which $0V \leq Voltage \leq \pm 100V$ and $\pm 100fA \leq \pm 100mA$ [10]. Output voltage or output current of each SMU can be held constant or can be swept by specifying the source function field (CONST, VAR1, VAR2) on the Channel Definition. A user can specify output voltage and current, sweep mode (linear or log), start, stop , step , and compliance (maximum current/voltage) on the source setup page.

Bibliography

[1] J. Goldstein, D. E. Newbury, D. C. Joy, P. Echlin, C. E. Lyman, E. Lifshin, L. Sawyer, *Scanning electron microscopy and x-ray microanalysis*, 3rd edition, Springer, (2003)

[2] L. Reimer, *Scanning Electron Microscopy: Physics of Image Formation and Microanalysis*, Springer Series in Optical Sciences, 2nd edition, Springer, (1998)

[3] A. C. Buechele, D. McKeown, K. Klatt, I. L. Pegg, J. Beres, P. B. Mavedo, *Wide angle X-ray Diffraction Procedure*, Vitreous State Laboratory Provedure, TPI-XRAY, The Catholic University of America, (2005)

[4] John Clarke (Editor), *The SQUID Handbook, Volume 2: Applications of SQUIDs and SQUID Systems (Hardcover)*, First edition, Wiley-VCH; (2006)

[5] D. McKeown, M. Penafiel, L. Alar, I. L. Pegg, *Instructions for Collecting Spectra Using the Micro-Raman System*, Vitreous State Laboratory Procedure, TPI-Raman, The Catholic University of America, (2008)

[6] H. J. Levinson, *Principles of Lithography*, 2nd edition, SPIE Press, (2005);

[7] http://www.jcnabity.com/

[8] *Handbook of Microlithography, Micromachining, and Microfabrication*, Vol 1: Microlithography, Editor P. Rai-Choudhury, SPIE Press, (1997)

[9] *Basic Vacuum Practice*, Varian vacuum products 3rd edition, (1992)

[10] *Agilent Technologies 4156C Semiconductor Parameter Analyzer Manual* http://www.home.agilent.com/agilent/product.jspx?pn=4156C

Chapter 5

Spin dependent transport properties of manganite nanowires

5.1 Background

Most of the research works of Colossal magnetoresistance-manganese oxides have been focused on 3D bulk and 2D thin film forms [1,2], but there are very few studies exist for nanostructure forms. The reasons is synthesis of the manganites nanostructures are difficult. However, recently magnetic properties of the nanowire, and nanopowder of the $La_{0.7}Sr_{0.3}MnO_3$ (LSMO) and $La_{0.7}Ca_{0.3}MnO_3$ (LCMO) have been reported in elsewhere. For example, K. S. Shankar *et al*., 2004 reported growth of oriented nanowires of manganites within the pores of anodic alumina (AAO) templates [3]. Same year, S. Han *et al*. fabricated colossal magnetoresistive, MgO/LCMO core-shell nanowires by pulsed laser deposition process [3]. A. Carretero-Genevrier *et al*. produced single-crystalline $La_{0.7}Sr_{0.3}MnO_3$ nanowires by Polymer-Template-Directed Chemical Solution Synthesis in 2008 [4], but none of them fabricated and characterized nanoscale devices made by single doped manganese oxides.

5.2 Experiment

For this work, we employed commercially available following precursors for $La_{0.67}Sr_{0.33}MnO_3$ and $La_{0.67}Ca_{0.33}MnO_3$ nanowire synthesis.

- Lanthanium Nitrate: $La(NO_3)_3x6H_2O$

- Manganese Nitrate: $Mn(NO_3)_2x2H_2O$

- Stronium Nitrate: $Sr(NO_3)_2$
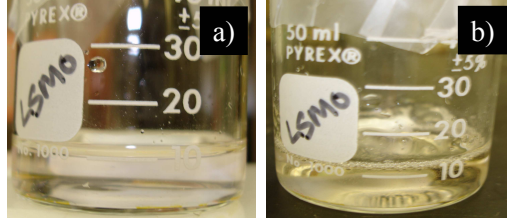
- Calcium Nitrate: $Ca(NO_3)_2x4H_2O$

Figure 5.1 a) La-Sr-Mn aqueous solution, b) A resultant gel solution in which polyvinylpyrrolidone beads were dissolved in the aqueous solution

Based on our experimental results, we are introducing following the recipe for fabricating quality electrospun manganites nanowires: The aqueous solution of appropriate amounts of commercially available 3 gm batch of 99.9 % (REO) $La(NO_3)_3x6H_2O$ (Alfa Aesar), 99.98% $Mn(NO_3)_2x2H_2O$ (Alfa Aesar) and 99.996% $Sr(NO_3)_2$ (Alfa Aesar) or 99.995% $Ca(NO_3)_2x4H_2O$ (Alfa Aesar) were initially dissolved in 5 gm of deionized water with magnetic stirring at room temperature for over night. The ration of the solvent to the PVP polymers was 6:1. The mixture of colorless La-Sr-Mn aqueous solution is diplayed in Fig. 5.1 a. As a next step, 0.7 g of polyvinylpyrrolidone (PVP) beads were slowly added to the aqueous solution and resultant gel solution

was vigorously stirred for another 3 hours at room temperature. Fig. 5.1 b. displays viscous, colorless a resultant gel solution that is ready for the electrospinning process. It should be noted that in our early experiments, we used polyethylene oxide (PEO) and polyvinyl alcohol (PVA) polymers to bind the aqueous solutions, but our experiments indicate that PVP is more suitable for the manganites. PVP dissolved aqueous solutions gives out high quality, continuous and much thinner nanowires compare to the that of PVA or PEO dissolved resultant solutions. A high voltage of 25 kV was
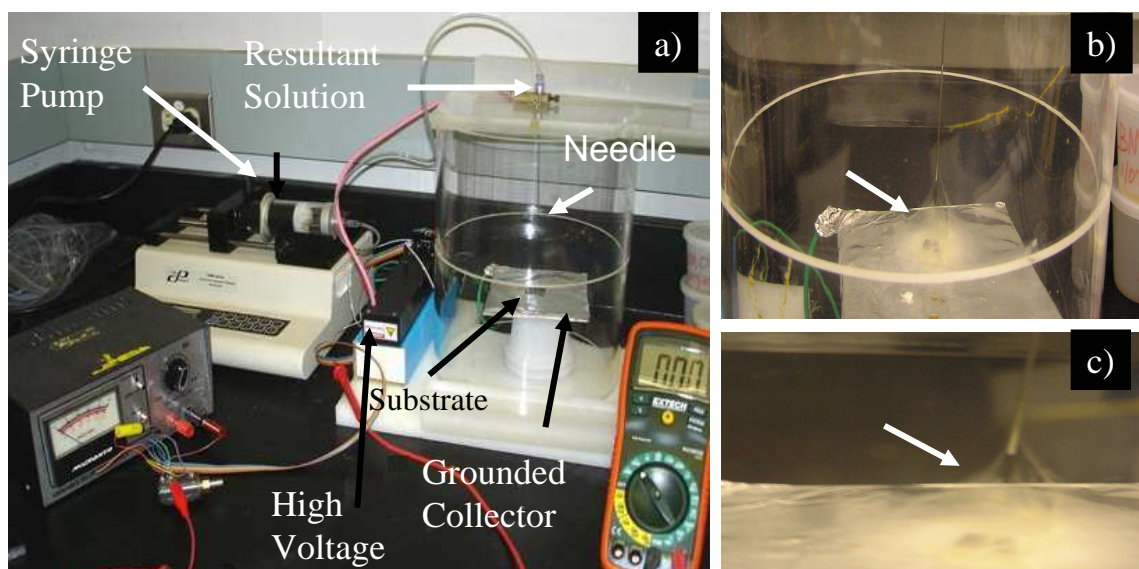

Figure 5.2 a) A electrospinning setup that was used in this work, b-c) The electrospinning process in progress

applied to the vertically positioned needle with an inner diameter of 0.4 mm was connected to a reservoir containing the resultant solution and a base collector plate (Fig. 5.2 a). Most cases, the needle was simply dipped into the resultant gel solution and clamped to the anode of a high voltage power supply. A large electric field induces an electrostatic jet from the solution that is then accelerated and stretched to form fine, continuous bundle of nanofibers or nanowires on a desired substrate, which was placed 15 cm from the tip of the needle on an aluminum cathode (Fig. 5.2 b-c).
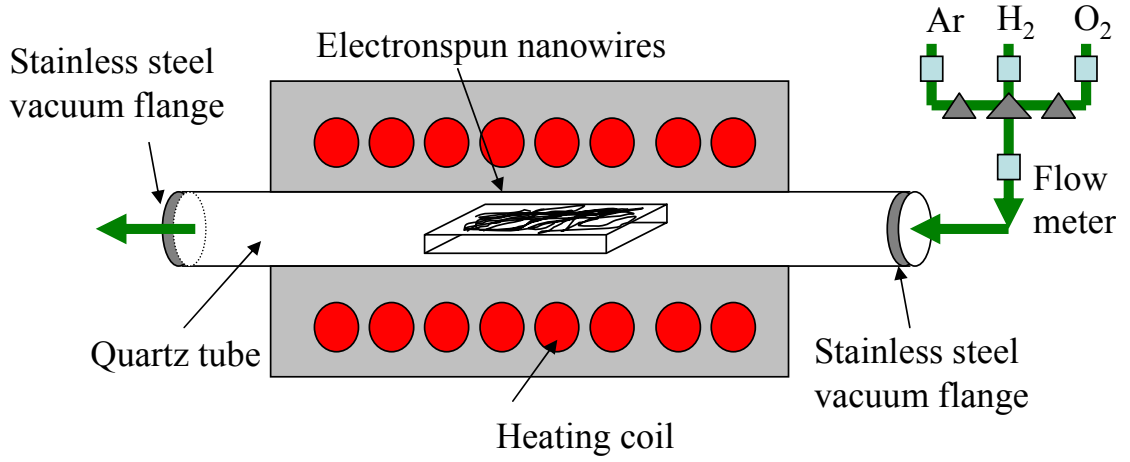
Figure 5.3 a) Scheme of a tubular furnace used for annealing the nanowires

After the electrospinning process, the collected nanowires were annealed in a tubular furnace as illustrated in Fig. 5.3 at 500 ^{0}C in ultra-high purity argon gas (1L/min flow rate) and 3% hydrogen (0.75 scfh flow rate) mixture. We call this process as a *first heat* treatment and it usually takes three hours in order to remove the polymer shield. As the polymer was selectively removed during the heat treatment, the nanowires remained as continuous structures, with reduced diameters. Immediately after first heat treatment, we increased the furnace temperature to 750 ^{0}C and the gas changed to oxygen (1L/min flow rate)into the furnace. We call this process as a *second heat treatment.* This process is required to form LSMO (or LCMO) nanostructure(s) which takes an additional three hours. Once the second heat treatment process is finished, thin and continuous LSMO (or LCMO) nanowires were obtained and where randomly distributed parallel to the substrate that are shown in Fig. 5.4 a-b. In chapter 3, we discussed importance of well aligned, parallel nanowires for device applications.
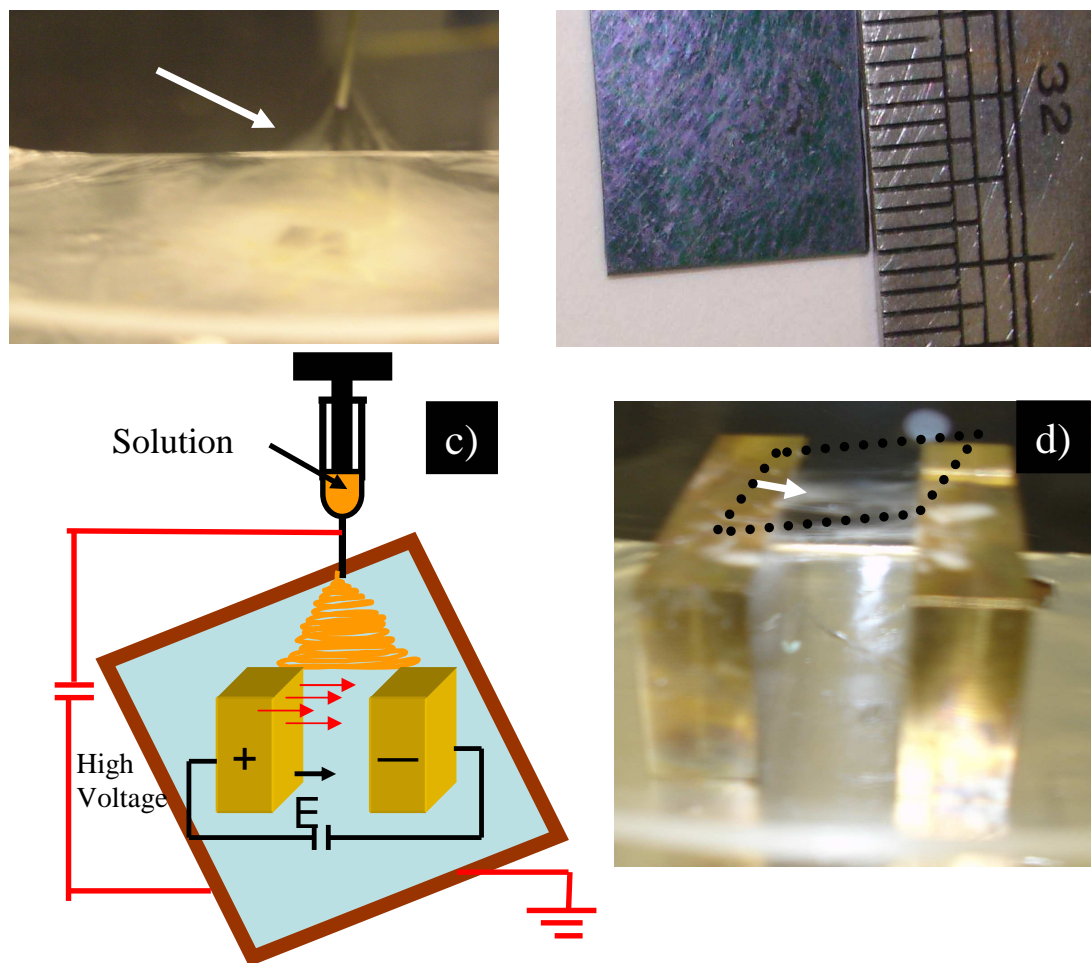
Figure 5.4 a) Electrospinning process, b) A optical photographic images of the randomly distributed bundle of La-Sr-Mn nanowires, c) Electrospinning setup for aligned doped manganese oxides, d) La-Ca-Mn aqueous solution was electrospun in the presence of an electric field between the two brass blocks

Although the electrospinning process is fairly straightforward, controlled production of aligned wires or fibers reproducibly on a substrate remains a major challenge. For aligning doped manganese oxides, we have used two brass block and applied small voltage between them (12V). Once electrospin process begin, the electric field between the prisms align the electrospun nanowires as shown in Fig. 5.4 c-d.

5.3 SEM characterization

The morphology of the wires was examined by scanning electron microscopy (SEM - JEOL JSM-5910LV). Fig. 5.5 and Fig. 5.6 show images of the randomly distributed LSMO and aligned LCMO nanowires respectively. SEM image reveals uniform, smooth, continuous high aspect ratio of LSMO and LCMO nanowires with diameters in the range 80-300 nm and hundreds of microns in length. Statistically we estimated that average diameter of the nanowires were 120-150 nm. The EDS analyses confirm the uniformity of LSMO and LCMO phases over the entire length of the wires. We
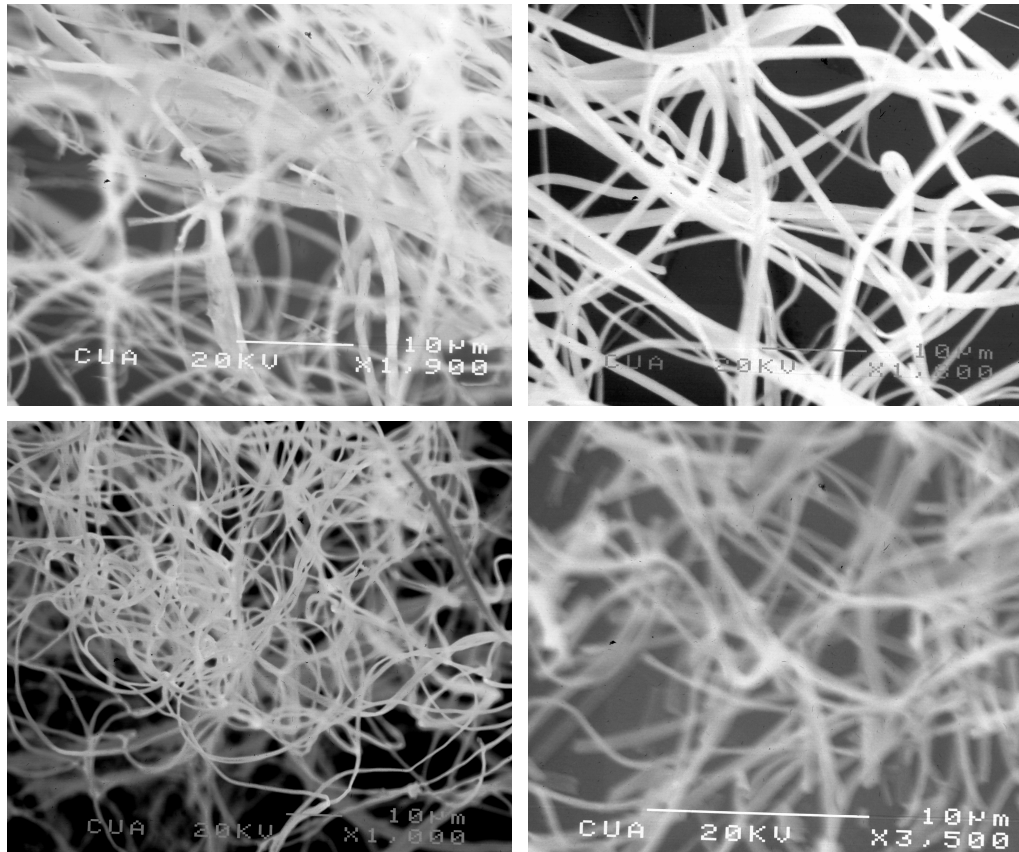

Figure 5.5 SEM images of randomly grown LSMO nanowires

observed that the good morphology and surface smoothness of the nanowires strongly depend on mostly following factors: 1) Choosing right polymers. We initially used

PEO and PVA polymers and did not produce high quality nanowires. We demonstrate that PVP is perfectly worked for doped manganese oxides (LSMO or LCMO), ii) Ratio of aqueous solution to polymer. SEM images show highly viscous solutions prepared by certain ratio of La, Mn, Sr or Ca nitrates and the PVP polymer were electrospun and resulting in nanowires with larger diameters , around 200-800 nm, but less viscous solution mixture yields thin wires. Therefore, finding a right ratio of the polymer and aqueous solution is the key to obtain high quality nanowires. iii) Applied high voltage and distance between needle and collector plate. We have optimized 25 k V for the voltage and 18 cm for the distances. iv) Annealing temperature. Proper annealing is important smoothness of the nanowires. We set and maintained the heating rate of the furnace at 2 degree/min for the both first and second heat treatment processes.
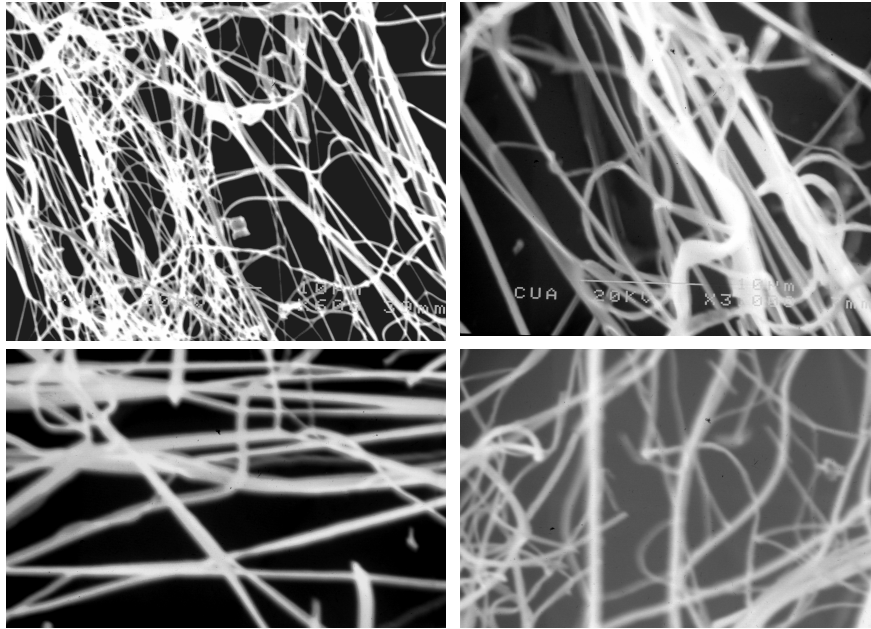

Figure 5.6 SEM images of aligned and partially aligned LSMO nanowires

5.4 XRD characterization

X-ray diffraction (XRD) patterns were recorded with a Thermo ARL diffractometer with Cu-K$_\alpha$ radiation between 2θ, 5 and 80^0 at a scan rate of 10^0 min^{-1}. XRD results confirm that the electrospun La$_{0.7}$Sr$_{0.3}$MnO$_3$ and La$_{0.7}$Ca$_{0.3}$MnO$_3$ nanowires spectra can be indexed to an orthorhombic pervoskite structure without any other secondary phase (Fig. 5.7). The EDS analyses confirm the uniformity of LSMO phase over the entire length of the wires.
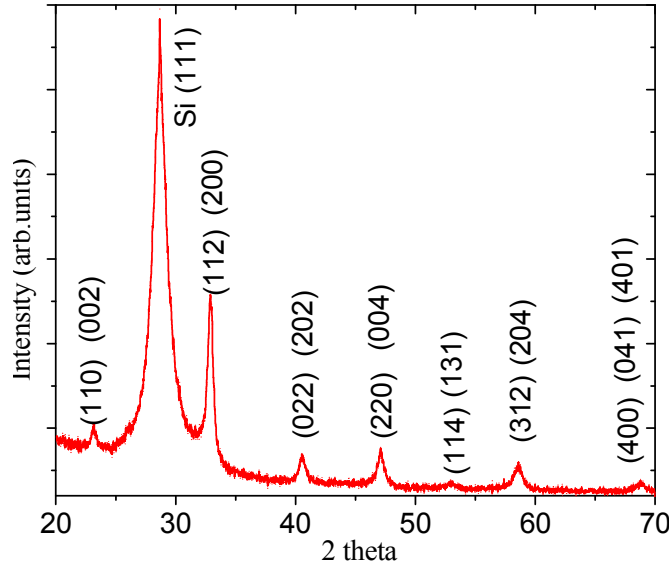

Figure 5.7 XRD spectra of electrospun La$_{0.67}$Sr$_{0.33}$MnO$_3$

5.5 Raman Spectra

5.5.1 Background

Raman spectra of undoped and doped La$_{1-x}$M$_x$MnO$_3$ (M= Sr, Ca) single crystals and thin films have been reported elsewhere in the temperature range from 5 to 423 K [7]. Earlier X-ray diffraction studies have shown that crystal structure of

$La_{0.67}Sr_{0.33}MnO_3$ electrospun nanowires is orthorhombic. The other investigations show that the orthorhombic perovskite phase of the parent $LaMnO_3$ has the same the space group $(D_{2h}{}^{16})$ as doped LSMO [6]; and at the zone center, the following 60 phonon modes are allowed:

- $\Gamma = 7A_g + 5B_{1g} + 7B_{2g} + 5B_{3g}$ (Raman active)

- $9B_{1u} + 7B_{2u} + 9B_{3u}$ (IR active)

- $8Au$ (Silent)

- $B_{1u} + B_{2u} + B_{3u}$ (Acoustic)

where, $A_g \rightarrow \alpha_{xx}, \alpha_{yy}, \alpha_{zz}$ $B_{1g} \rightarrow \alpha_{xy}, \alpha_{yx}$ $B_{2g} \rightarrow \alpha_{xz}, \alpha_{zx}$ $B_{3g} \rightarrow \alpha_{yz}, \alpha_{zy}$

5.5.2 Experiment

Undoped $LaMnO_3$ as well as doped $La_{0.9}Sr_{0.1}MnO_3$ and $La_{0.67}Sr_{0.33}MnO_3$ nanowires were grown on both amorphous SiO_2 (quartz) and Si substrates. At least four different samples were chosen for the each particular material. A single-grating spectrograph and notch filter micro-Raman system [see Chapter 4] was used to gather the Raman spectra at room temperature. A Melles-Griot Model 35-LAP-431-208 Ar+ laser provided the 5145 Å wavelength incident light that was directed through a broad band polarization rotator (Newport Model PR-550) to the laser microscope which guided the laser light down to the sample surface through a long working distance Mitutoyo 10x microscope objective. The laser-light was focused to a 10 micron diameter spot on each sample. The laser light power was approximately 25 mW at the sample. Due to the weak Raman scattering from the samples investigated, room temperature unpolarized spectra were gathered in back-scattering geometry. After the analyzer, the scattered light proceeded through holographic notch and super-notch filters (Kaiser

Optical Systems), which reduced the Rayleigh scattered light intensity by ten optical densities. The notch filters were oriented in the scattered light path so that the filter cut off frequency was minimized to near 70 cm^{-1} from the laser line. The spectrograph used a 1200 gr/mm grating (Richardson Grating Laboratory) that was set to disperse the Stokes scattered light from the sample on to a 2048 x 512 element Peltier cooled CCD detector (Model DU440BV, Andor Technology). The JY-Horiba HR460 spectrograph were set to 6 cm^{-1} resolution for the 1200 gr/mm grating to collect spectra and from 50 to 1600 cm^{-1}, respectively. The spectrograph was frequency calibrated using CCl4, so that the recorded frequencies are accurate to within ± 1 cm^{-1}.

5.5.3 Result

In a single crystalline bulk LaMnO$_3$, lines of A_g symmetry are observed at 140, 198, 257, 284, and 493 cm^{-1}, of B_{2g} symmetry at 109, 170, 308, 481, and 611 cm^{-1}, and of B_{1g} and B_{3g} symmetry at 184 and 320 cm^{-1} respectively [6]. In the Raman spectrum (RS) of the undoped electrospun LaMnO$_3$ nanowires, we only observed the most intense broad B$_{2g}$ peak at $\sim$670 cm^{-1} (Fig. 5.8 a). For single crystalline bulk LaMnO$_3$, B$_{2g}$=611 cm^{-1} (M. N. Ilievi et al., 1998) and it corresponds to the pure oxygen and Mn-O vibrations. Interestingly, a theoretical investigation using lattice dynamical calculations (LDC) predicts a B$_{2g}$ mode at 669 cm^{-1} which is consistent with our experiment [6]. It is well known that the broadened phonon profiles, which may be caused by excess charges introduced by La doping, lead to a large overlap. In detail, these excess charges activate Jahn Teller (JT) distortion of Mn-O octahedran and induce, to some extent, lattice disorder. We conclude that in nanowire form, the JT distortion behavior is different compared with that in bulk materials. Studies show a corresponding Raman mode observed for single crystal La$_{1-x}$M$_x$MnO$_3$ (M=Sr,

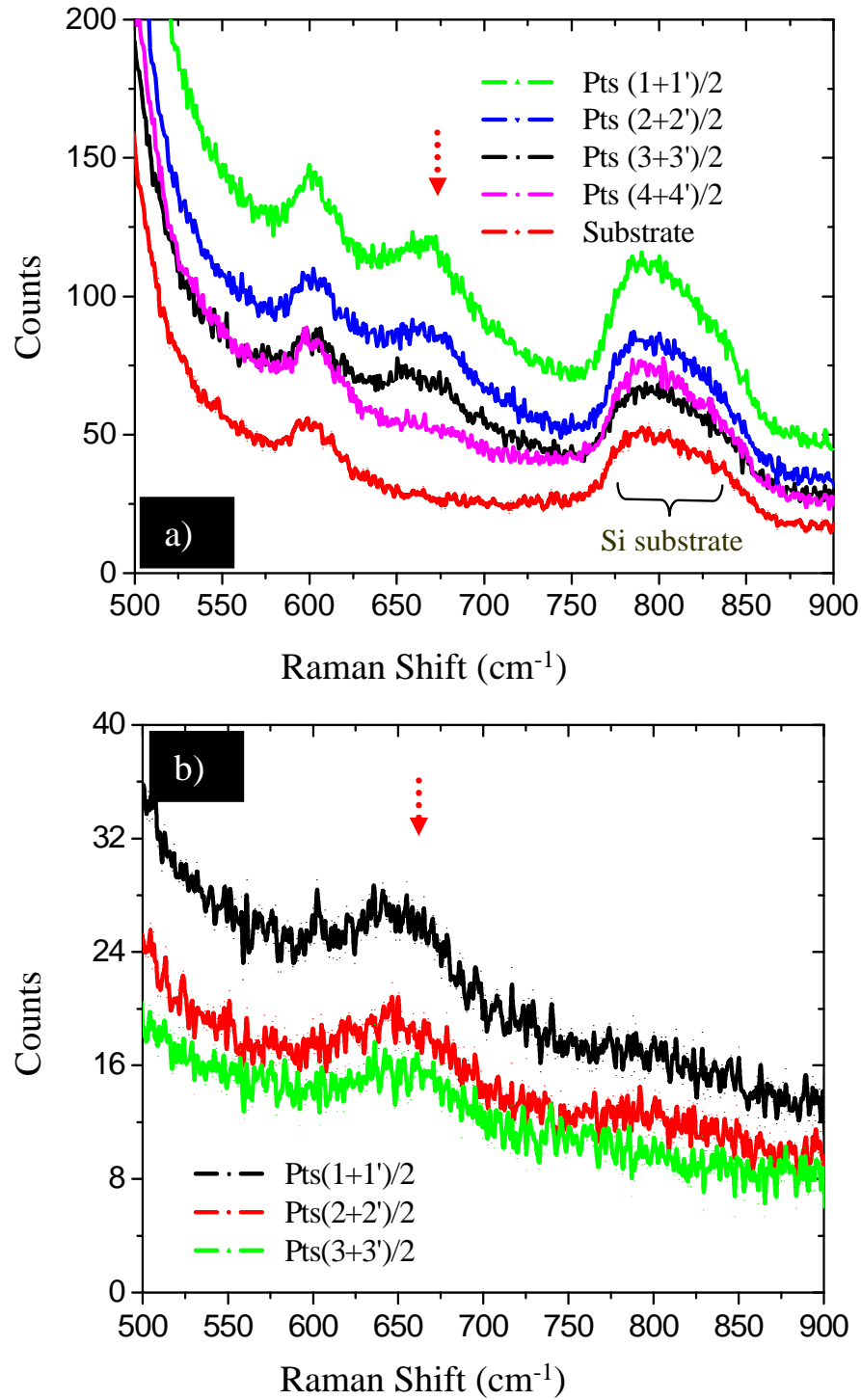**Figure 5.8** RS spectra: a) undoped LaMnO$_3$ grown on amorphous SiO$_2$ substrate, b) La$_{0.9}$Sr$_{0.1}$MnO$_3$ grown on amorphous SiO$_2$ substrate

Ca) materials may be presented as a superposition of two components: first-order RS and second order RS. We observed a peak at 650 cm^{-1} in the RS of $La_{0.9}Sr_{0.1}MnO_3$ nanowires. According to S. Yoon *et al.*, 1998 and M. V. Abrashev *et al.*, 1999, this peak corresponds to tilting or rotation of the MO_6 octahedra (see Chapter 2.1.1). To compare undoped $LaMnO_3$, the peak has shifted in lower wavelength and intensity of the peak significantly decreased (Fig. 5.8 b). This features are also observed in RS spectra of $La_{0.67}Sr_{0.33}MnO_3$ nanowires and the intensity of the Raman peak was observed around 650-670 cm^{-1} was further decreased ((Fig. 5.9 a-b). This behavior is also observed in bulk orthorhombic manganites. The intensity change at x>0 is explained by the smaller Jahn Teller distortion of the nearly cubic $La_{1-x}M_xMnO_3$ (M=Sr, Ca) structure. It has been stated that nature of interaction between La/Sr ions and MnO_6 octahedra that can overcompensate the mass effect. While the La or Sr ions occupy the sites between oxygen octahedra in $La_{1-x}M_xMnO_3$ compounds, it was shown (W. Archibald et al., 1995) that the ionic radius of this site increases with Sr doping. V. B. Podobedov *et al.* in 1998 considered that the increase of the ionic radius strongly affects the force constant in the MnO_6 vibrational system. This effect explains the corresponding change in the Raman shift of the related low frequency mode.
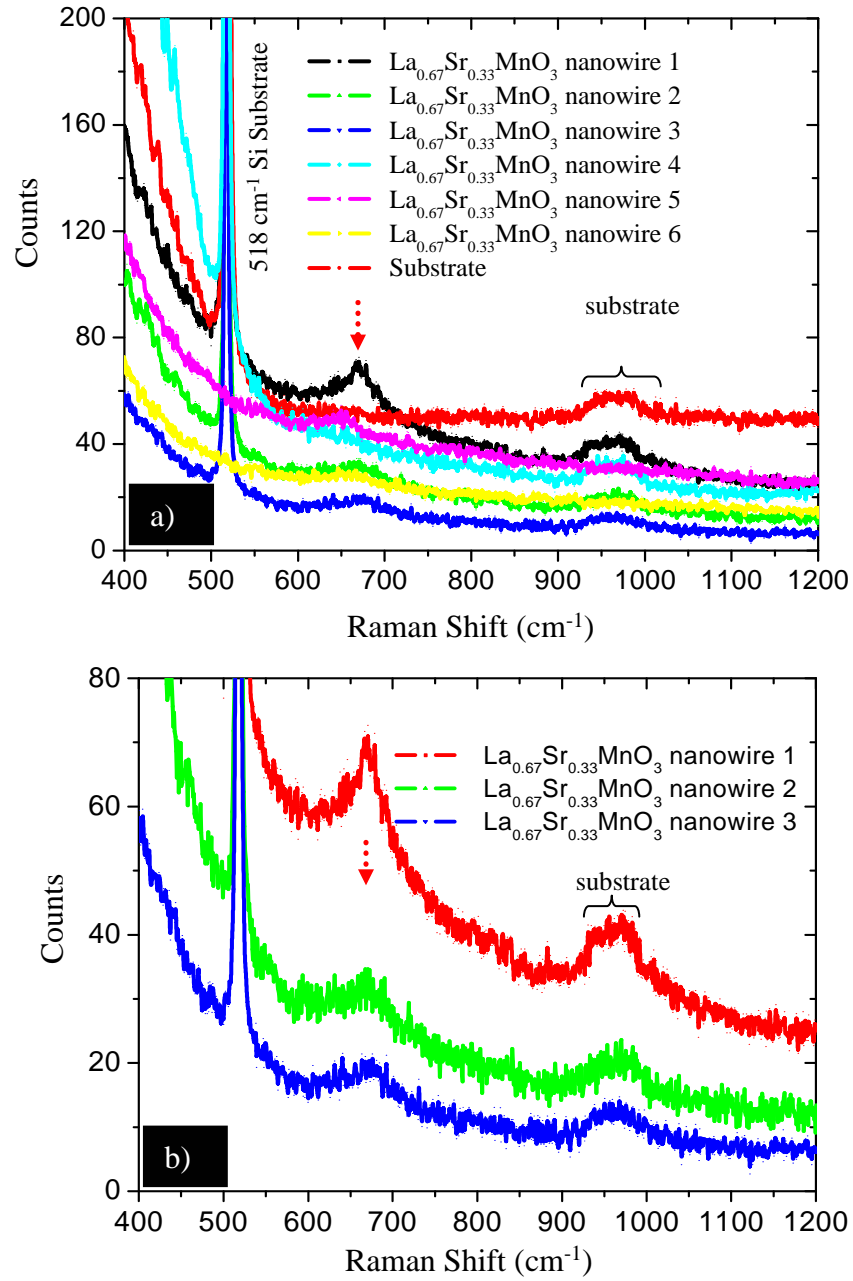
Figure 5.9 RS spectra: a) $La_{0.67}Sr_{0.33}MnO_3$ nanowires are grown on Si (111) substrate, b)high quality $La_{0.67}Sr_{0.33}MnO_3$ nanowires are grown on amorphous SiO_2 substrate

5.6   Magnetic Properties

Magnetic characterization was performed with a Quantum Design model MPMS magnetic property measurement system (SQUID magnetometer) with magnetic quench option. Magnetization measurements of field cooled and zero field cooled samples were obtained with increasing temperatures. Figure Fig. 5.10 shows out of plane
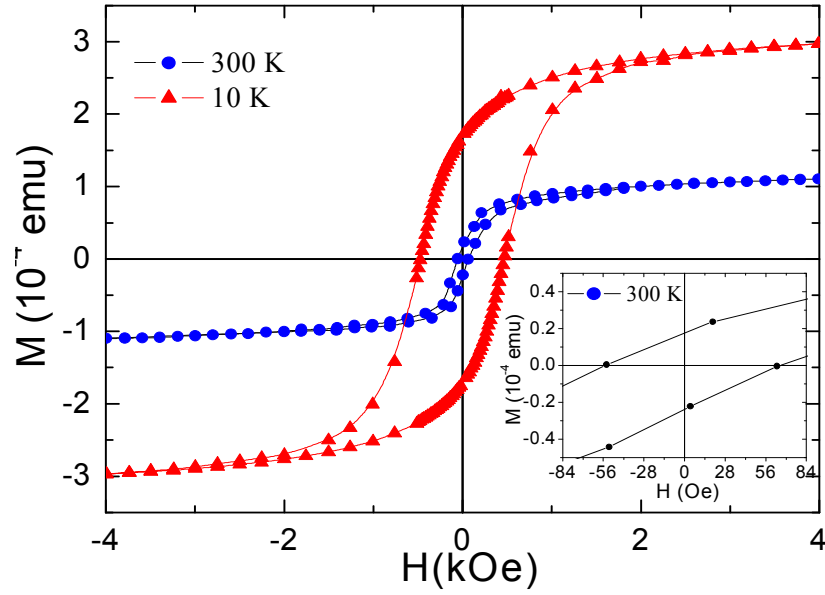

Figure 5.10 Magnetic Properties of $La_{0.67}Sr_{0.33}MnO_3$ Nanowires

(the external field was applied perpendicular to the substrate) hysteresis loops of $La_{0.67}Sr_{0.33}MnO_3$ nanowires having diameters range 80-300 nm. The hysteresis loops of the nanowires at 10 K and 300 K revealed the ferromagnetic ordering existing in the $La_{0.67}Sr_{0.33}MnO_3$ nanowires. At 10 K, a clear hysteresis loop with remanent magnetization, M_r=1.70x10^{-4} emu and coercive field H_c=471 Oe are observed. At 300 K, the remanent magnetization, M_r=1.75x10^{-5} and coercive field, H_c=65 Oe, become smaller, which may be due to the intrinsic magnetically soft properties, but the loop still shows the features of ferromagnetism.

5.6.1 Magnetization versus Temperature

The temperature dependence of magnetization for the LSMO nanowires with an applied magnetic field of 2000 Oe is shown in Fig. 5.11 a with a Curie temperature above room temperature. The nanowires show sharp transition temperature from paramagnetic to ferromagnetic state around 350 K. The value was smaller than the work of bulk LSMO transition temperature reported at 369 K (A. Urushibara *et al.*, 1995). Smaller transition temperature also was reported in LSMO nanophase system where it was 324 ^{0}C for 700 ^{0}C annealed sample (A. Gaur and G.D. Varma., 2006). The temperature dependence of magnetization for electrospun LCMO nanowires is diplayed in Fig. 5.11 b. The curie temperature for LCMO show similar value for that of single crystalline LCMO microwires (C. A. Cardoso *et al.*, 2003)

5.7 Spin Dependent Transport

As described in Chapter 4.6, as-grown nanowires were sonicated in isopropanol alcohol and then individual $La_{0.67}Sr_{0.33}MnO_3$ nanowires were dispersed onto to heavily doped p-type Si chips capped with a oxide layer. Two layers of electron beam resist, 540 nm thick, methylmethacrylate (MMA) and polymethylmethacrylate (PMA) were spin coated onto to the chip and each was baked for 150 ^{0}C for 20 minutes (see Chapter 4.6). 100 nm Ti/Cu electrodes were deposited to the selected nanowire's by high vacuum electron beam evaporator (Fig. 5.12) The electrical measurement was carried out using an Agilent 4156C semiconductor parametric analyzer at room temperature. Figure. 5.12 shows single phase $La_{0.67}Sr_{0.33}MnO_3$ nanowire devices. All devices were stored in a high vacuum chamber so that oxidation of the electrodes or the interface is avoided. The gate voltage did not significantly change I-V characteristics and set to zero. Devices were annealed at 350 ^{0}C for 15 minutes in high purity Ar for better
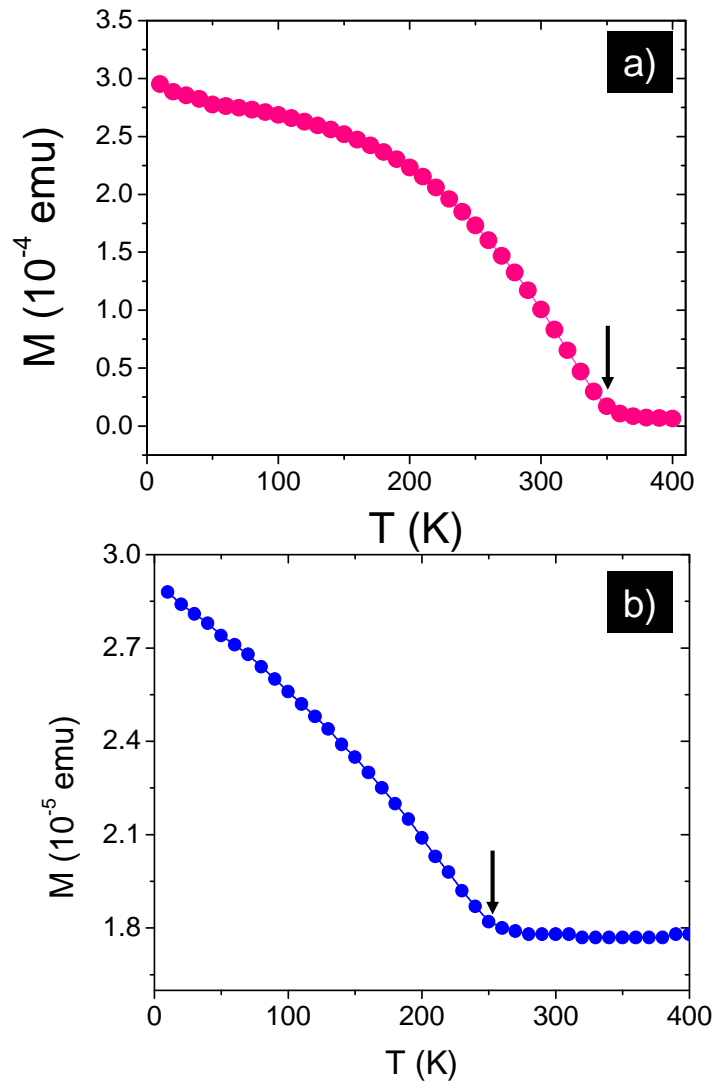
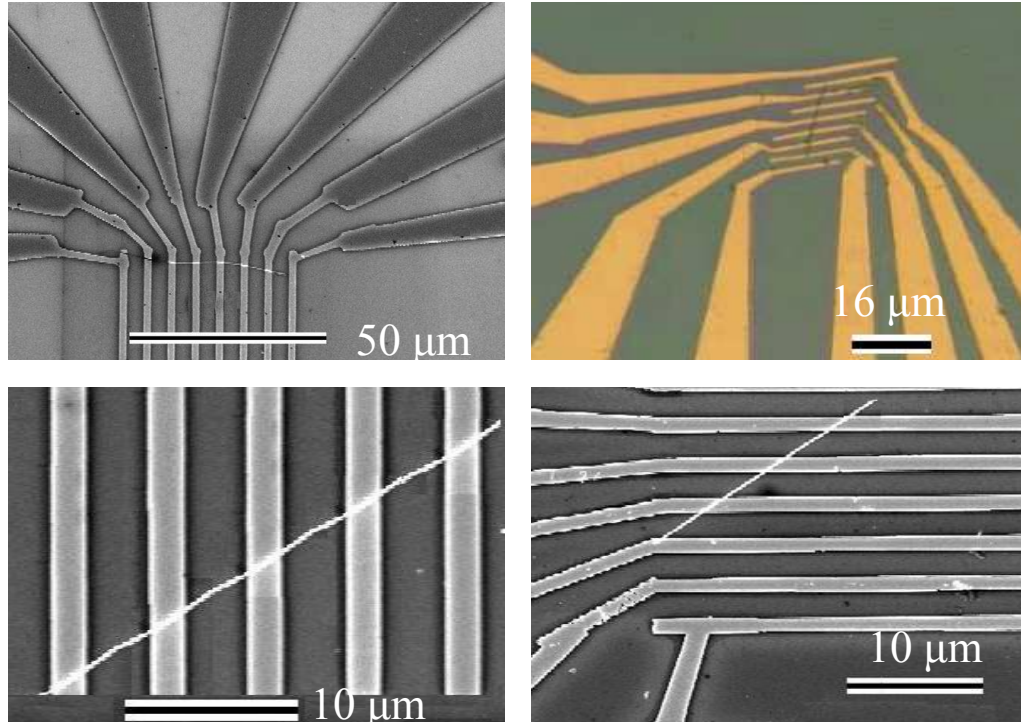**Figure 5.11** Magnetic field vs temperature: a) $La_{0.67}Sr_{0.33}MnO_3$, b) $La_{0.67}Ca_{0.33}MnO_3$

Figure 5.12 Electrical contact to a single $La_{0.67}Sr_{0.33}MnO_3$ nanowires

electrical contact.

5.7.1 Result

Electrical transport properties of single La-Sr-Mn-O nanowire devices (x=0.33) were investigated with and without magnetic field. When a magnetic field of 600-1000 G was applied to the axial direction of the nanowires, the I-V characteristics significantly changes with higher current in due to presence of the field. Switching off magnetic field produces same I-V response we observed earlier. We fabricated eighteen different $La_{0.67}Sr_{0.33}MO_3$ devices and twelve of them have shown repeatable good results. The nanowires contacted with Ti/Cu electrodes deposited in ultra high vacuum system described in Chapter 4 exhibited current-voltage curve at room temperature with currents in the nanoampes. Experimental evidence of first device show

that $La_{0.67}Sr_{0.33}MO_3$ nanowires exhibit large spin-dependent transport properties in relatively low magnetic field around 600-1000 G at ambient temperature (Fig. 5.13 a). If we recall bulk La-Sr-Mn-O system (Fig. 5.13 b), the resistivity was changed under high magnetic field about 5-15 Tesla (1 Tesla=10,000 Guass). Rest of almost all devices have shown similar I-V effect with first device and they were consistent with each other. (Fig. 5.14) and (Fig. 5.15). Some cases devices with bad interface show small change and increasing voltage responds almost zero current (Fig. 5.16).
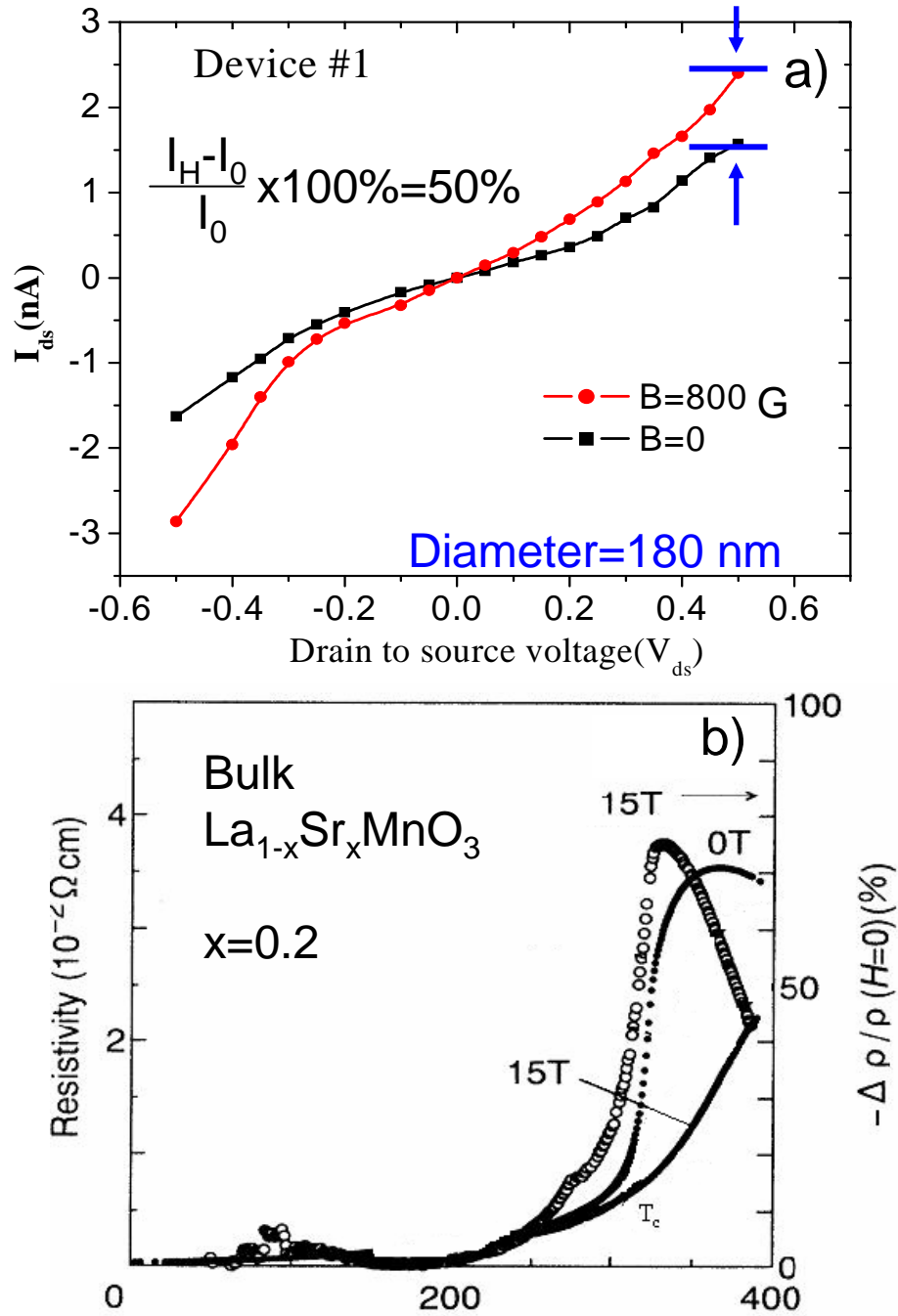
Figure 5.13 a) Device 1: I-V characteristics of the electrospun La$_{0.67}$Sr$_{0.33}$MnO$_3$ Nanowires, b) Resistivity of bulk La$_{0.67}$Sr$_{0.33}$MnO$_3$ [2]

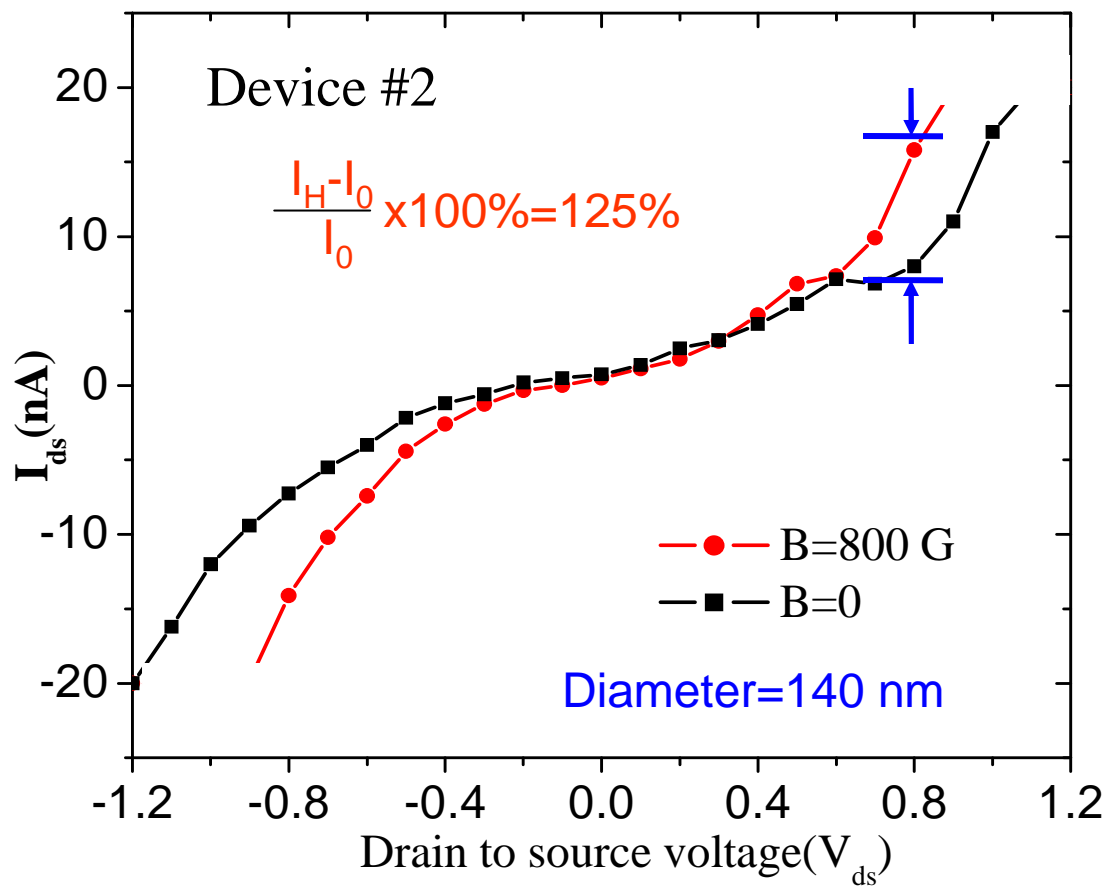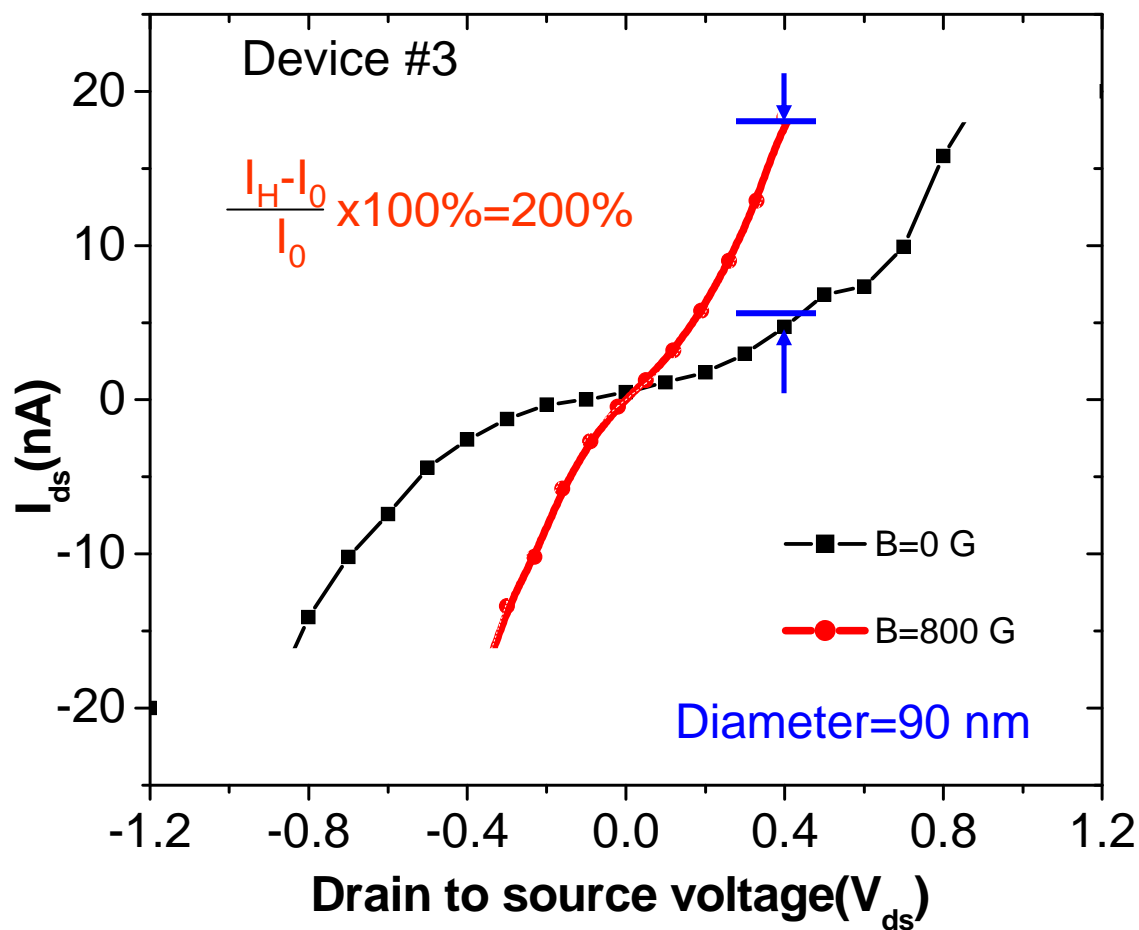**Figure 5.14** a) Device 2: I-V characteristics of the electrospun $La_{0.67}Sr_{0.33}MnO_3$ Nanowires

Figure 5.15 a) Device 3: I-V characteristics of the electrospun La$_{0.67}$Sr$_{0.33}$MnO$_3$ Nanowire

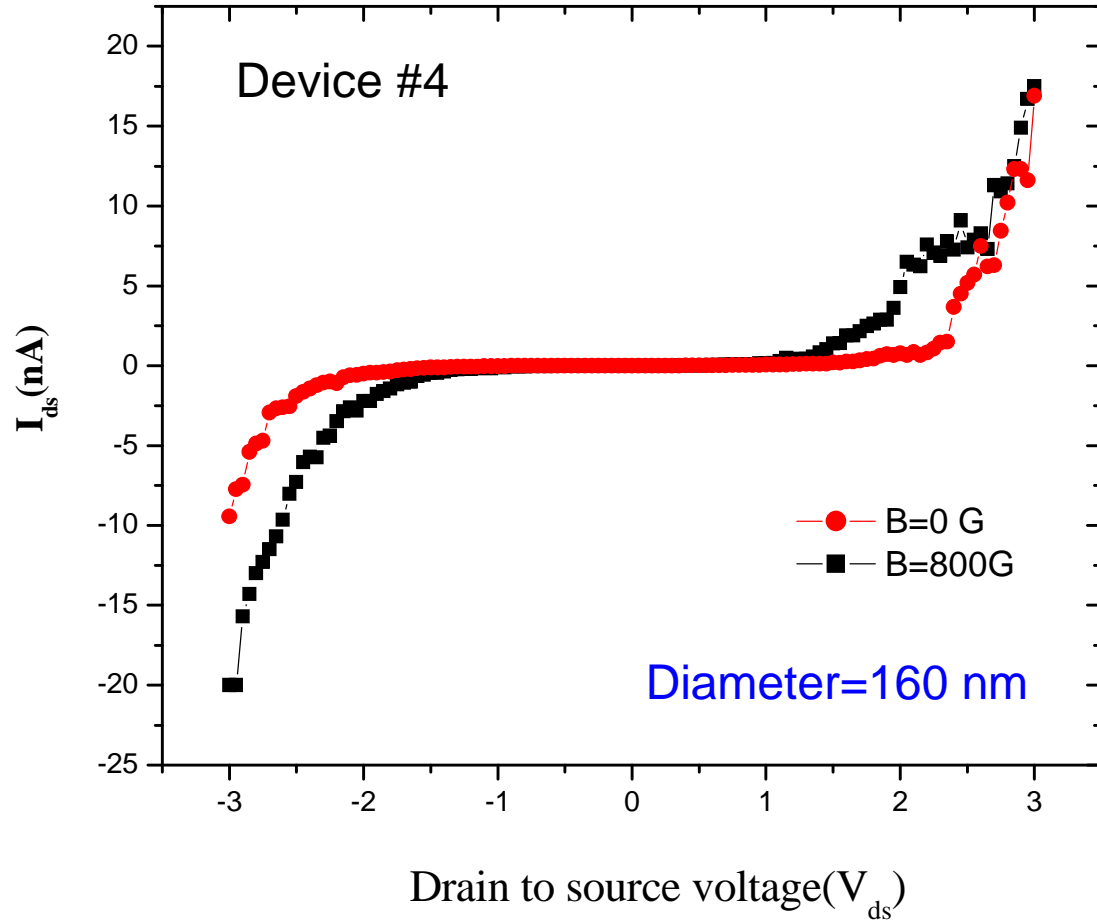**Figure 5.16** a) Device 4: I-V characteristics of the electrospun $La_{0.67}Sr_{0.33}MnO_3$ nanowire with bad interface

We also measured temperature dependent I-V characteristics for a number of LSMO nanowires with diameter ranges 120-170 nm. Nanowire device on a socket is mounted on copper plate inside a cylinder that was surrounded by a vacuum system able to be filled with liquid nitrogen. The ability to fill the system with liquid nitrogen allowed for measurements at temperatures as low as 150 K and even lower. A thermocouple was attached to the copper block to enable the temperature to be carefully monitored. The arrangement of the apparatus is shown in Fig. 5.17. Measurement data were recorded for both cooling down as well as heating back cycles. Decreasing with temperatures, LSMO nanowires show seminconducting behavior contrast to metallic behavior in bulk system (Fig. 5.18).
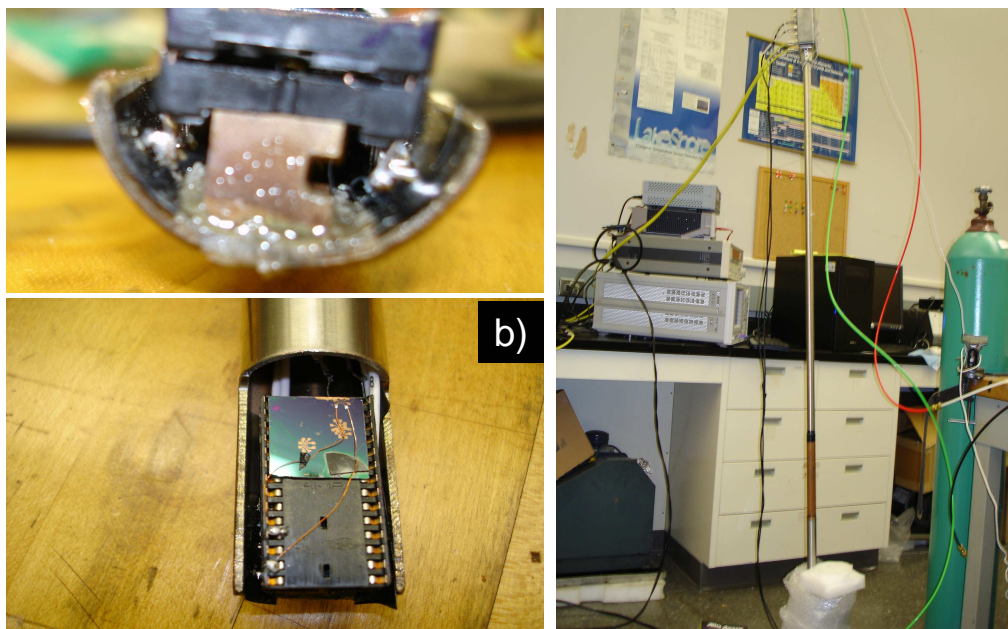

Figure 5.17 a- b) For low temperature electrical transport measurement, a sample was mounted on copper plate in a cylinder, c) The cylinder was surrounded by a vacuum system able to be filled with liquid nitrogen
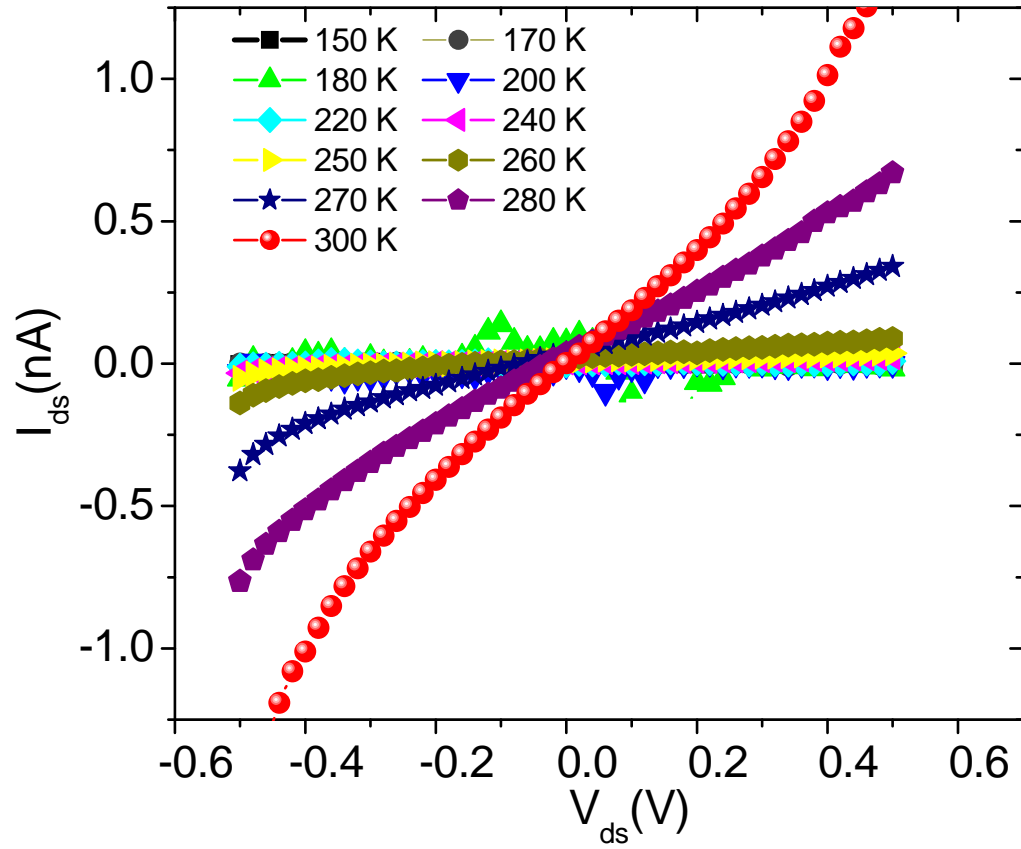
Figure 5.18 Low temperature electrical transport measurement for a LSMO nanowire with diameter 120 nm

Bibliography

[1] Advanced in condensed matter science Vol II, *Colossal magneto-resistive oxides*, edited by Y. Tokura, Gordon and Breach Science Publishers, (2000); R. Valenzuela, *Magnetic Ceramics*, London, Cambridge University Press, (1994)

[2] A. Urushibara, Y Moritomo, T. Arima, A. Asamitsu, G. Kidoa, and Y. Tokura, *Insulator-metal transition and giant magnetoresistance in $La_{1-x}Sr_xMnO_3$*, Phys. Rev B, 51(20), 14103, (1995)

[3] K. S. Shankar, S. K, and A. K. Raychaudhuria, *Fabrication of ordered array of nanowires of $La_{0.67}Ca_{0.33}MnO_3$ (x=0.33) in alumina templates with enhanced ferromagnetic transition temperature*, App. Phys. Lett, 84(6), 993, 2004

[4] S. Han, C. Li, Z. Liu, B. Lei, D. Zhang, W. Jin, X. Liu, T. Tang, and C. Zhou, *Transition Metal Oxide Core-Shell Nanowires: Generic Synthesis and Transport Studies*, Nano Lett, 4(7), 1241, (2004)

[5] A. Carretero-Genevrier, N. Mestres, T. Puig, A. Hassini, J. Oro, A. Pomar, F. Sandiumenge, X. Obradors, and E. Ferain, *Single-Crystalline $La_{0.70}Ca_{0.30}MnO_3$ Nanowires by Polymer-Template-Directed Chemical Solution Synthesis*, Adv. Mater, 20, 3672, (2008)

[6] M. N. Iliev, M. V. Abrashev, H.-G. Lee, V. N. Popov, Y. Y. Sun, C. Thomsen, R. L. Meng and C. W. Chu, *Raman spectroscopy of orthorhombic perovskitelike $YMnO_3$ and $LaMnO_3$*, Phys Rev B, 57(5), 2872, (1998)

[7] V. B. Podobedov and A. Weber, D. B. Romero, J. P. Rice, H. D. Drew, *Effect of structural and magnetic transitions in $La_{1-x}M_xMnO_3$ (M=Sr, Ca) single crystals in Raman scattering* Phys Rev B, 58 (1), 43, (1998); T. Li, B. Wang, H. Dai, Y. Du, and H. Yan, *Annealing effect on the structural and magnetic properties of $La_{0.7}Sr_{0.3}MnO_3$ films*, J. Appl. Phys., 98, 123505, (2005)

Chapter 6

Electrospun FeGa Nanowires

6.1 Background

It is known that the magnetic properties of the Fe-based alloys strongly depend on the method of synthesis and its subsequent annealing history and composition. It is also well known that low-dimensional magnetic nanowires show some distinctive physical properties compared to their bulk counterparts, even at micro-level. Melt-spun 5 mm width and 75 m thick FeGa ribbons exhibit magnetostriction strains; -2100 ppm was recently observed.In this work, we report the growth and structural characterization and the magnetization response of $Fe_{1-x}Ga_x$ nanowires that are grown on either quartz or Si(111) substrates by the electrospinning technique. To our knowledge, the electrospinning process has never before been used to grow Fe-based alloy compounds.

6.2 Experiment

$Fe_{80}Ga_{20}$ and $Fe_{83}Ga_{17}$ nanowires were fabricated by the electrospinning method. The experimental setup was same as described early in Chapter 5. A stainless steel needle

with an inner diameter of 0.3 mm is connected to reservoirs containing dissolved polyvinyl alcohol (PVA) (Aldrich, Mw = 9,000-10,000) in solutions of appropriate amounts of commercially available:

- Gallium Nitrate $Ga(NO_3)_3xH_2O$ (99.9%, metals basis, Alfa Aesar)

- Iron (III) Nitrate Hydrate $Fe(NO_3)_2x2H_2O$ (99.999%, metals basis, Alfa Aesar)

Desired ration of these nitrates were initially dissolved in 5 gm of deionized water with magnetic stirring at room temperature for over night. As a next step, PVA beads were slowly added to the aqueous solution and resultant gel solution was vigorously stirred for another 5 hours at 80 ^{0}C. The ration of the solvent to the PVA polymers was 3:1. Fig. 6.1 shows viscous, redish color a resultant gel solution. A high voltage of 25 kV was applied to the vertically positioned needle and a base collector plate. A large electric field induces an electrostatic jet from the solution that is then accelerated and stretched to form fine, continuous nanowires on the quartz substrate, which was placed 15 cm from the tip of the needle on an aluminum sheet, see Fig. 6.2 a. After the electrospinning process, the collected nanowires were annealed at 600 ^{0}C for four hours in an ultra-high purity Ar and 3% hydrogen gas mixture. A promising

Figure 6.1 PVA beads were dissolved in FeGa aqueous solution

method recently has been reported was using a magnetic field. D. Yang *et al.* in 2007, fabricated aligned polymer nanowires that were magnetized by the addition of a small amount (less than 0.5 wt%) of magnetic nanoparticles. We adapted this experiment

for the alignment of Fe-Ga nanowires. The prepared solutions were electrospun in the presence of a magnetic field generated by a horseshoe magnet. Fig. 6.2 b. During the annealing process, PVA was removed and continuous $Fe_{80}Ga_{20}$ and $Fe_{83}Ga_{17}$ nanowires were grown (Fig. 6.2 c). After annealing, the nanowires are stored in an inert atmosphere for structural analysis and magnetic measurements.
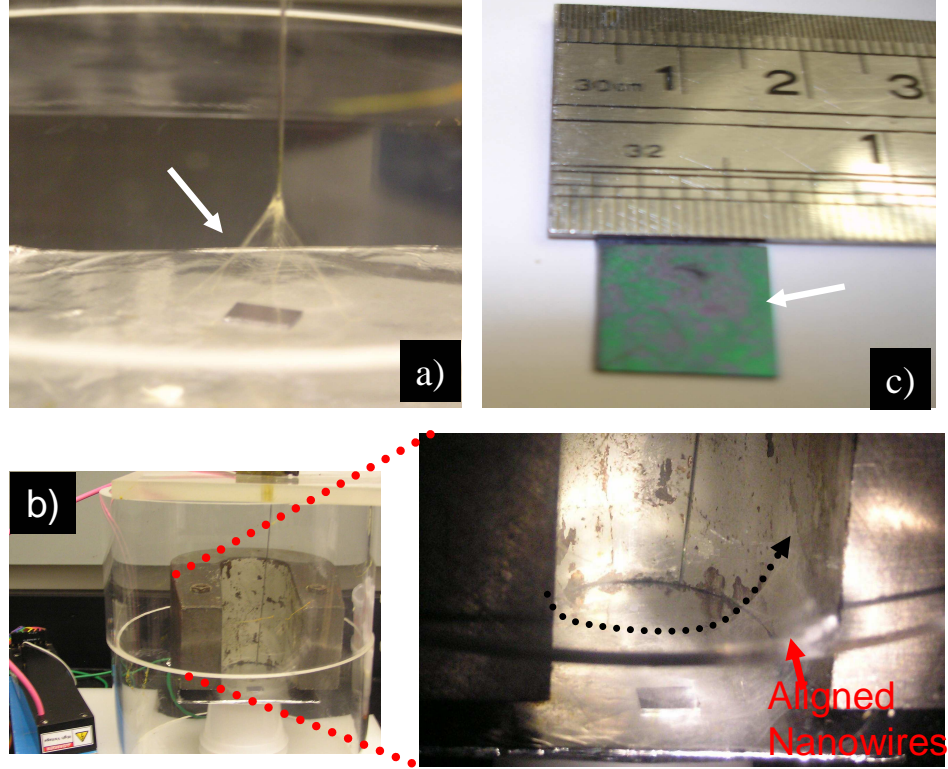

Figure 6.2 a) The electrospinning process for FeGa resultant solution in progress, b) The bundles of FeGa nanowires were grown on Si(111) substrate after annealing at 600 ^{0}C

6.3 SEM characterization

The morphology of the FeGa wires was examined by scanning electron microscopy (SEM - JEOL JSM-5910LV). Fig. 6.3 show images of the aligned nanowires respectively. The alignment technique for the nanowires was same as process described

in Chapter 5. SEM image reveals uniform, smooth, continuous high aspect ratio of FeGa nanowires with diameters in the range of 50-500 nm and lengths up to 500 μm (Fig. 6.3). Statistically we estimated that average diameter of the nanowires were 140-180 nm. The EDS analyses confirm the uniformity of FeGa phases over the entire length of the wires.
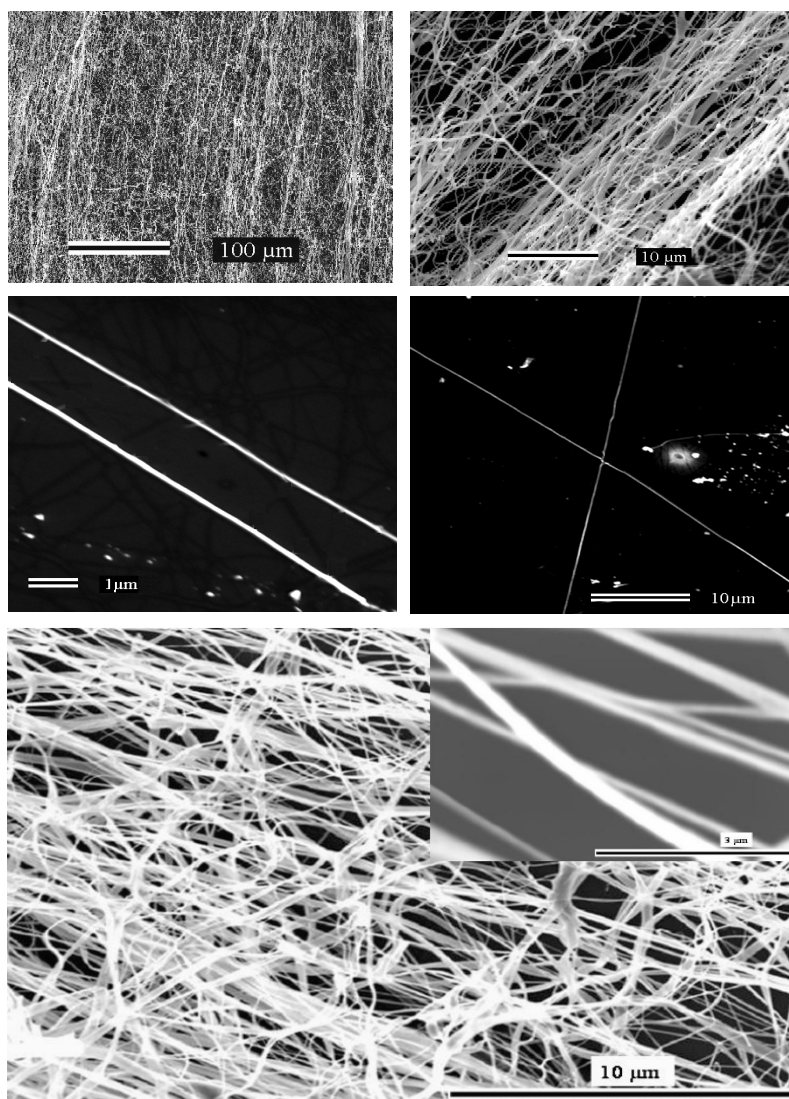

Figure 6.3 SEM images of aligned FeGa nanowires

6.4 XRD characterization

X-ray diffraction (XRD) patterns were recorded with a Thermo ARL diffractometer with Cu-K$_\alpha$ radiation between 2θ of 5 and 80^0 at a scan rate of 10^0 min^{-1}. XRD results confirm that the Fe$_{80}$Ga$_{20}$ and Fe$_{83}$Ga$_{17}$ nanowires spectrum were well matched to that of the body centered cubic, disordered bulk A2 structure with three major peaks with hkl values (110), (200) and (211) without any other secondary phase (Fig. 6.4). The EDS analyses confirm the uniformity of LSMO phase over the entire length of the wires.
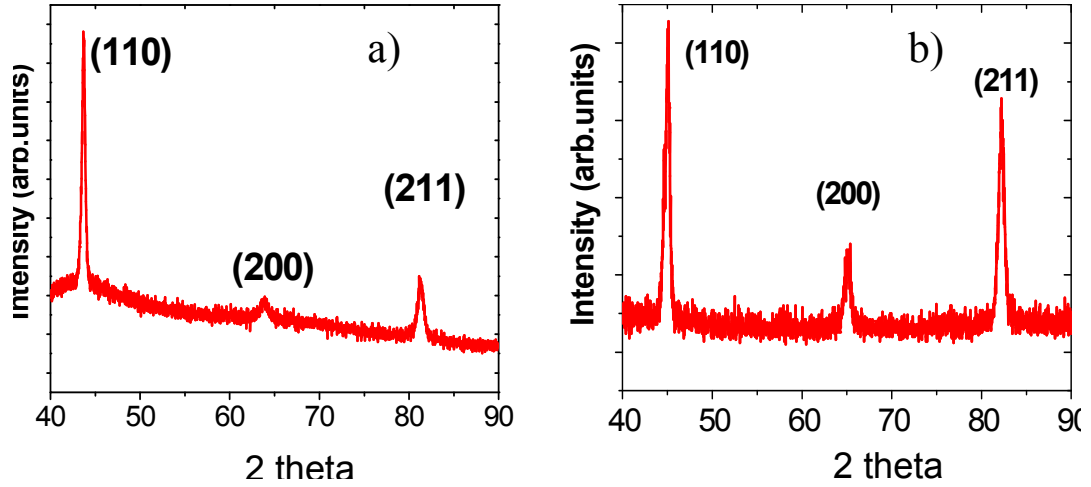
Figure 6.4 XRD spectra of electrospun a) Fe$_{80}$Ga$_{20}$, b) Fe$_{83}$Ga$_{17}$ nanowires

6.5 Magnetic Properties

The magnetic measurements of the as grown nanowire ensemble were carried out in a superconducting quantum interference device magnetometer (MPMSXL5). Fig. 6.5 shows the hysteresis loops of the FeGa nanowires at 4 and 300 K when the external field was applied parallel to the substrate. The diamagnetic contribution of the quartz substrate has been subtracted from the original data. The magnetization (M) versus

magnetic field (H) curves with nonzero coercive field (H_C) and remanent magnetization (M_r) reveal the ferromagnetic behavior of the nanowires. At 300 K, H_C was
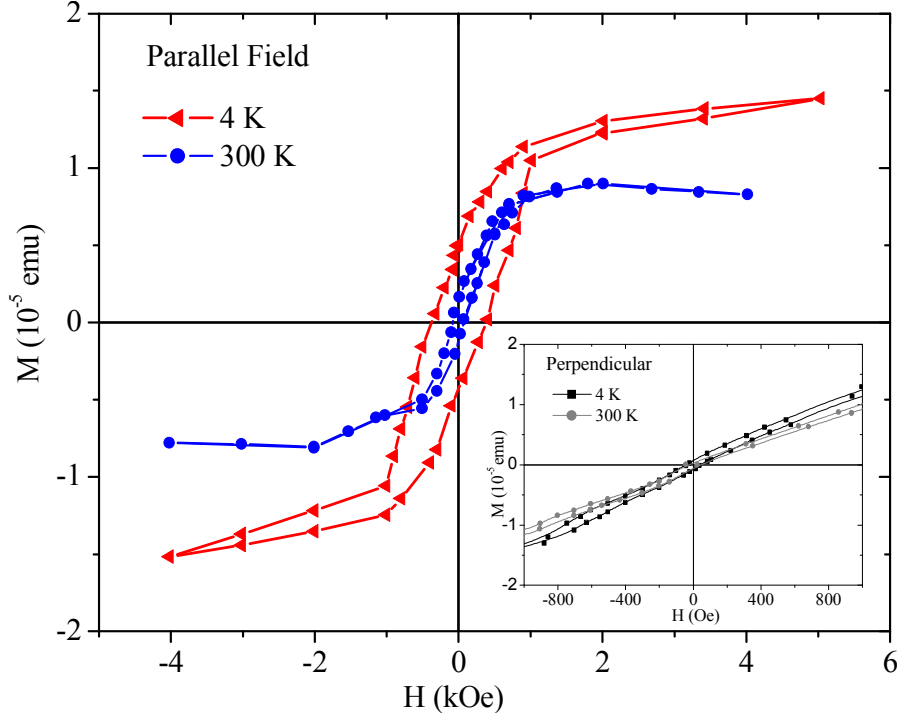

Figure 6.5 Magnetic hysteresis loop of $Fe_{80}Ga_{20}$ nanowires in parallel magnetic field at 4 and 300 K. The inset shows the expanded view of the hysteresis loops measured with magnetic field applied perpendicular to the substrate plane at 4 and 300 K

85 Oe, but H_C=380 Oe was obtained at 4 K. On the other hand, in perpendicular field (inset of Fig. 6.5), the coercivities were lower: H_C=61 Oe at 4 K and it was 36 Oe at 300 K. The coercivities at 300 K are lower than those reported for bulk FeGa alloys and some of the FeGaB thin film compositions. Analyses of the hysteresis loops show that the electrospun Galfenol nanowires exhibit a difference in coercivities of 49 Oe at room temperature in parallel and perpendicular fields and the anisotropy was much larger than reported for α-iron and slightly larger than that of electrodeposited Galfenol nanowires. The shape anisotropy of the electrospun $Fe_{80}Ga_{20}$ nanowires (with aspect ratio of ~1000−10 000) is much larger than the crystal anisotropy;

it is expected that the shape anisotropy is predominant here. It should be noted that all the hysteresis loops were measured from a nanowire ensemble with a size range of 50500 nm. In parallel field, the remanence ratio M_r /M_s was 0.3 at 4 K. (M_s is the saturation magnetization), but the remanence ratio is 0.01 at 300 K.

6.5.1 Magnetization versus Temperature

Fig. 6.6 displays the temperature dependent magnetization measured with H=100 Oe, applied parallel to the substrate, indicating that the Curie temperature might be much greater than 300 K. Clearly, the magnetization decreases monotonically with increasing temperature, displaying that the magnetization behavior of electrospun nanowires is consistent with the results for the gallium substituted α-iron, $Fe_{100-x}Ga_x$ (15<x<20), bulk alloys, which have a reported Curie temperature of around of 675 ^{0}C.

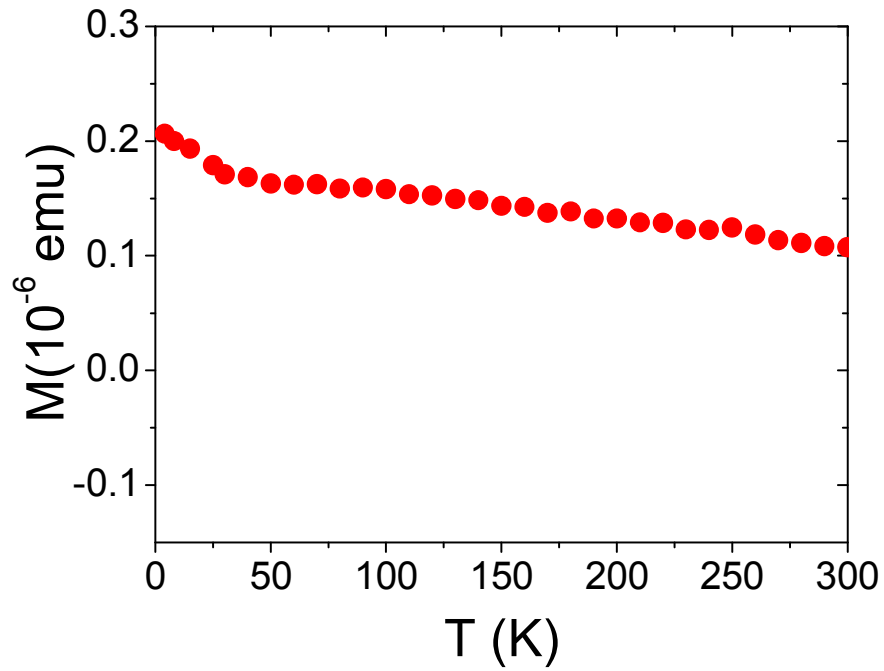**Figure 6.6** Temperature vs magnetization of $Fe_{0.8}Ga_{0.2}$ nanowires (H=100 Oe)

6.6   Spin Dependent Transport

As grown $Fe_{0.8}Ga_{0.2}$ nanowires were sonicated in isopropanol alcohol and then individual nanowires were dispersed onto to heavily doped p-type Si chips capped with a oxide layer same manner described early in Chapter 4.6. Electron beam exposure patters were designed on selected coordination of the nanowires. Two layers of electron beam resist, 540 nm thick, methylmethacrylate (MMA) and polymethylmethacrylate (PMA) were spin coated onto to the chip and each was baked for 150 ^{0}C for 20 minutes. 100 nm Ti/Cu electrodes were deposited to the selected nanowire's by high vacuum electron beam evaporator. (Fig. 6.7) shows single phase $Fe_{0.8}Ga_{0.2}$ nanowire
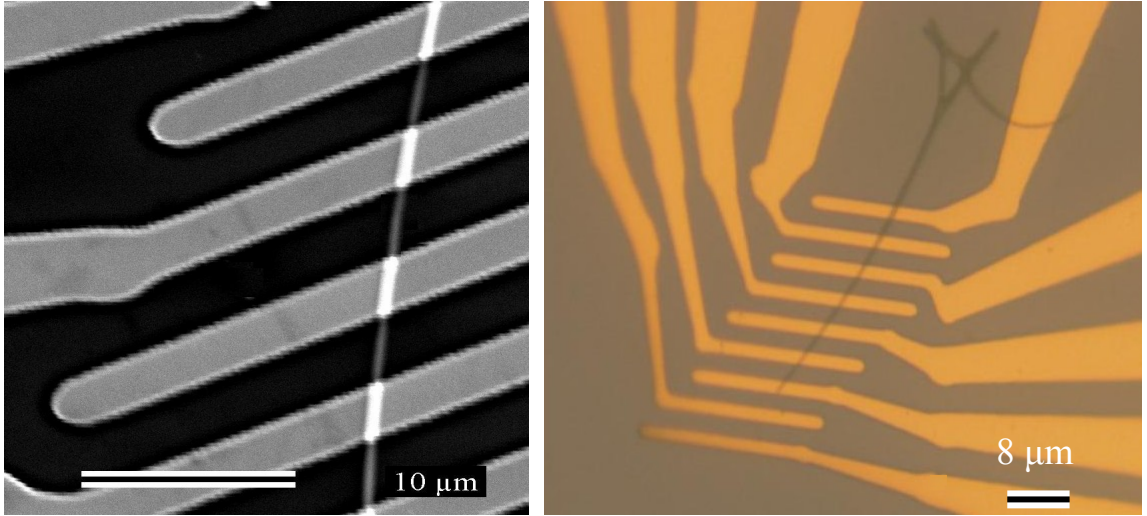

Figure 6.7 Electrical contact to a single $Fe_{0.8}Ga_{0.2}$ nanowires

devices. Except measurement time at room temperature, all devices were kept in high vacuum chamber. The electrical measurement was carried out using an Agilent 4156C semiconductor parametric analyzer at room temperature. When a magnetic field of 800-1000 G was applied to the axial direction of the nanowires, the I-V characteristics significantly changes with higher current in due to presence of the field. Switching off magnetic field produces same I-V response we observed earlier. This behavior was observed several different devices we fabricated.

Although FeGa material is known to be a highly active material for magnetostriction, but not for spintronics, the single nanowire device clearly shows spin dependent transport properties at room temperature (Fig. 6.8).
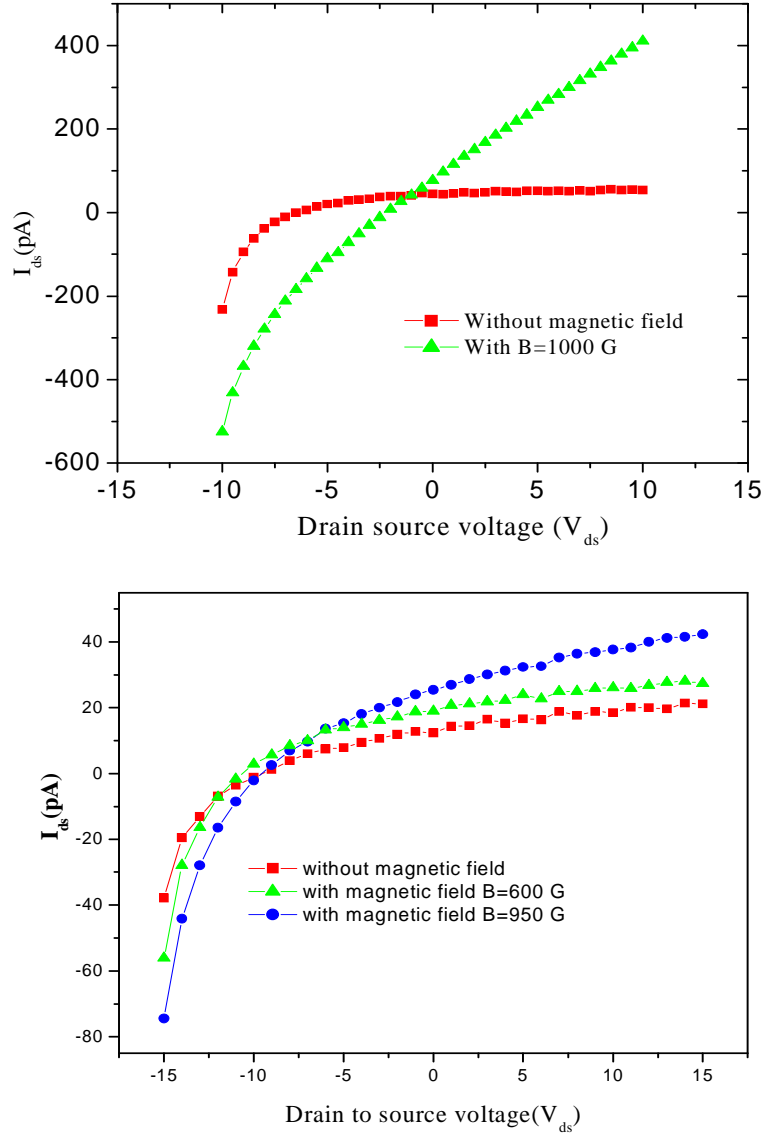

Figure 6.8 I-V characteristics of the electrospun $Fe_{0.8}Ga_{0.2}$ Nanowires

6.7 Conclusions

High quality, continuous magnetostrictive Fe-Ga nanowires with a diameter in the range of 60500 nm have grown using electrospinning method. This work has demonstrated that highly ordered Fe-Ga can be grown aligned or crossed configuration using an external magnetic field in during electrospinning process. The Fe-Ga nanowires structure and morphology was characterized by scanning electron microscopy, and x-ray diffraction. SEM images show the nanowires are uniform. XRD pattern reveal the nanowires have BCC B_2 structures. Superconducting Quantum Interference Devices measurement was carried out at room and low temperatures and exhibited ferromagnetism of the nanowires . In addition to magnetostrictive properties, we have demonstrated that Fe-Ga nanowires show magnetoresistance effect under relatively small magnetic field (600-1000 G). Magnetostrictive and magnetoresistance properties can be combined to fabricate novel devices.

Bibliography

[1] R. Valenzuela, *Magnetic Ceramics*, London, Cambridge University Press, (1994)

[2] K. S. Shankar, S. K, and A. K. Raychaudhuria, *Fabrication of ordered array of nanowires of $La_{0.67}Ca_{0.33}MnO_3$ (x=0.33) in alumina templates with enhanced ferromagnetic transition temperature*, App. Phys. Lett, 84(6), 993, 2004

[3] S. Han, C. Li, Z. Liu, B. Lei, D. Zhang, W. Jin, X. Liu, T. Tang, and C. Zhou, *Transition Metal Oxide Core-Shell Nanowires: Generic Synthesis and Transport Studies*, Nano Lett, 4(7), 1241, (2004)

[4] A. Carretero-Genevrier, N. Mestres, T. Puig, A. Hassini, J. Oro, A. Pomar, F. Sandiumenge, X. Obradors, and E. Ferain, *Single-Crystalline $La_{0.70}Ca_{0.30}MnO_3$ Nanowires by Polymer-Template-Directed Chemical Solution Synthesis*, Adv. Mater, 20, 3672, (2008)

[5] W. L. Sin, K. H. Wong, and P. Li, *Synthesis and Magnetic Properties of $La_{0.67}Sr_{0.33}MnO_3$ Rod-like Particles*, Synthesis and Reactivity in Inorganic, Metal-Organic, and Nano-Metal Chemistry, 38, 260, (2008)

Summary

High quality colossal magnetoresistance $La_{1-x}M_xMnO_3$ (M=Sr or Ca), $0<x<0.34$ and magnetostrictive $Fe_{1-x}Ga_x$, x=0.17-0.20 nanowires below 100 nm were first time grown by electrospinning method. Electrospinning is a very flexible technique that yields wires with different diameters 60 nm-10 μm and can be grown aligned or crossed for different device applications. Their structure and morphology were characterized by scanning electron microscopy, Raman spectra and x-ray diffraction. $La_{1-x}M_xMnO_3$ (M=Sr or Ca), $0<x<0.34$ nanowires have shown orthorhombic crystal structure and $Fe_{1-x}Ga_x$, x=0.17-0.20 nanowires have body centered cubic B_2 phases. Superconducting Quantum Interference Device was revealed ferromagnetic properties of the as grown nanowires. Electron beam lithography technique and Ultra High Vacuum System were used to pattern nanoscale devices and metallizataion for nanowires for electrical transport measurements with and without external magnetic field. La-Sr-Mn-O nanowires show huge spin-dependent transport properties at room temperature in presence of relatively small field (600-1000G) which will be useful for several novel device applications, including nanoscale magnetic sensors, magnetic switches, MEMS devices. Nanoscale La-Sr-Mn-O wires are semiconducting in contrast to the bulk metallic behavior. La-Sr-Mn-O semiconducting and ferromagnetic properties at room temperature can be used to fabricate devices for semiconducting spintronics. In addition to its magnetostrictive properties, single Fe-Ga nanowire act as a tunnel-

ing device which has shown significant spin dependent transport properties at room temperature in presence of low magnetic field (600-1000 G), opening a new avenue to study devices with coupled properties such as high magnetoresistance and high magnetostriction.